UiT
THE ARCTIC UNIVERSITY OF NORWAY

FACULTY OF SCIENCE AND TECHNOLOGY
Department of Geosciences

Combining geophysical data with a mathematical model to describe vertical two-phase flow

—

Johanne Hansen

Master's thesis in Geology GEO-3900

May 2018

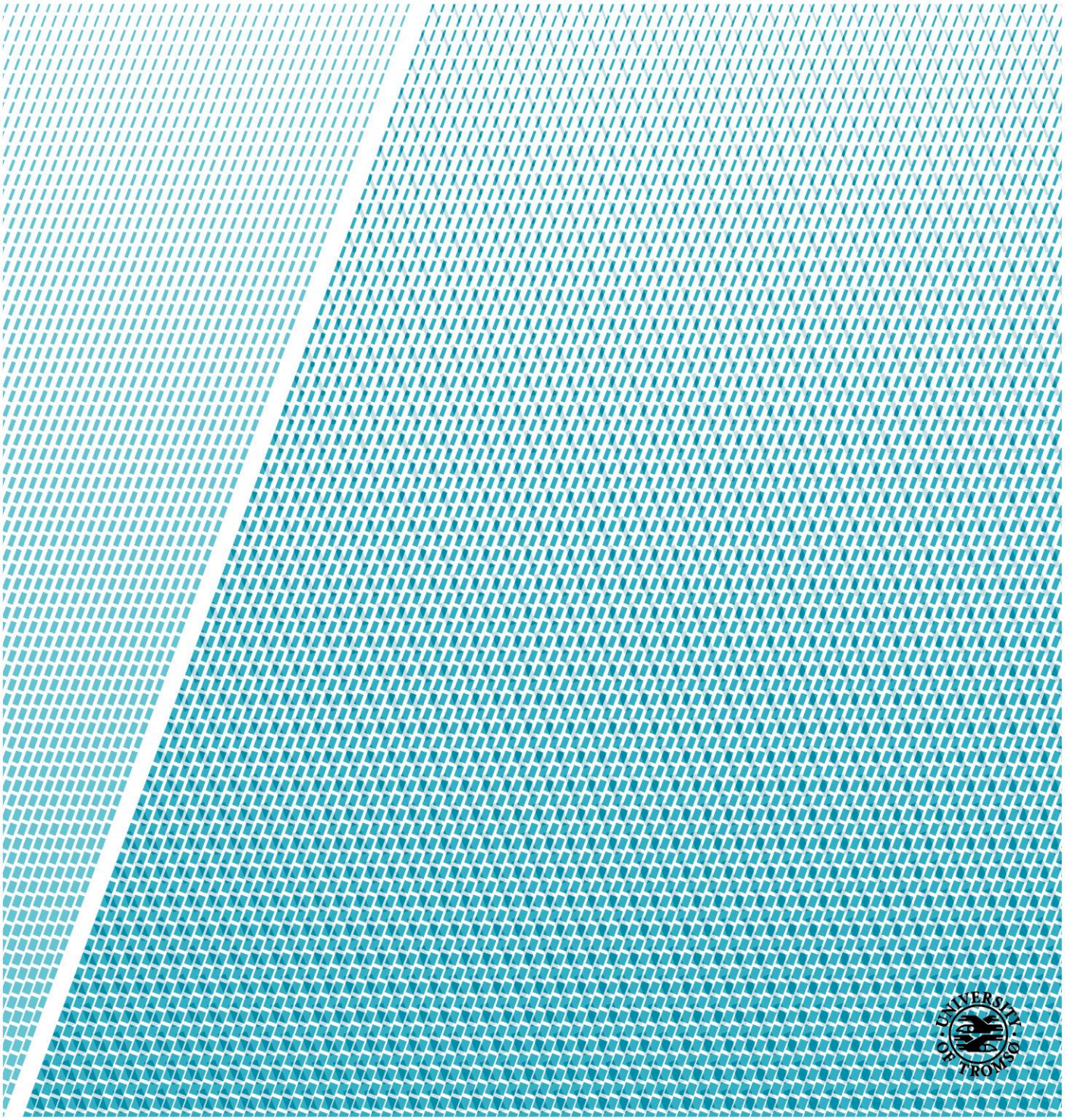

Abstract

This thesis combines a geological model with a mathematical model to describe the vertical propagation of a gas plume through layers with different physical properties. The geological model is based on geophysical data from the Sørvestsnaget Basin and the mathematical model is derived based on the classical Buckley-Leverett theory for two-phase flow.

The model estimates the velocity of a vertical propagating plume based fluid and rock properties. Two different cases are displayed using the model. The first case evaluates how the plume propagates in a homogenous layer and the second case looks at how the plume behaves when crossing a horizontal interface between two different lithologies.

For the first case, the model predicts that the plume evolution consists of three stages. The different stages can be characterised by a different amount of shock and rarefaction waves propagating with different velocities. The model also shows that changing the fluid and rock properties does not change the evolution of the plume. However, the time taken for it to reach the different stages changes significantly. For the second case the model predicts that gas accumulation will occur beneath a boundary if the permeability and porosity above it is not sufficient enough to support the gas flow from the layer below. This results in the formation of two shockwaves travelling in opposite directions with different velocities.

Acknowledgements

This work has been carried out as part of the ARCEx project, grant number 228107, Research Council of Norway.

Finally, but sadly, five years of studying is over. Writing this thesis has been demanding but I am proud to say that I managed to finish. This would not have been possible without the support and help from several people.

First, I would like to thank my supervisors, Alfred Hanssen and Iver Martens, for guidance and valuable feedback during the course of this thesis. I would like to give a special thanks to Alfred for helping me with a Matlab script towards the end of the thesis.

Furthermore, I would like to thank my fellow students, especially 'office buddy' Hanne-Lise for making these five years at university a most enjoyable time.

Finally, I would like to thank my family. I would like to thank my father Lennart for academic input and proofreading. My mother Hilde for encouraging and supporting words. My little brother and roommate Arne and his girlfriend Åshild for support, tasty dinners and nice evenings. Also my grandmother Brit who has called me every Saturday during these last five years.

I would like to give a special thanks to my big brother Emil for helping me with Matlab and the math related topics of this thesis.

Your help and support during the course of this thesis has been invaluable.

"Who says"

Johanne Hansen

Tromsø, May 2018

Contents

1 Introduction

The objective of this thesis is to combine geophysical data with a mathematical model to describe the vertical migration of a gas plume through sedimentary layers with different properties. Information from seismic and log data will be used to make a geological model and estimate key parameters, e.g. porosity and permeability, and give boundary conditions for the mathematical model. The data is collected from one exploration well (7216/11-1S) and one seismic survey (NH9803) from the Sørvestsnaget Basin in the southwestern Barents Sea.

A detailed description of the structure is as follows:

The three first chapters includes an introduction chapter, an overview of the study area and information regarding the data and methods. The first part is meant as an introduction to the reader, where the reader will be familiarised with some of the main concepts and parameters related to fluid flow, as well as the study area and datasets.

Further, the main observations from the seismic and well will be described in Chapter 4. These observations give the basis for the geological model.

Chapter 5 is the modelling chapter and it includes two sections. The first section introduces and derives the original Buckley-Leverett model and its solution. The second section introduces the modified model and a simple walkthrough of the solution.

The last part of the thesis consists of the results and discussion. Here the geological model will be integrated with the mathematical model to describe how the gas plume will migrate in two different cases. In case one, we consider the evolution of the gas plume in a homogenous layer and in case two we look at how the plume evolves when crossing a horizontal boundary.

1.1 Basic parameters and concepts related to fluid flow

The following subchapters will introduce the main parameters and concepts related to fluid flow in porous media, with respect to both the properties of the medium and the fluid.

1.1.1 Porosity

Sediments and rocks consist of a matrix and pores/fractures which can be occupied by fluids. The porosity (ϕ) of a rock is the fraction or percentage of a rock that consists of open space. It can be divided into primary and secondary porosity. Primary is the porosity at deposition and secondary is the porosity after physical and chemical alterations that occur during compaction and burial of the sediments (Selley & Sonnenberg, 2015). Figure 1.1 illustrates the three different types of pores, the catenary/interconnected, cul-de-sac and closed pores. Catenary pores are pores that are in communication with other pores by more than one passage. Cul-de-sac pores are dead end pores, connected to another pore through one passage. Closed pores are isolated pores that have no communication with other pores (Dandekar, 2013). The pore volume (V_ϕ) is given by

$$V_\phi = V_p + V_f, \tag{1.1}$$

where V_p is the volume of the pores and V_f is the volume of the fractures.

The bulk volume (V_B) is given by

$$V_B = V_\phi + V_s, \tag{1.2}$$

where V_s is the volume of the solid.

The porosity of a rock is then given by

$$\phi = V_\phi / V_B. \tag{1.3}$$

Depending on the communication between the pores, porosity is subdivided into effective and ineffective porosity. Effective porosity consists of pores that are connected to each other such as catenary and cul-de-sac pores, whereas ineffective porosity consists of isolated pores. The total porosity is the sum of the effective and ineffective porosities (Selley & Sonnenberg, 2015).

The main factors affecting the porosity is the particle shape, including the sphericity and angularity, packing configuration, sorting, cementation and compaction. Usually the porosity decreases with increasing depth as the rock gets more compacted and cemented (Selley & Sonnenberg, 2015). A porosity of 5% is considered to be low, whereas a porosity of 30% is considered to be high (Dandekar, 2013). Higher porosities exist and in the Ekofisk field in the North Sea there are local porosities as high as 48% (Sulak & Danielsen, 1988).

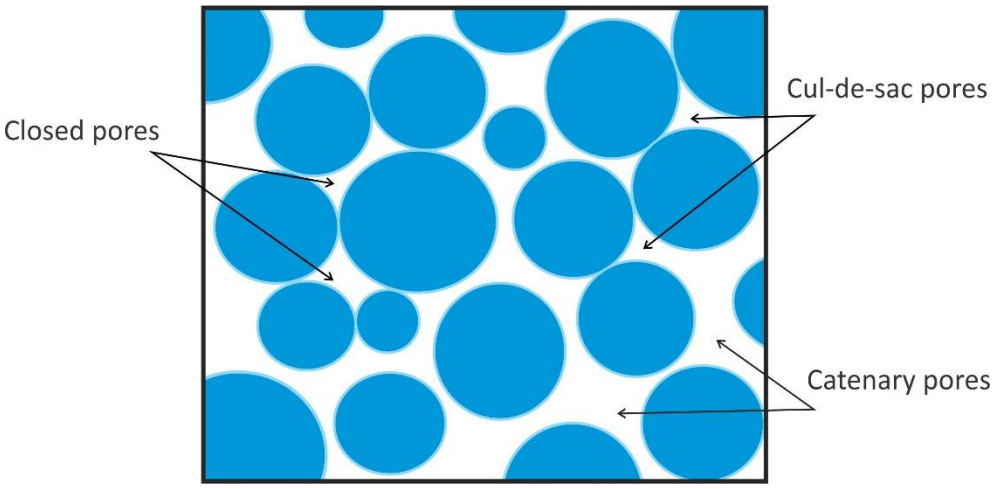

Figure 1.1 The three main type of pores.

1.1.2 Permeability

Permeability defines the ability of a rock or sediment to transmit fluids (Allaby, 2013). It describes the connection and contact between the pores in a porous media. Permeability is seldom equal in all directions within a rock. This characteristic can be used to distinguish between isotropic and anisotropic media. In an isotropic medium, the permeability is the same at all places and in all directions. In an anisotropic medium, the permeability is not equal at all places and it is direction dependent (Ayan et al., 1994).

Porosity is one of the main factors influencing the permeability, but a high porosity does not necessary mean high permeability. Factors such as pore grain size and shape, sorting and packing can affect the permeability (Beard & Weyl, 1973). Permeability is most accurately calculated from core samples, but if they are not available, it can be calculated based on an empirical relationship between the porosity and water saturation (Torskaya et al., 2007). Various empirical relationships

have been suggested. In this thesis Timur's equation is used to calculate permeability. It is given by Timur (1968)

$$k = 8.58\frac{\phi^{4.4}}{{S_{wr}}^2}, \tag{1.4}$$

where k is the permeability, ϕ the porosity and S_{wr} the irreducible water saturation. The unit for permeability is Darcy (D) or millidarcy (mD), and 1 D ≈ $9.87 \cdot 10^{-13}$ m^2. The permeability in reservoirs usually range between 5-500 mD (Selley & Sonnenberg, 2015).

Permeability can be subdivided into absolute, effective and relative permeability. Absolute permeability measures the capacity of the medium to transmit fluids when a single phase is present. Effective permeability is the ability to transmit a particular fluid at a certain saturation. The ratio between the effective permeability to the absolute permeability is known as the relative permeability (Schlumberger, 2017). Figure 1.2 shows the relative permeability curves of oil and water as a function of water saturation. K_{ro} and K_{rw} denote the relative permeability of oil and water, respectively. The blue and red shaded areas are areas in which the water and oil does not flow, respectively. In the white area oil and water flow simultaneously. The readiness with which a fluid flows depends on its saturation in the media. The higher saturation it has, the easier it flows (Buckley & Leverett, 1942). Several models have been developed to relate relative permeability to the water saturation (Li & Horne, 2006). The ones used in this thesis are summarised in Appendix C.

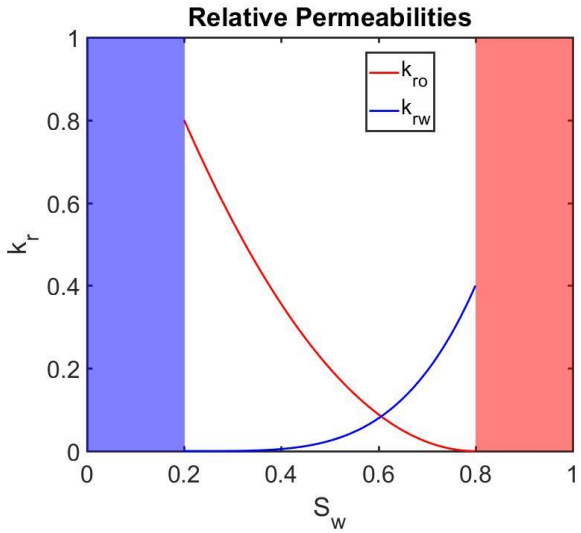

Figure 1.2 Relative permeability curves of oil and water as a function of water saturation

1.1.3 Darcy's law

Fluid flow through a porous media is often described by Darcy's law (Hubbert, 1940). According to Darcy (1856) the fluid flow depends on the permeability of the medium, the pressure gradient and the viscosity of the fluid. Darcy (1856) formulated the law

$$q = -\frac{kA}{\mu}\nabla P\,, \tag{1.5}$$

where *q* is the Darcy velocity, *k* is the permeability, *A* the cross-sectional area, ∇P *is* the pressure gradient and μ is the viscosity of the fluid. The fact that fluids migrate from areas with high pressure to areas with low pressure is indicated by the negative sign in the equation.

1.1.4 Wettability

Fluids have a preferential attraction to themselves. However, fluids may also be attracted to a solid surface. If two fluids are placed on a solid surface, the one that is most attracted to the solid (the wetting fluid) will be the fluid occupying most of the surface, displacing the other fluid (the non-wetting fluid). According to Abdallah et al. (2007) "*wettability describes the preference of a solid to be in contact with one fluid rather than another*". Figure 1.3 shows the concept of wettability. If a solid prefers to be in contact with e.g. water and oil is placed on the solid, the oil will bead up, creating a very small contact angle, θ, with the solid. On the other hand, if the solid prefers to be in contact with the oil, the oil will spread over the entire surface, displacing the water. If the solid does not prefer any fluid, a contact angle will form between the fluids at the surface of the solid.

The wettability of a reservoir is often described as either water-wet or oil-wet and it is affected by factors such as lithology, surface roughness and saturation history. The wettability is an important factor that affects reservoir behaviour and factors such as the distribution of fluids within a reservoir, their movement, recovery and saturation (Abdallah et al., 2007; Falode & Manuel, 2014).

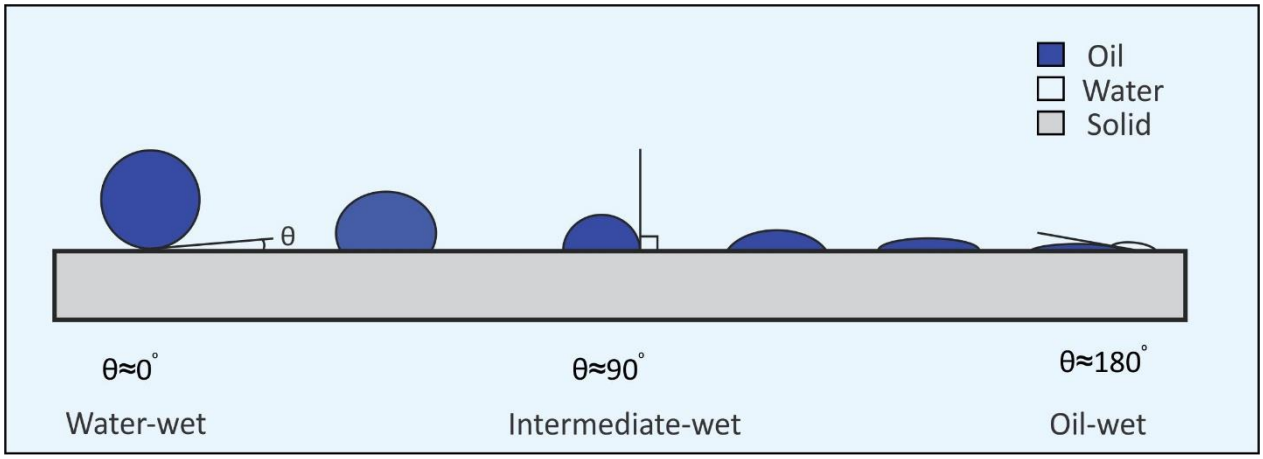

Figure 1.3 Different kinds of wettability. To the left a water wet surface and to the right an oil wet surface. θ denotes the contact angle between the fluid an solid. Based on Njobuenwu et al. (2007).

1.1.5 Capillary pressure

Capillary pressure is the pressure difference across a curved interface between two immiscible fluids caused by interfacial tension (Leverett, 1941). Capillary pressure can also be explained as the amount of additional pressure required to force a non-wetting phase to displace a wetting phase in a pore/capillary (Vavra et al., 1992). The capillary pressure depends on factors such as the surface tension, pore throat diameter and wettability (Leverett, 1941; Schowalter, 1979). By definition it is expressed as

$$P_c(S) = P_{nw} - P_w. \tag{1.6}$$

Here *P* denotes the pressure, *S* is the saturation of the wetting fluid, and the indices *nw* and *w* denote the non-wetting and wetting phase, respectively (Leverett, 1941). To initiate fluid flow, the capillary pressure must be exceeded (Tissot & Welte, 1984).

Figure 1.4 shows the concept of capillary pressure. When two immiscible fluids are in contact with each other through tubes (equivalent to pores in a rock), a curved interface arises between them. The wetting fluid rises due to the adhesive forces between the fluid and solid. The pressure on the convex side (white area in Fig. 1.4) is smaller than that on the concave (blue area in Fig. 1.4).

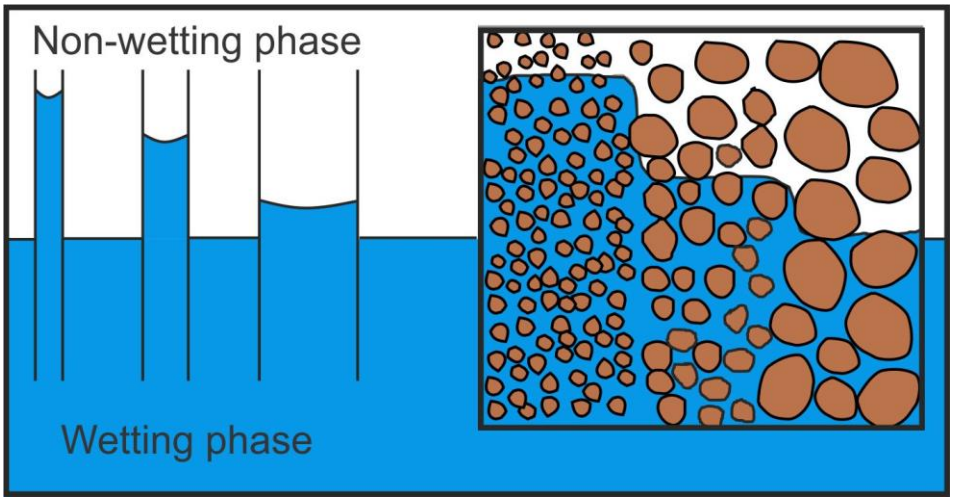

Figure 1.4 Schematic illustration of how capillary forces causes the wetting phase to rise in capillary tubes to the left and a porous media to the right. Modified from ReservioirEngineeringOnline (2014).

1.2 Petroleum systems and migration

A petroleum system is according to Magoon & Dow (1994) defined as a *"geological system that encompasses a pod of active source rock and all related oil and gas and includes all the essential elements and processes needed for oil and gas accumulations to exist".* The elements are the source-, reservoir-, seal- and overburden-rock. Trap formation and generation-migration-accumulation of petroleum are considered as important processes. For an accumulation to occur, these factors must occur in a particular order relative to each other (Magoon & Dow, 1994).

The source mainly consists of organic rich shales and the reservoirs of either sandstones or carbonates. According to Downey (1994) any rock may act as a seal as long as the capillary pressure is greater than the buoyancy pressure from the hydrocarbon column. However, all seals are subjected to fluid flow despite their low permeability properties (Cartwright et al., 2007).

1.2.1 Migration

The most common reservoir rocks such as sandstones and carbonates are deposited in oxidizing environments, where most organic matter is destroyed (Barker, 1980). This means that hydrocarbons are not formed in the reservoirs, but must have entered them from somewhere else. The process in which oil and gas moves from a source to a trap is known as migration. Figure

1.5 shows the three different types of migration; primary, secondary and tertiary migration (Peters et al., 2012). The mechanisms behind each stage are not the same and for some stages they are not completely understood (Bjørlykke, 2015).

Primary migration (Fig. 1.5) is the process where hydrocarbons are expelled from the source rock itself into adjacent carrier beds (Peters et al., 2012). The process behind is not fully understood, but it is believed to involve several mechanisms where complex interactions occur between water, rock matrix and petroleum. These factors change in composition and/or amount with increasing burial and different mechanisms may dominate at different depths (Barker, 1980).

Secondary migration (Fig. 1.5) is the process where petroleum is transported from the source rock to a trap (England, 1994). Most hydrocarbons migrate as a separate, immiscible phase through water saturated formations. There are three physical mechanisms affecting secondary migration. The main driving force is buoyancy, which is related to density differences between the hydrocarbon phase and water phase (Schowalter, 1979). The magnitude of the buoyancy force depends on the density difference between the fluids. The greater difference, the greater force. A second process affecting migration is hydrodynamics. It adds a directed force which may be in any direction. Depending on the nature of the flow involved, the buoyant force may be increased or reduced (Pegaz-Fiornet et al., 2012). The last process affecting migration is the capillary pressure. This is a resistance force (Schowalter, 1979). Migration occur as long as the buoyancy forces are greater than the forces of capillary pressure (Hindle, 1997; Selley & Sonnenberg, 2015).

Traps may leak due to fracturing or structural movements. As a consequence, remigration of hydrocarbons into new traps or all the way to the seafloor may occur. This is a process known as tertiary migration (Fig. 1.5) (Peters et al., 2012).

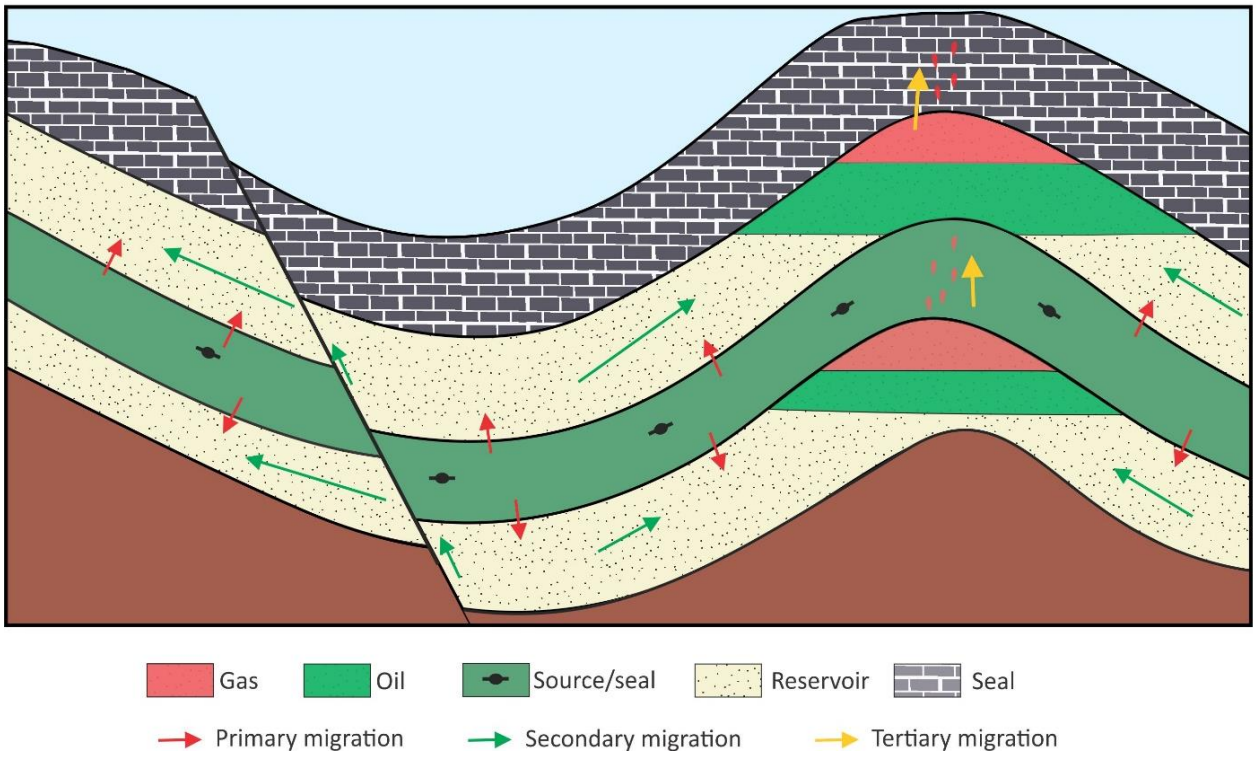

Figure 1.5 Primary, secondary and tertiary migration. Modified from Tissot & Welte (1984).

1.2.1.1 Lateral migration

Migration following the stratigraphy in an area is known as lateral migration. This usually occurs in confined permeable layers (Floodgate & Judd, 1992). Lateral migration may occur over several kilometres extending from source to reservoir or seabed. Petroleum expelled from primary migration gradually piles up as a separate phase, and creates a stringer of petroleum in the layer (England, 1994). Figure 1.6 shows migration in a) homogenous media and b) heterogeneous media. Assuming a dipping carrier bed, the stringer will grow and start moving up dip due to buoyancy. In a homogeneous bed, the migration will be restricted to the upper boundary between the bed and sealing rock (fig 1.6a). In a heterogeneous bed, the uneven capillary pressures will lead to a more dendritic pathway deflecting the migration from the structurally most advantageous route (Fig. 1.6b) (England, 1994).

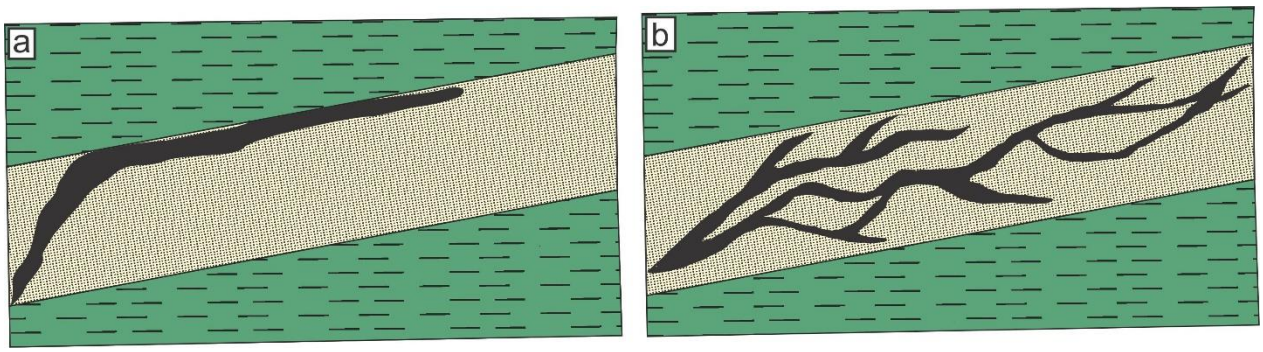

Figure 1.6 a) Migration in a homogenous media. Based on England(1994). b) Migration in a heterogeneous media. Modified from England (1994).

1.2.1.2 Vertical and fault related migration

Vertical migration occurs across stratigraphic units. An increase in pressure due to no lateral drainage paths or due to water and gas expansion, may create fractures in a layer in which fluids can escape through (Hindle, 1997; Bjørlykke, 2015). Whereas lateral migration occurs in permeable and porous units, vertical migration usually occurs in low permeable layers such as mudstones and shales, or in the absence of seals (Floodgate & Judd, 1992; Hindle, 1997). Migration related to faults have been heavily discussed, but observations such as large pockmarks, mud volcanoes and hydrothermal deposits situated above or along faults links them to significant fluid fluxes (Cartwright et al., 2007). According to Ligtenberg (2005) faults work as the main fluid conduits in deeper basins with more consolidated and lithified rocks. Faults may also deflect the migration as two porous and permeable lithologies may be juxtaposed across the fault (Hindle, 1997).

Faults can have the opposite effect and work as seals. The fault can work as a seal itself, or a sealing unit can be juxtaposed against reservoir units across the fault. Whether a fault is sealing or not depends on the cementation and rock properties that develop within the fault zones. These are affected by factors such as pressure differences across the fault, fault and burial histories, stress direction, composition of material etc. (Watts, 1987; Cerveny et al., 2004).

1.3 Seismic principle

Each layer in the subsurface has a certain density and wave propagation velocity. The product of these properties is known as the acoustic impedance (AI) (Sheriff, 2002). Seismic exploration utilises the fact that different lithologies may have different AI. Figure 1.7 shows how seismic waves reflect and refract at boundaries where there is a change in acoustic impedance. The reflected or refracted signals are recorded by a receiver where the arrival time and amplitude of the signals are used to create seismic lines (Selley & Sonnenberg, 2015). Seismic exploration includes both reflected and refracted surveys, but mainly the former is used. The acoustic impedance is given by

$$Acoustic\ Impedance = v\rho, \tag{1.7}$$

Where ρ is the density of the layer and v is the P-wave propagation velocity in the respective layer.

Seismic waves travel through the earth as body or surface waves. Surface waves travel directly to the receivers along the surface of the ground or water. Figure 1.8 shows how the two main body waves, the compressional (P) and shear (S) wave, propagate through earth. P-waves are the fastest waves and the particle motion is parallel to the direction of wave propagation (fig 1.8a). S-waves cannot move through fluids, they are slower and the particle motion is perpendicular to the direction of wave propagation (fig 1.8b) (Sheriff, 2002). Due to their ability to travel through all media, the P-waves are considered to be most important in traditional seismic exploration. However, in the more recent years, receivers have been placed on the ocean floor during some surveys. This makes it possible to record both P- and S-waves. By combining the P- and S-wave velocity a clearer image of the subsurface can be obtained (Peak Seismic Solutions, 2017). E.g. if a change in P-wave reflection amplitude across an interface is combined with a constant-S wave amplitude it is more likely to indicate fluids rather than a lithology change. If the S-wave amplitude also changes, the variation is more likely caused by changing rock properties.

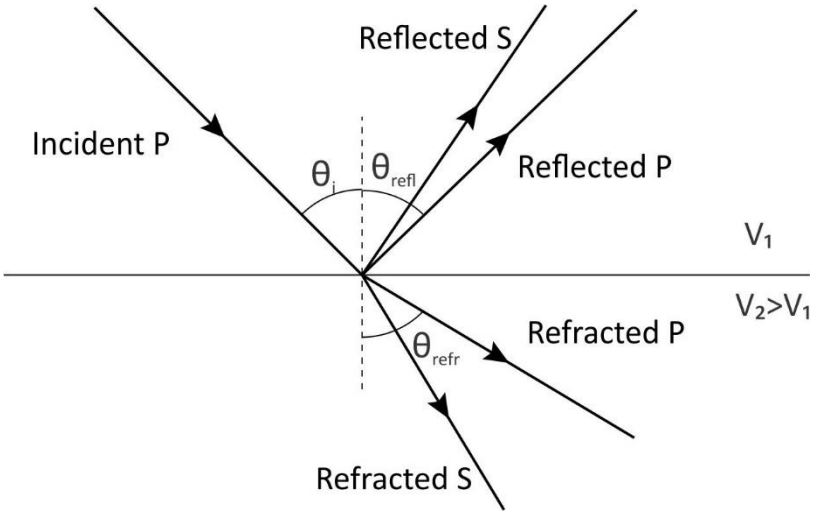

Figure 1.7 Relationship between the incident, reflected and transmitted waves. Modified from Kearey et al. (2002).

When hitting an interface, the wave will reflect, refract and convert (fig 1.7). The relationship between the incident wave and refracted wave can be described by Snell's law (Kearey et al., 2002), which is given by

$$\frac{sin\ \theta_i}{sin\ \theta_{refr}} = \frac{V_1}{V_2}, \tag{1.8}$$

Here, θ_i is the incident angle and θ_{refr} is the P-wave refracted angle and V_1 and V_2 are the P-wave velocities in the respective layers.

The reflection coefficient, RC, is the ratio between the amplitude of the reflected wave and the incident wave (Sheriff, 2002). It is expressed as

$$RC = \frac{AI_2 - AI_1}{AI_2 + AI_1}, \tag{1.9}$$

where the subscripts *1* and *2* denotes the lithology above and below a boundary, respectively.

The reflection coefficient is a measure of the strength of a seismic reflection. The amplitude of the recorded signal can be used to estimate the acoustic impedance contrast across the boundary (Andreassen, 2009). The values of RC lie between -1 and 1, where a value of ± 1 indicates that 100% of the energy is reflected. The positive and negative sign says something about the phase

of the signal. RC is positive if there is an increase in acoustic impedance across a boundary and the phase of the wave remains the same. RC is negative if there is a decrease in acoustic impedance and there is a phase-reversal of the wave (see 1.4.5). Reflection coefficients usually lie between ± 0.2 and rarely exceed ± 0.5 (Kearey et al., 2002).

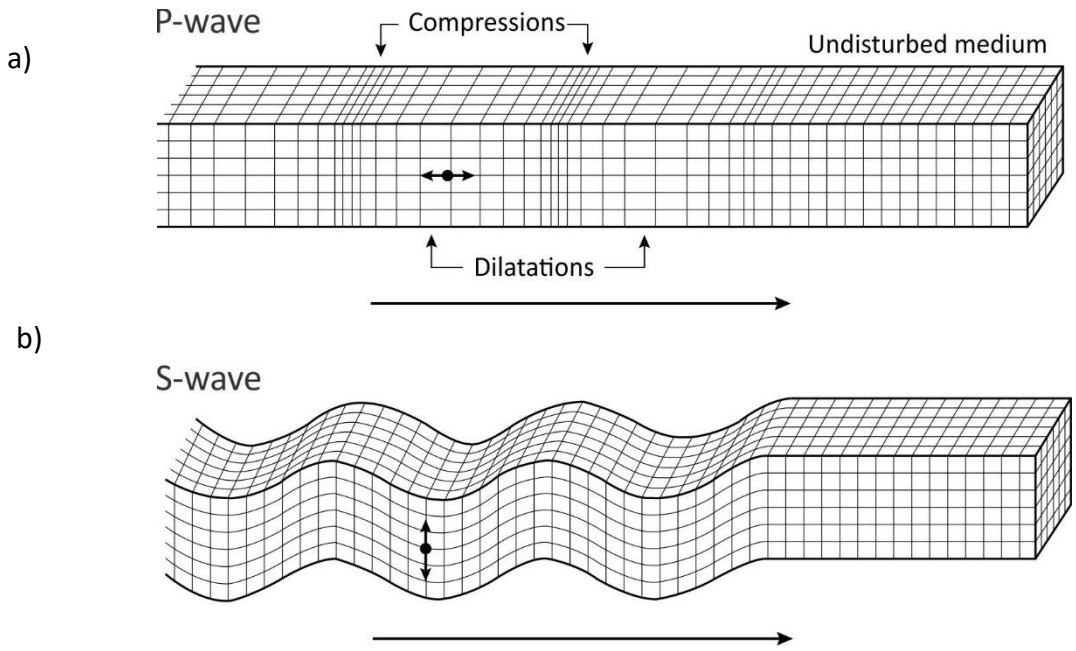

Figure 1.8 The propagation of a) P- and b) S-waves. Modified from Kearey et al. (2002).

1.3.1 Resolution

The contrast in acoustic impedance across boundaries produce seismic reflections as seismic waves hit the interfaces. For layers or structures to be detected, the contrast has to be large enough and the resolution high enough, both in the vertical and horizontal dimension. It is important to find the resolution to a dataset because it says something about what you are able to identify. Resolution is according to Sheriff (2002) defined as "*the minimum separation of two bodies before their individual identities are lost on the resultant map or cross section*". The wavelength (λ) of a signal strongly influences the resolution and is given by

$$\lambda = \frac{v}{f}, \tag{1.10}$$

where *v* is the wave velocity in the formation and f the frequency of the signal (Brown, 2011).

1.3.1.1 Vertical resolution

Vertical resolution refers to the ability to distinguish two close seismic events vertically corresponding to different depth levels (Chopra et al., 2006). Figure 1.9a shows a schematic illustration of a sedimentary wedge and 1.9b show a synthetic seismic section for the same wedge. Vertical resolution consists of two limits; the limit of separability and the limit of visibility (Brown, 2011). The limit of separability is the common measure for vertical resolution and is determined by the dominating wavelength. In theory, the vertical resolution is 1/4 of the wavelength (Brown, 2011). Thinner layers are still observed, but the top and bottom reflections interfere until they reach the limit of visibility, which corresponds to the minimum thickness a layer must have to give a reflection (Sheriff, 2002). The visibility limit varies and depends on the signal to noise ratio, the acoustic impedance and the phase of the seismic wavelet. At best, it can be 1/30 of a wavelength if there is an excellent signal to noise ratio and high acoustic contrast (Brown, 2011). The vertical resolution is given by

$$Vertical\ resolution = \frac{\lambda}{4}. \tag{1.11}$$

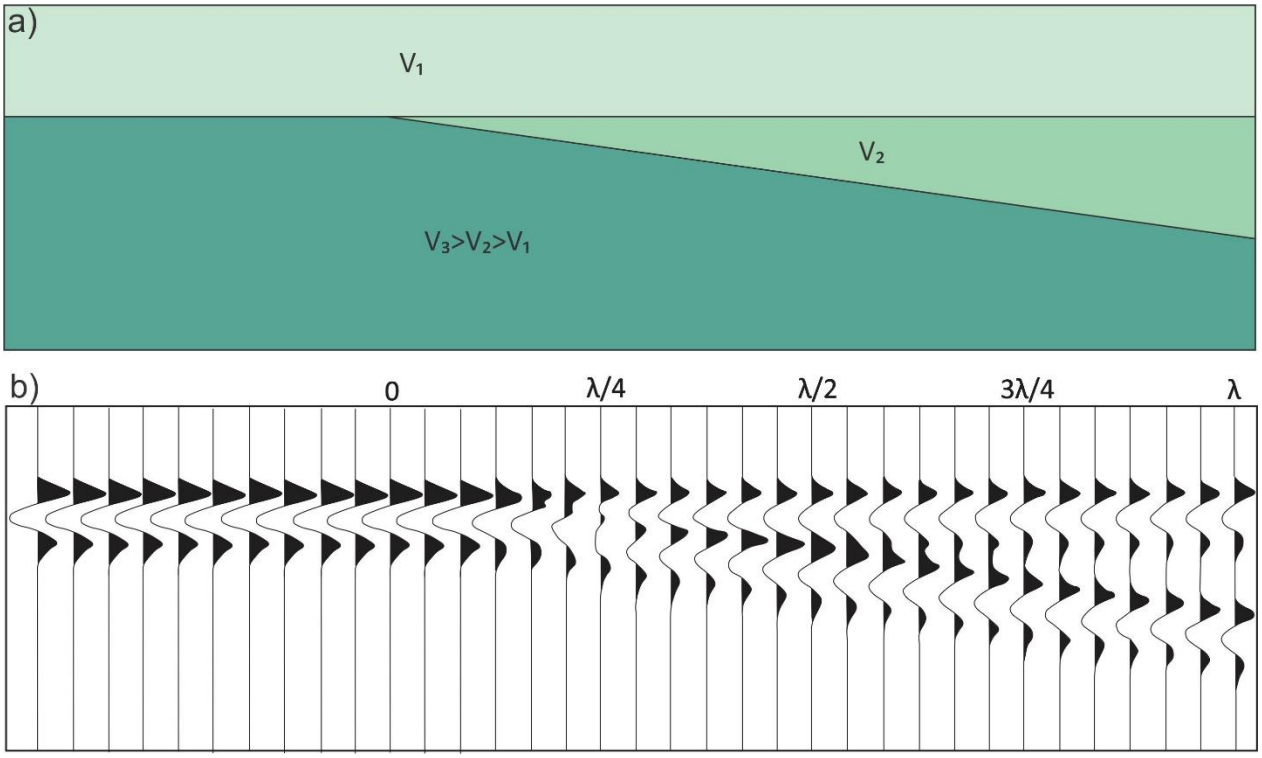

Figure 1.9 a) Schematic illustration of a sedimentary wedge and the relative velocity of the layers. b) Generated synthetic seismic section. Modified from Badley (1985).

1.3.1.2 Horizontal resolution

Horizontal resolution concerns the ability to separate and recognize laterally displaced features as individual events (Chopra et al., 2006). A signal from a source has a spherical propagation, hence, the reflection of a seismic wave affects an area, not a point. This area is known as the Fresnel Zone and is limited by the area that the wave front λ/4 later makes with the reflector (Sheriff, 2002). Figure 1.10 shows the concept of the Fresnel zone and the difference in the Fresnel zone between a high and low frequency wave. The arrival times between the first wave and the one a quarter of a wavelength later, differ by less than half a period. This will cause all the waves between the two arrival times to interfere constructively and be considered as a single reflection (Sheriff, 2002). Structures with a lateral extent larger than the Fresnel zone will be visible in the seismic.

The Fresnel Zone is a function of the wavelength (velocity and frequency) and depth. On unmigrated data, the diameter of the Fresnel zone is

$$F_d = \sqrt{2Z\lambda}, \tag{1.12}$$

where *Z* is the depth (Kearey et al., 2002).

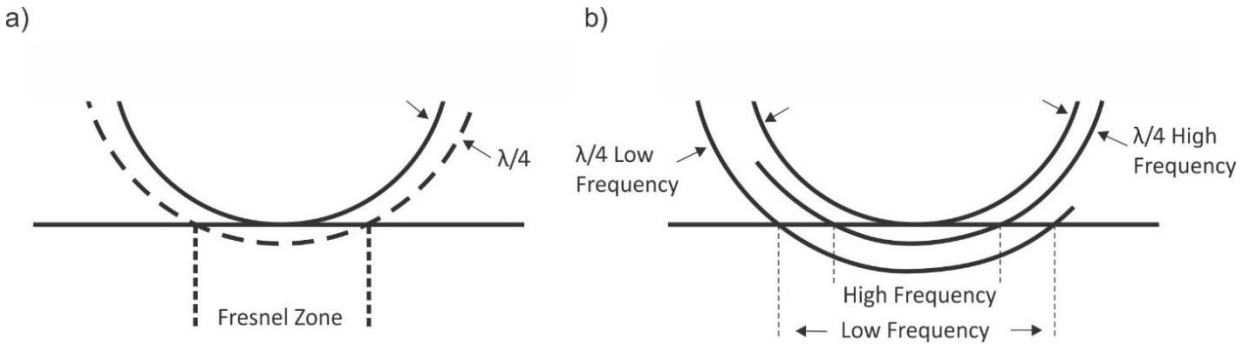

Figure 1.10 a) Showing the concept of the Fresnel zone. b) Shows the difference in the Fresnel zone between a high and low frequency wave. Modified form Sheriff (1985).

Migration is a processing technique that enhance the lateral resolution. It re-arranges misplaced reflections due to dip in the subsurface, removes diffractions from edges and points, and focuses the spread energy over a Fresnel Zone (Brown, 2011). In migrated data, the Fresnel zone is reduced. The amount of reduction depends on the type of seismic. Figure 1.11 shows the migration of 2D and 3D data. Migration of 2D seismic reduce the Fresnel zone to an ellipsoid perpendicular to the inline direction (Brown, 2011). In 3D seismic, migration collapse the Fresnel zone to a small circle with a size comparable to the vertical resolution. Perfect migration reduces the Fresnel zone to a quarter of a wavelength, but usually it is reduced to half of the wavelength (Brown, 2011). Horizontal resolution on perfect migrated data is given by

$$Horizontal\ resolution = \frac{\lambda}{4}. \tag{1.13}$$

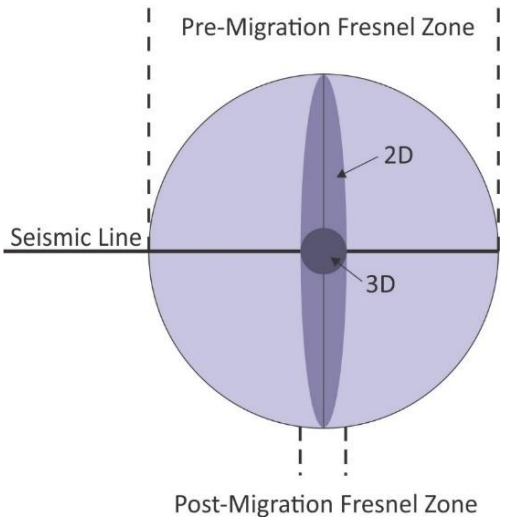

Figure 1.11 The Fresnel zone before and after migration of seismic data. Modified from Brown (2011).

Both the vertical and horizontal resolution depend on the wavelength, which is affected by the velocity, frequency and depth. Figure 1.12 shows how the velocity and frequency change with depth. Rocks gets more compacted and denser with depth, causing an increase in seismic velocity. The frequency decreases with depth due to higher frequencies being more easily absorbed and attenuated. Thus, the wavelength increases significantly with depth, causing a poorer resolution (Brown, 2011). Other factors such as reflections, refractions, mode conversions and spherical divergence cause a loss of seismic energy and an increase in wavelength with depth (Andreassen, 2009).

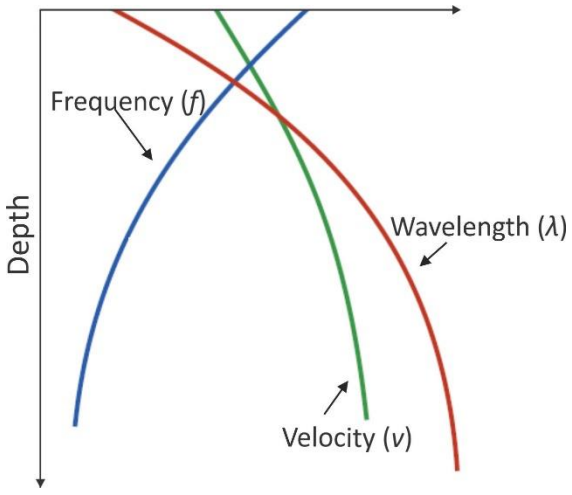

Figure 1.12 Variation in frequency, velocity and wavelength with depth. Modified Brown (2011).

1.4 Indication of fluids and migration

A lithology filled with fluids can create distinct seismic response depending on the properties of the fluid. The way they affect the seismic waves depend on the sedimentary background and what type of fluid is present (Badley, 1985). In general gas causes a greater change in acoustic impedance compared to e.g. oil, because it creates a significant reduction in P-wave velocity and a small decrease in density (Andreassen, 2009). Figure 1.13 shows some of the main indications of fluids on seismic data.

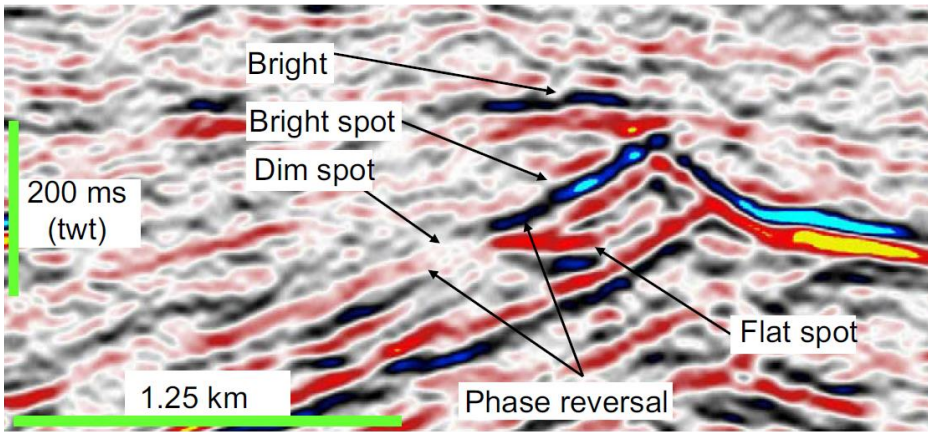

Figure 1.13 Bright spot, dim spot, phase reversal and flat spot. Figure from Løseth et al. (2009).

1.4.1 Bright spots

A bright spot is a local increase of amplitude on a seismic section (fig 1.13). The amplitude anomaly is often associated with gas-filled porous sands (Badley, 1985). The presence of gas in the pores of the sand will cause a drastic reduction in seismic velocity, hence the acoustic impedance will decrease. The result is a negative reflection coefficient and a strong reflection whose polarity is reversed to that of the seafloor. A bright spot does not necessarily imply fluids and it can be both positive and negative in amplitude. Lithological changes such as the presence of carbonates or intrusions could give rise to amplitude anomalies (Badley, 1985).

1.4.2 Acoustic masking/wipe out zones and acoustic pipes

Areas on the seismic with weak, disturbed and distorted reflections are known as acoustic masking/chimneys/wipe out zones (Andreassen et al., 2007a; Løseth et al., 2009). Figure 1.14

shows a schematic illustration of acoustic masking and pockmarks (1.14a) and how they may appear on the seismic (1.14b). These features are often associated with other fluid indicators such as bright spots. The chaotic reflection pattern results from scattering and attenuation of seismic energy when it interferes with gas that have penetrated the cap and overburden rocks (Badley, 1985). Wipe out zones in 2D and 3D seismic may be a result of ongoing or previous migration. Smaller and narrower zones of acoustic masking often occur as connections between bright spots. These circular and sub-vertical zones may appear over a long vertical distance and are referred to as acoustic pipes (Andreassen et al., 2007a).

1.4.3 Flat spots

The interface between gas and water, gas and oil, and oil and water can have a strong AI contrast. If the reservoir and hydrocarbons columns are thick enough, the base of the oil and gas phases will generate a reflection. Since these boundaries in most cases are horizontal, the corresponding reflection will be horizontal (fig 1.13). A horizontal reflection that cuts the surrounding stratigraphic reflections is known as a flat spot (Løseth et al., 2009). A flat spot does not have to be horizontal in the seismic as it depends on the hydrodynamic conditions of the subsurface (Nanda, 2016). Flat spots do not necessarily imply fluids. They can also be caused by lithological changes and diagenetic effects in the subsurface (Badley, 1985). Usually flat spots are found down to a depth of approximately 2500m. Below this depth, the effect of especially gas on the velocity is less drastic (Andreassen, 2009).

1.4.4 Dim spots

Dim spots (fig 1.13) are often associated with carbonates and compacted sandstones. The initial velocity in these lithologies are high. Gas will reduce the velocity and AI, but not enough to create a negative reflection coefficient (Sheriff, 2002; Nanda, 2016). Therefore, the reflection remains positive, but weaker at the top of the reservoir compared to flanks.

1.4.5 Phase reversal

If the reflection from the top of a reservoir changes from a trough to a peak, or vice versa, across the fluid contact, a phase reversal occurs (fig 1.13) (Brown, 2011). This happens when there initially is an increase in AI from cap rock to reservoir. E.g. when a reservoir gets filled with gas,

the velocity at the top of the reservoir will decrease and there is a decrease in AI. This will cause a negative RC at the top of the reservoir and a positive RC at the flanks, changing the polarity of the reflection along the top reservoir.

1.4.6 Pockmarks

The presence of fluids in the subsurface may also be seen on the seabed. Pockmarks (fig 1.14 a/b) are shallow crater-like depressions formed in soft and fine grained sediments on the seafloor in both oceans and lakes (Ligtenberg, 2005; Judd & Hovland, 2007). Their size, depth and shape vary. Pockmarks may occur together occupying large parts of the seafloor, or as few isolated individuals. Their formation is related to fluid flow, where the nature of the involved fluids may vary. Very often pockmarks are located close to faults and bright spots, or disturbed seismic such as wipe out zones and acoustic pipes (Judd & Hovland, 2007; Løseth et al., 2009). Pockmarks can also be found on buried surfaces. These paleo-pockmarks are filled in with sediments and indicate previous fluid flow in the area (Judd & Hovland, 2007).

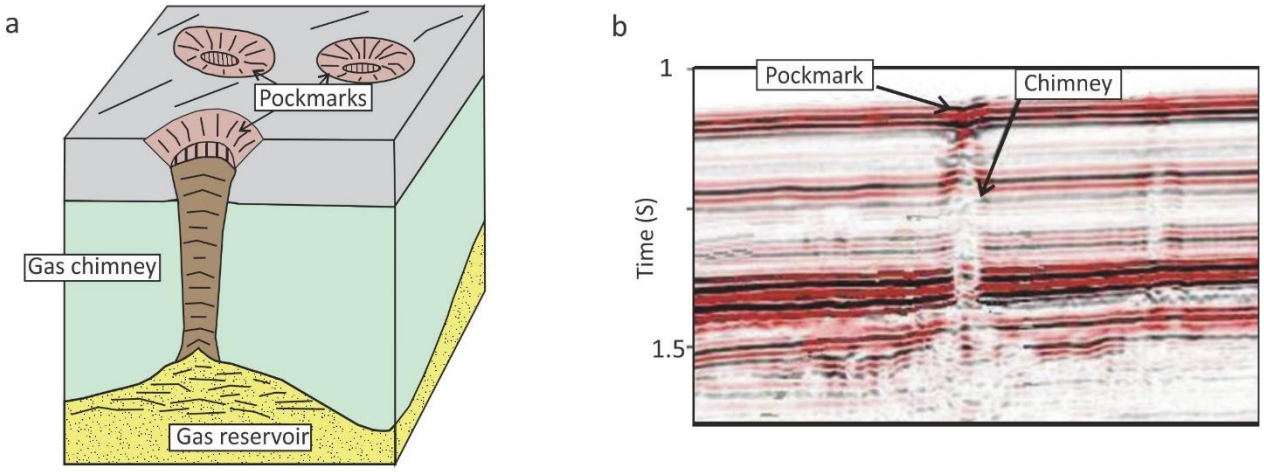

Figure 1.14 a) Schematic illustration of a gas chimney with a pockmark on top. b) Pockmark and chimney in a seismic section. Modified from Cathles et al. (2010).

1.5 Well logs

A well log is a continuous recording of a geophysical parameter along a borehole (Rider & Kennedy, 2011). Well logs contain important physical data of the subsurface. Some of the main logs are the density, sonic, gamma ray, neutron porosity and resistivity log. In the following subchapters, the function of the logs will be described. The information/description regarding each log is mainly based on the book "The Geological Interpretation of Well Logs" by Rider & Kennedy (2011) unless stated otherwise.

1.5.1 The density log

Density logs measures the bulk density of formations. This includes the density of the rock and potential fluids enclosed in the pores. Figure 1.15 shows the density measurements for some typical lithologies.

The log works by emitting gamma radiation into the formation, and measuring the induced radiation. Electrons in the formation attenuate and re-emit the emitted gamma rays causing them to loose energy and change direction (Compton scattering). This results in a lower flux of incoming gamma rays and a decrease in their energy. The more electrons, the higher the attenuation. Hence, the attenuation and re-emitting of gamma rays is a function of the electron density (electrons/cm^3) of the formation, which is closely related to density (g/cm^3).

The density log has some important applications. It can calculate the hydrocarbon volume and density, and model seismic response (multiplied with sonic log to calculate acoustic impedance). Lithologies are rarely defined by the density log alone, as they show a great variation in composition and texture. If combined with the neutron log (chapter 1.5.4) it becomes a good indicator of general lithology.

The principal use of the density log is to calculate potential porosities. The equation for bulk density is given by

$$\rho_b = \phi\rho_{fl} + (1-\phi)\rho_{ma}, \tag{1.14}$$

where ρ_b denotes the bulk density, $\rho_{ma}$the matrix density, ρ_{fl} the density of the fluid and ϕ the porosity. Rearranging the equation and solving for porosity, equation (1.14) becomes

$$\phi = \frac{\rho_{ma} - \rho_b}{\rho_{ma} - \rho_{fl}}. \tag{1.15}$$

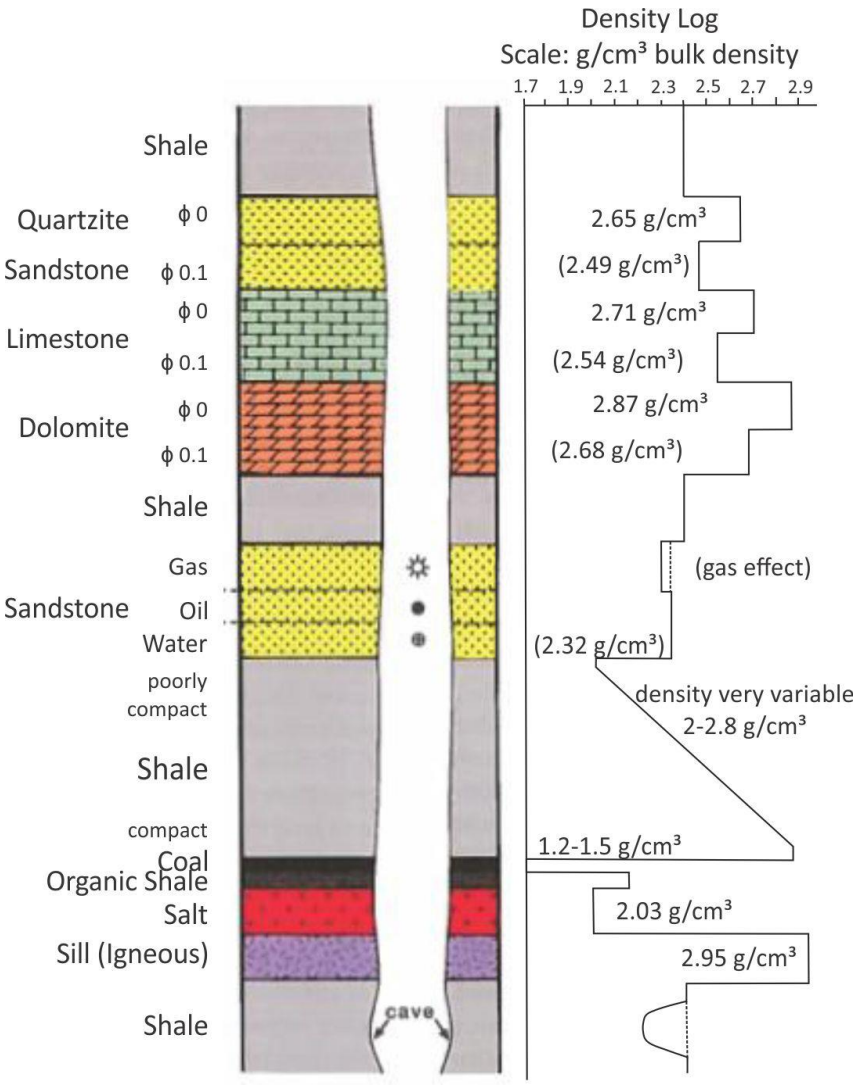

Figure 1.15 Typical density log for some common lithologies. Modified from Rider & Kennedy (2011).

1.5.2 The sonic log

The sonic log measures the acoustic characteristics of a formation often in the form of its interval transit time/slowness (Δt). In other words, it measures the formation's capacity to transmit sound waves. This is done by measuring the time it takes for a sound wave to travel a known distance within the formation. The sonic logging tool consists of one or two transmitters and several receivers where the distance between them is known. Δt is found by measuring the time it takes for a soundwave to travel along the formation from the source(s) to the receiver(s). Three wave types are detected in sonic logging; compressional, shear, and Stoneley. However, the former is mostly used. Figure 1.16 shows the sonic log for some common lithologies.

The sonic log measures the velocity, but it is often expressed as slowness or the interval transit time. The standard units for this is μs/ft. Typical values for formations in the subsurface range from 50-150 μs/ft. This is corresponds to approximately 6000-2000 m/s. Since the velocity in the common rock types have too much of a variation and overlap between types, recorded velocities are not a diagnostic tool for lithology. However, the velocity is very sensitive to changes in the texture.

The main use of sonic log is to aid seismic investigations. Accurate depth conversions and velocity profiles can be calculated by tying the well to the seismic. By combining it with the density log, an acoustic impedance log can be established, which later can be used to create a synthetic seismogram.

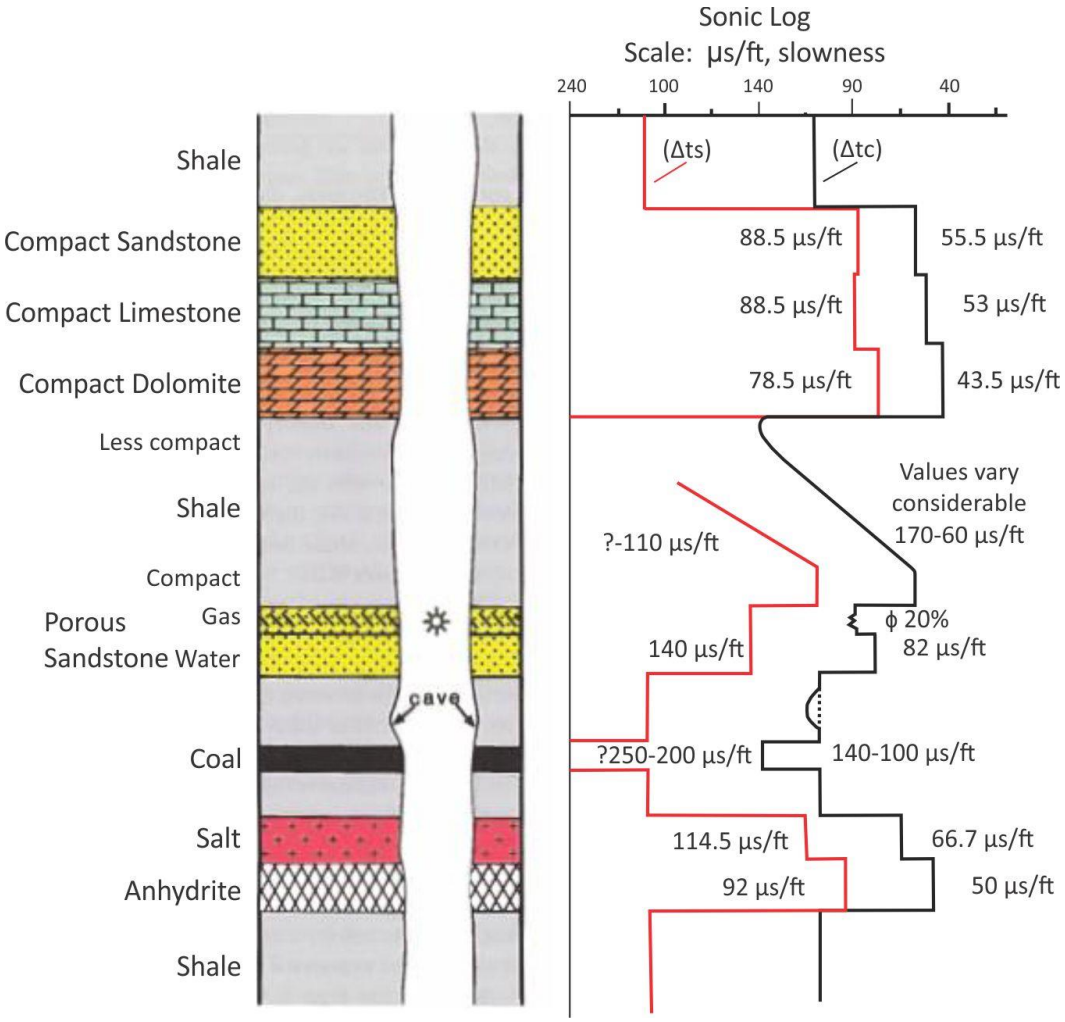

Figure 1.16 Typical sonic log for some common lithologies. Modified from Rider & Kennedy (2011).

1.5.3 The gamma ray log

The gamma ray log measures the natural gamma radioactivity from potassium, uranium and thorium in a formation. A normal log outputs the total count rate of these as it cannot distinguish between the individual elements. Most rocks, including metamorphic, igneous and sedimentary rocks contain traces of gamma-emitting elements, where the two former contains the most. Amongst the sedimentary rocks, shale exhibit the highest radioactivity. Because of this behaviour, the gamma log is often referred to as the “shale log”, even though it is not equivalent to the amount of shale content. Figure 1.17 shows the gamma ray log for some lithologies.

The gamma ray log is mainly used for correlation of different strata and it is often used to pick well tops while drilling. It is a good indicator of shale and it can be used to help identify lithology, key stratigraphic surfaces, facies, sequences and derive shale and mineral volume. The unit for the gamma ray log is the API (American Petroleum Institute) unit. According to Belknap et al. (1959) an API unit is defined as 1/200 of the difference between two reference units. An average shale usually reads 100 API units. Pure sandstones and carbonates normally have a low API unit (10-40 API) compared to shales. However, if they contain heavy minerals that are radioactive their associated API units can be higher than usual.

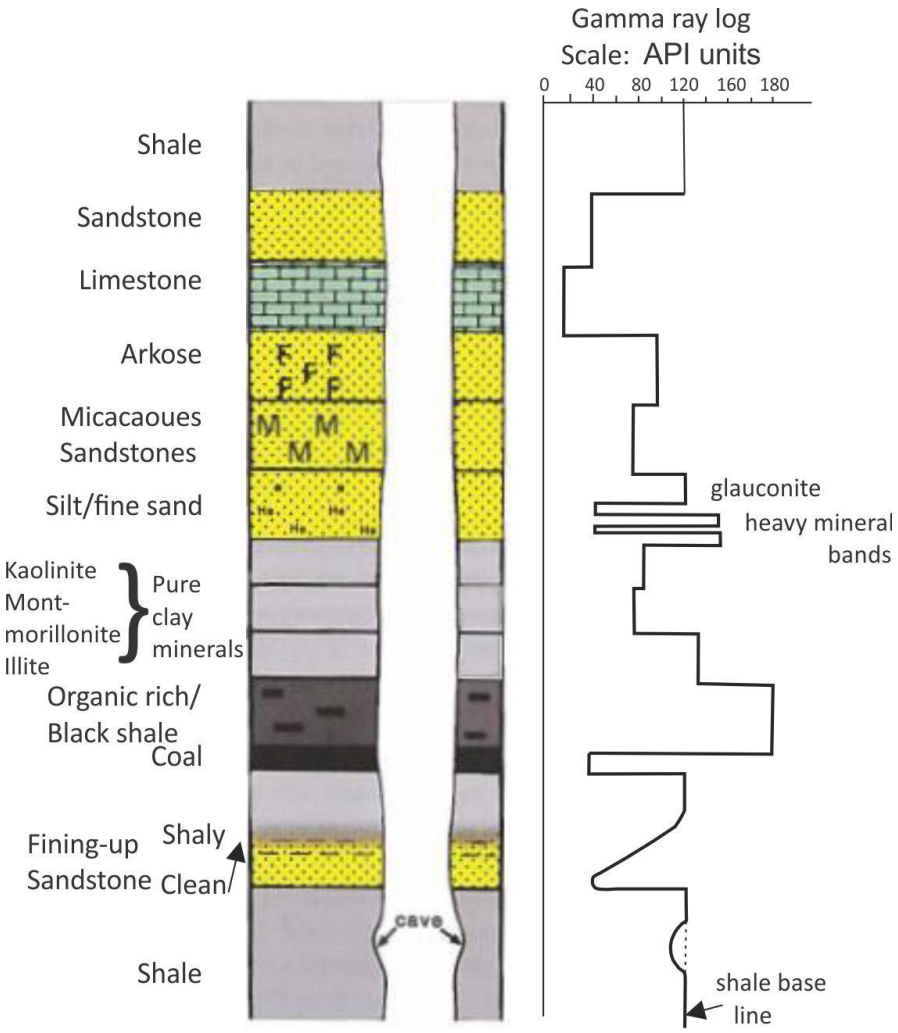

Figure 1.17 Typical gamma ray log from some common lithologies. Modified from Rider & Kennedy (2011).

1.5.4 The neutron log

The neutron log measures how a formation react to neutron bombardment. The tools work more or less in the same way as the tools used for density logs. There is a source that emits high energy neutrons into the formation and a receiver that measures the numbers of low energy neutrons that are re-emitted back. Emitted neutrons strongly respond on hydrogen in the formation. Therefore, the returning amount of neutrons strongly depend on the hydrogen content. In high porosity rocks, the neutrons are slowed down quickly and absorbed causing the count rate to be low. Vice versa, in low porosity rocks, the emitted neutrons are not absorbed as quickly and they travel further. Hence, the count rate will be higher (Schlumberger, 1994). Figure 1.18 shows how the neutron log may vary depending on lithology.

Hydrogen appears in all formation fluids (water, oil and gas), but not in all minerals. Because of this, the response from the neutron log could be correlated with porosity (Selley & Sonnenberg, 2015). However, shales often contain bound water in addition to free water. Free water is the formation fluid whereas bound water is the water that occurs in the crystal lattice or between clay minerals.

The log output/scale is given in neutron porosity units, which is an indication of the Hydrogen Index for the formation. It is given as either a percentage or fraction. Typical values for sandstones lie between 0-30% whereas shales, due to their bound water, have values between 25-75%. The neutron log is mainly used to derive porosities, but it can in combination with the density log be used to indicate subsurface lithologies and calculate shale volumes.

The neutron log is often plotted with the highest values to the left and lowest to the right (Fig. 1.18).

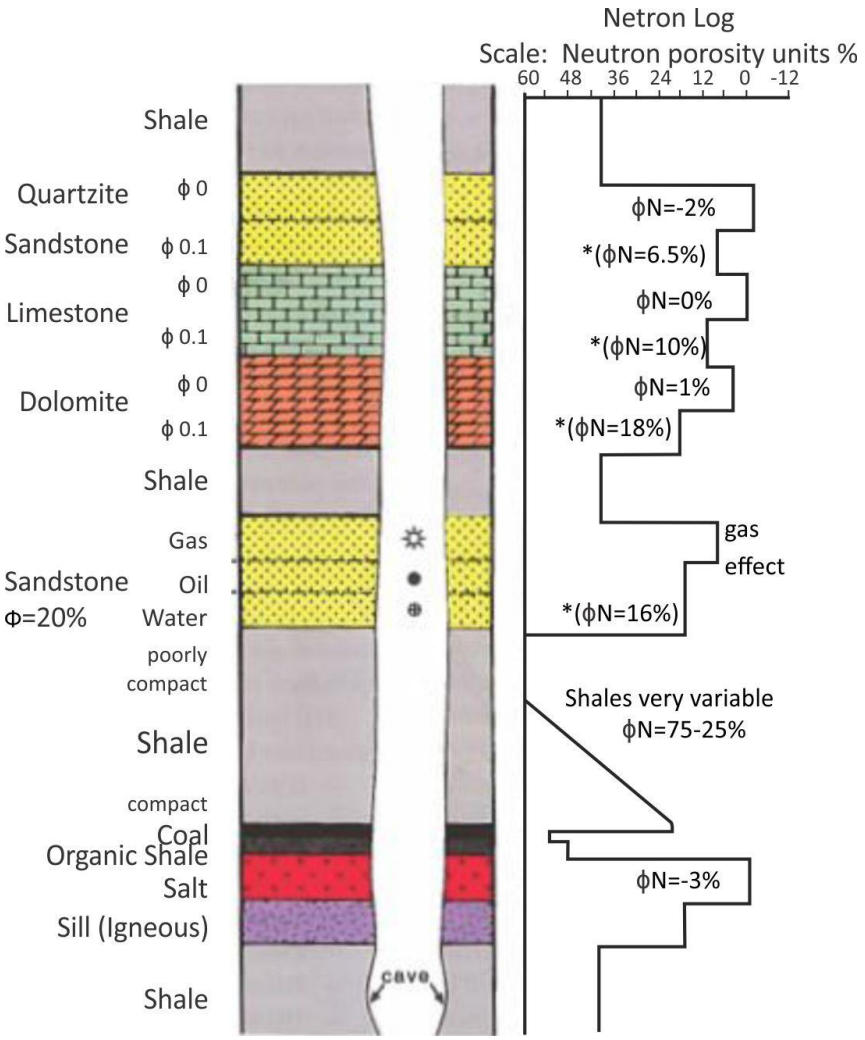

Figure 1.18 Typical neutron log for some common lithologies. Modified from Rider & Kennedy (2011).

1.5.5 The resistivity log

The resistivity log measures the ability of a formation to conduct electric currents. The lower the resistivity the easier it is to pass a current through it. Most of the fluids and minerals in the subsurface have high resistivities, except water. If a formation is porous and contains saline water the resistivity would be small because the water can conduct the current. If the same formation were to be filled with hydrocarbons, the resistivity would increase. Hydrocarbons are only one of many things that can give high resistivity values. A low porosity or low permeable formation could also give rise to high values. The resistivity depends on the formations lithology, texture, facies, and temperature of formation water, compaction and mineral content. Figure 1.19 shows a typical resistivity response for oil-, gas-, saltwater-, and freshwater-filled sandstones.

The resistivity in the formation can be measured in two ways. In the first way there is a direct connection between the formation and the tool where the current flows from the tool to the formation and back again. The other way induces electromagnetic fields in the formation which is measured or calculated based on the behaviour of the fields. Resistivity measurements are often divided into shallow, medium and deep, based on the distance from the borehole. This is due to when drilling, the drilling mud invade and mix with the formation fluid. The mixing develops a flushed and invaded zone in which most or parts of the formation fluid has been displaced. The shallow and medium measurements correspond to the flushed and invaded zone, whereas the deep most likely represents the true resistivity of the formation.

The unit for the resistivity log is ohm meter (ohm-m) and it usually ranges between 0.2-200 ohm-m. The log is mainly used to define the water saturation, but it can be combined with other logs to say something about the characteristics of the formations in the subsurface.

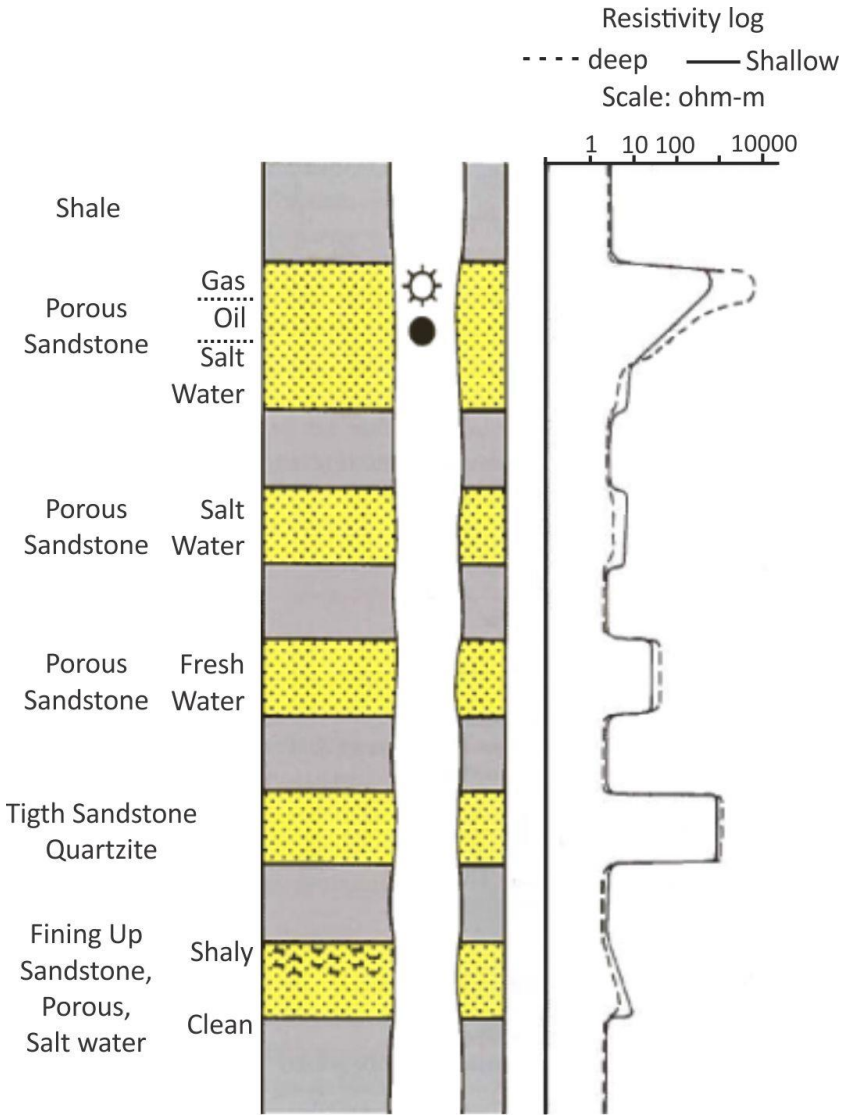

Figure 1.19 Typical resistivity log. Modified from Rider & Kennedy (2011).

2 Study Area

2.1 Introduction

The study area is located in the Sørvestsnaget basin. Figure 2.1 shows the location of the study area in the southwestern Barents Sea. The Barents Sea is a large epicontinental sea with water depths mainly shallower than 500 m (Dore, 1995; Smelror et al., 2009). It covers an area of approximately 1.4 million km^2, making it one of the largest shelf areas in the world. The shelf is bounded by the coasts of Northern Norway and Russia to the south, the Svalbard archipelagos and Franz Josef Land to the north, the Norwegian-Greenland Sea to the west and Novaya Zemlya to the east, separating the Barents Sea from the Kara Sea. A north-south trending monoclinal structure situated approximately along the political border between Norway and Russia, separates the Barents Sea into two main provinces, the eastern and western province (Worsley, 2008; Smelror et al., 2009).

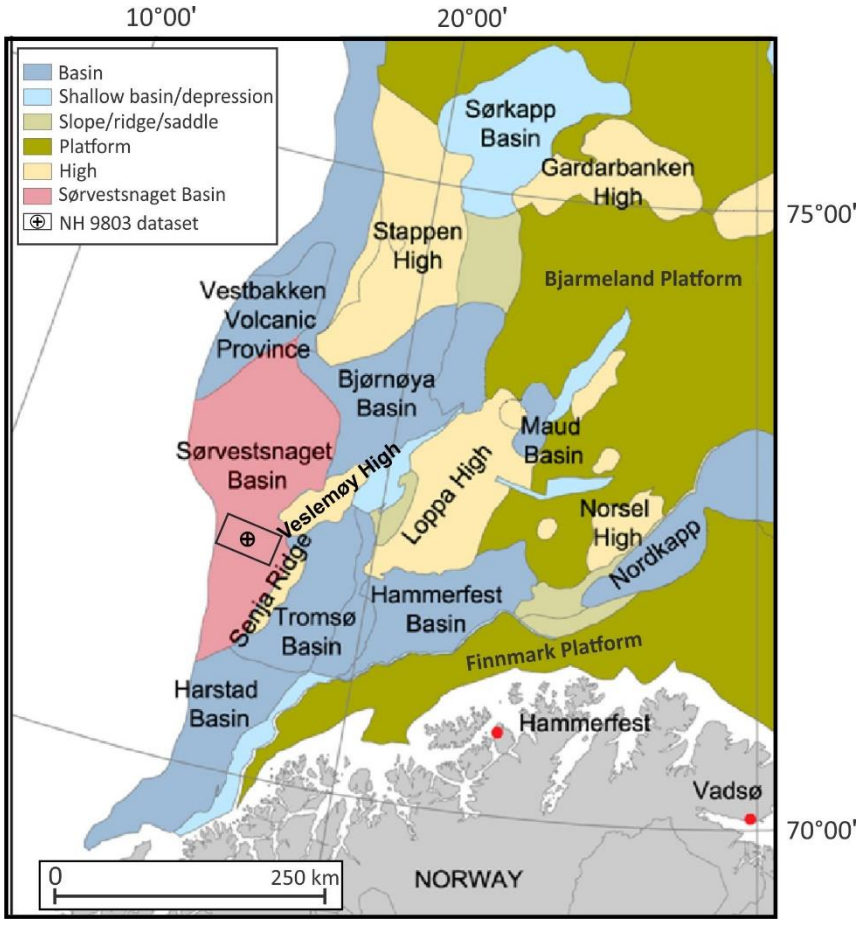

Figure 2.1 Location of the Sørvestsnaget Basin in which the study area is located. Modified from Henriksen et al. (2011).

2.2 Tectonic history

The geological history of the Barents Sea commenced in late Paleozoic. A combination of many large-scale processes controlled by plate movements and varying depositional and climatic conditions has led to several periods with extension, subsidence, uplift and erosion, and to the present day configuration of the Barents Sea (Smelror et al., 2009). The geology of the eastern and western provinces is different. The tectonic histories of Novaya Zemlya and the Timan-Pechora basin together with the Uralian Orogeny have influenced the geology of the eastern parts, whereas the Caledonian Orogeny and major rifting events have influenced the western parts (Worsley, 2008). The major post-Caledonian rifting phases took place in (1) Late Devonian-Carboniferous, (2) Middle Jurassic-Early Cretaceous and (3) Early Paleogene, but minor tectonic events have taken place in between (Faleide et al., 1993; Kristensen et al., 2017).

The western Barents Sea comprises three distinct regions (Faleide et al., 1993):

1. The Svalbard platform to the north
2. A basin province between the Norwegian coast and Svalbard characterised by sub-basins and highs.
3. A continental margin towards the west

The continental margin consists of three main segments related to the Cenozoic opening of the Norwegian-Greenland Sea (Faleide et al., 1993). It is divided into

1. A southern sheared margin along the Senja Fracture Zone
2. A central rift complex associated with volcanism (Vestbakken Volcanic Province)
3. A northern, initially sheared and later rifted margin along the Hornsund Fault Zone

Figure 2.2 shows the three distinct regions and main segments of the continental margin in the western Barents Sea. In addition some of the main structural elements are shown. Since the study area in this thesis is located in the southwestern Barents Sea, the history of the eastern province will not be described to the same extent.

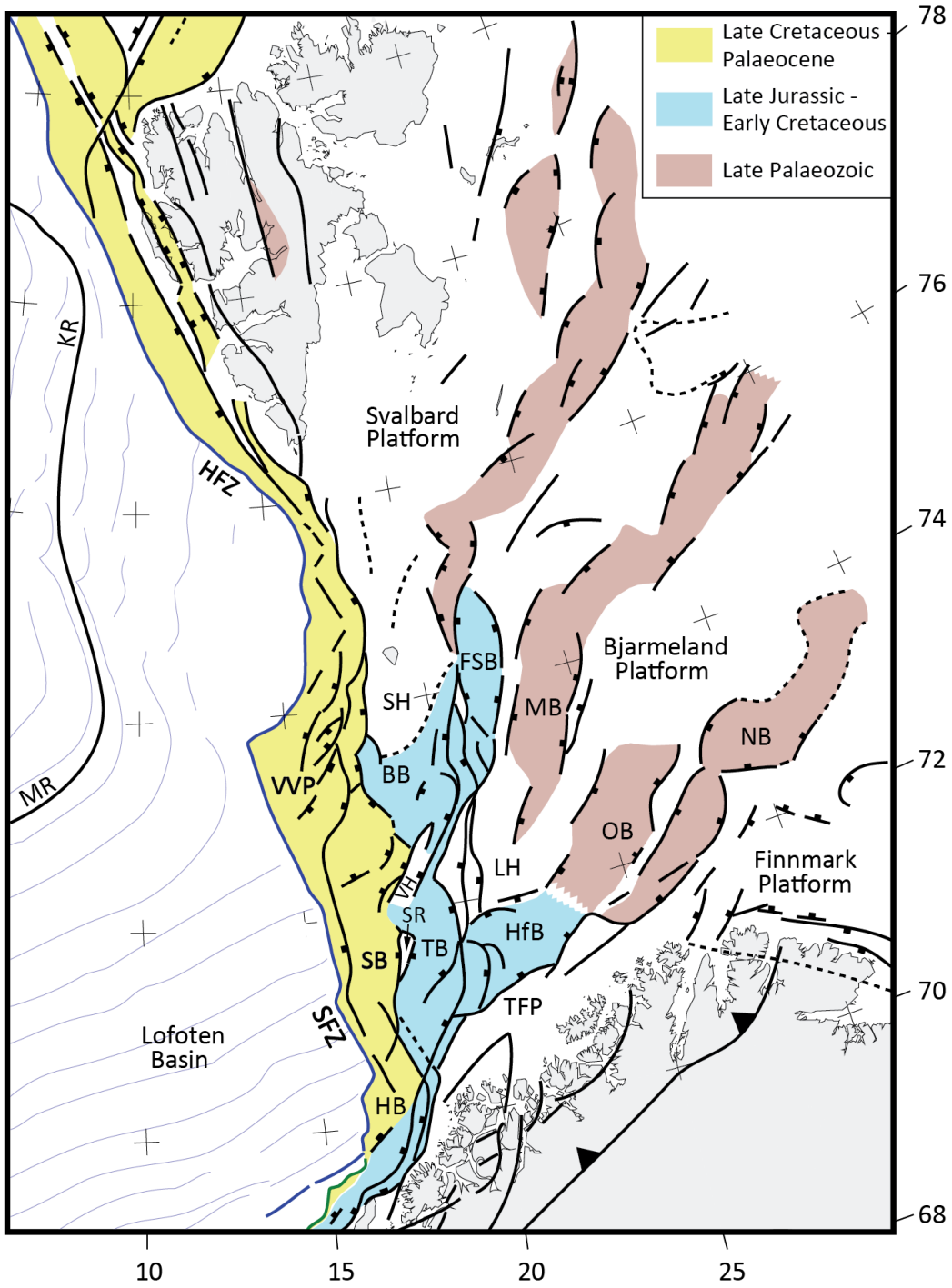

Figure 2.2 Main structure elements in the western Barents Sea. The colors indicate the time periods in which they were mainly formed. BB = Bjørnøya Basin, FSB = Fingerdjupet Sub-basin, HB = Harstad Basin, HfB = Hammerfest Basin, HFZ = Hornsund Fault Zone, KR = Knipovich Ridge, LH = Loppa High, MB = Maud Basin, MR = Mohns Ridge, NB = Nordkapp Basin, OB = Ottar Basin, SB = Sørvestsnaget Basin, SFZ = Senja Fracture Zone, SH = Stappen High, SR = Senja Ridge, TB = Tromsø Basin, TFP = Troms-Finnmark Platform, VH = Veslemøy High, VVP = Vestbakken Volcanic Province. Modified Faleide et al. (2015).

2.2.1 Paleozoic

Approximately 425 million years ago, the collision between Laurentia and Baltica resulted in the formation of the Caledonian orogeny and the Laurasian continent. The orogeny covered large parts of the western Barents Sea whereas the eastern province consisted of a passive carbonate margin with a shallow to deep water depositional environment (Smelror et al., 2009). When the Caledonian orogeny culminated in early Devonian, the tectonic regime changed from compressional to extensional (Fossen et al., 2006). This led to a reactivation of faults along weak zones in the Caledonian thrust nappe. Along the western margin a N-S structural trend was established. Further east, in the area surrounding the Nordkapp Basin, a NE-SW trend was established (Faleide et al., 1984; Smelror et al., 2009). Late Devonian to early Carboniferous in the western province was characterised with an extensive erosion of the Caledonians (Smelror et al., 2009). In the eastern province, the passive margin evolved into an active margin, which in late Carboniferous through Permian resulted in the closure of the Uralian Ocean and a collision between Laurasia and Western Siberia (Smelror et al., 2009).

In the western province, a 300 km wide rift zone extending around 600 km in a northeasterly direction was formed during the late Devonian-Carboniferous rifting phase. It was a direct continuation of the Atlantic Rift between Norway and Greenland and it formed an array of fault bounded basins and highs with orientations varying from NE-SW in the main rift zone and N-S in the present day western margin e.g. the Nordkapp, Maud, Ottar, Tromsø and Bjørnøya Basins (Gudlaugsson et al., 1998). As the rift phase ended, the Barents Sea area drifted northwards from ca. 20°N in Carboniferous to 40°N in late Permian, passing through several climate zones (Torsvik et al., 2002). When the area gradually moved towards north, fluctuating sea levels combined with a regional subsidence and a semi-arid climate led to an extensive warm-water carbonate platform covering large parts of the Barents Sea from late carboniferous to early Permian (Worsley, 2008). In the newly formed basins, thick successions of evaporates where deposited during low stands. Towards the end of Paleozoic, the seaway connection to the Tethys Sea was closed, and the development of the Urals commenced (Worsley, 2008).

2.2.2 Mesozoic

The Uralian orogeny culminated approximately 240 million years ago, closing the marine connection to the south. At this point, the Barents Sea region became a part of a massive Permian-Triassic sag basin (Gudlaugsson et al., 1998). The whole area was characterised by a regional subsidence and large amounts of sedimentation sourced from the Uralian highlands in the east, the Fennoscandia Shield in the south and local exposed areas to the north and northwest occurred (Smelror et al., 2009). Most of the western province was tectonically quiet in the Triassic, but a narrow zone in the N-S oriented part of the rift system experienced renewed faulting, uplift and erosion (Smelror et al., 2009; Faleide et al., 2015).

From middle Mesozoic, the structural evolution of the southwestern Barents Sea comprised two main phases, (1) Late Mesozoic rifting and basin formation and (2) Early Paleogene rifting and the opening of the Norwegian-Greenland Sea (Faleide et al., 1993).

The rifting associated with the North Atlantic rift reached the southwestern Barents Sea margin during late Jurassic. It occurred along old east to north-east trending structural lineaments in the Bjørnøya and Hammerfest basins, rotating fault blocks and creating restricted basins (Nøttvedt & Johannessen, 2006). The Tromsø, Bjørnøya and Harstad basins became prominent features during the Late Jurassic to Early Cretaceous structuring of the southwestern Barents Sea (Faleide et al., 1993). The rift phase was followed by a segmentation into sub-basins and a rapid subsidence. At the northern margin, the rifting and opening of the Amerasian Basin in Early Cretaceous caused an uplift and minor tilting of the northern parts of the Barents Sea region that continued throughout late Early Cretaceous (Smelror et al., 2009).

Continental breakup commenced in Late Cretaceous and the De Geer Zone, a dextral megashear zone connecting the North Atlantic rift with the Arctic rift, was developed. Strike-slip movements and oblique extension along the zone led to the formation of pull-apart basins and thick Cretaceous deposits, especially in the Sørvestsnaget Basin (Faleide et al., 1993).

2.2.3 Cenozoic

In early Cenozoic, at the transition between Paleocene and Eocene, seafloor spreading commenced in both the Eurasia Basin and the southern parts of the Norwegian-Greenland Sea. As a consequence, the western margin of the Barents Sea developed as a shear margin within the De Geer Zone (Faleide et al., 1993). The final opening of the Norwegian-Greenland Sea did not occur before the transition from Eocene and Oligocene when the initially sheared margin in the north evolved into a combined shear-rift margin. Prior to that, Greenland moved along the western margin and Svalbard, due to the opening of the Labrador Sea on the other side of Greenland, causing folding and thrusting in western Spitsbergen (Talwani & Eldholm, 1977). The direction of the early opening was at a small angle with the Hornsund Fault Zone and Senja Fracture Zone, causing transform movements with local transpression and transtention along the zones. Basins along the margin were uplifted and subsided due to local movements (Faleide et al., 1993). The central parts of the rift margin experienced volcanism due to rifting, leading to the formation of the Vestbakken Volcanic Province. The province consist of a thick oceanic crust and thin continental crust covered by a mixture of sediments and volcanics (Faleide et al., 1991). During Oligocene, the margin became tectonically quiet. Subsequently, oceanic crust has formed along the margin, followed by subsidence (Faleide et al., 1993).

Through late Cenozoic, the Barents Sea was exposed to several glaciations. Already in late Miocene there were small ice caps in the area, but the onset of larger glaciations did not occur before Late Pliocene (Knies et al., 2009). The onset is marked by an upper regional unconformity (URU) separating underlying Mesozoic-Paleogene sediments and overlying glacial sediments (Smelror et al., 2009). Cenozoic was characterized by an oscillating ice front where the ice moved forward and retreated several times. During interglacials, isostatic rebound caused an uplift of the area. The following erosion led to large amounts of sediments being eroded and deposited along the margin in big trough mouth fans. The total Cenozoic erosion from the whole Barents Sea ranges from 500-3500m with the greatest erosion being in the northwestern parts (Hjelstuen et al., 1996) . Throughout Cenozoic, the glaciers modified the seafloor and developed the present day morphology of the area with banks, troughs and other glacial structures (Faleide et al., 1996).

2.3 Stratigraphy

The stratigraphy of the Barents Sea spans from Late Paleozoic to Quaternary. Information regarding the basement is scarce. The western basement is believed to have consolidated during the Caledonian Orogeny (Gudlaugsson et al., 1998), whereas the eastern basement consists of Precambrian rocks that were deformed during the Timanian and Uralian orogenys (Marello et al., 2013). Since late Devonian several lithostratigraphic units have been deposited in the Barents Sea, reflecting periods with different climatic and depositional regimes (Worsley, 2008). Figure 2.3 summarises the stratigraphy and main tectonic events in the western Barents Sea.

2.3.1 Paleozoic

The Barents Sea experienced crustal extension and the formation of major rifting structures from Middle to Late Paleozoic. During this interval four lithostratigraphic groups were deposited. Late Devonian to early Carboniferous was characterised by a humid climate, fluvial/alluvial plains, marshes and extensive erosion of the Caledonians (Smelror et al., 2009). At this time, the Billefjorden Group (Fig. 2.3) was deposited as a rift-infill sequence consisting of continental clastics with a coarsening upward trend (Worsley, 2008). The group is characterised by an overall transition from continental fluvial dominated deposits to marginal marine deposits (Larssen et al., 2002).

The humid climate was followed by a more arid climate as the area drifted northwards during Carboniferous. This led to the deposition of the Gipsdalen Group (Fig. 2.3) consisting of shallow marine warm-water carbonates, local silisiclastics and sabkha evaporites on the shallow platforms and halite in the deeper basins (Worsley, 2008). During mid-Permian, a major flooding event combined with more temperate conditions mark the onset of the Bjarmeland Group(Fig. 2.3), consisting of cold water carbonates (Larssen et al., 2002). Towards the end of Paleozoic, the climate shifted from arid to temperate. This in combination with the closure of the seaway connection to the Tethys Sea and the development of the Urals replaced the warm water carbonate regime with a siliciclastic regime (Tempelfjorden Group) (Fig. 2.3) (Worsley, 2008).

2.3.2 Mesozoic

Most of the western province was tectonically quiet during Triassic, and the area was characterised by regional subsidence. This in combination with regression and erosion led to thick Triassic deposits, up to 1500m in the southwestern Barents Sea (Worsley, 2008). The Early to Middle Triassic lithology was dominated by sandstones, siltstones and shales deposited in a delta to shoreface environment, comprising the Sassendalen Group (Fig. 2.3) (Worsley, 2008).

In early Late Triassic the Barents Sea experienced a regional regression and large areas of the region was uplifted and subsequently eroded. The southwestern area was characterised by a westward progradation of near-shore and coastal depositional environments, resulting in the deposition of immature sandstones in the Kapp Toscana Group (Fig. 2.3) (Worsley, 2008). The regression was followed by regional transgression that flooded much of the area. The sedimentation and subsidence rates decreased, and coastal to shallow marine environments were established throughout the region (Worsley, 2008). Mature and well sorted sandstones deposited during this time comprise excellent reservoir units within the Kapp Toscana Group (Halland et al., 2014). A regional transgression in Bathonian led to the deposition of anoxic black shales in restricted basins throughout Late Jurassic (Hekkingen formation) (Fig. 2.3) (Faleide et al., 1993; Halland et al., 2014).

A change in depositional environment marks the transition between Jurassic and Cretaceous. A tectonically induced low stand in relative sea-level combined with major rifting formed a regional unconformity known as the “Late Kimmerian Unconformity” (Faleide et al., 1993). Marine environments replaced the anoxic environments, and the Early Cretaceous was dominated by clay deposition with thin limestone and dolomite layers in the basins (Kolje and Knurr formations) (Fig. 2.3) and carbonate deposition on the platforms (Smelror et al., 2009). The uplift of the northern parts during Aptian-Albian times, resulted in the deposition of thick successions of shales, mudstones and siltstones (Kolmule formation) (Fig. 2.3). Throughout Late Cretaceous the uplift continued, resulting in thick deposits in the western basins known as the Nygrunnen group (Fig. 2.3) (Worsley, 2008). The Late Cretaceous and Paleogene rocks have been partly removed due to the Paleogene uplift and the following erosion (Ohm et al., 2008)

2.3.3 Cenozoic

The Barents shelf was subject to transpression and transtension during the opening of the Norwegian Greenland Sea in Paleogene. During this time, claystones of the Torsk formation (Sotbakken Group) were deposited in the western basins in an open deep marine shelf environment (Worsley et al., 1988). The late Neogene to Quaternary Nordland group, consisting of sandstones and claystones, lies unconformable on top of the Torsk formation (Fig. 2.3) (Worsley et al., 1988).

A regional unconformity, known as the Upper Regional Unconformity (URU), marks the onset of the northern hemisphere glaciations. The glaciations resulted in several periods with uplift, erosion and redeposition on the slope. As a result, the southwestern Barents Sea margin prograded 30-40km westward (Faleide et al., 1996). Three main packages (GI-GIII) and seven regional reflectors have been identified within the Cenozoic succession (Faleide et al., 1996). The sediment packages comprise the Naust formation of the Nordland Group (Andreassen et al., 2007b). The deepest package, GI, represents a glaciomarine environment, whereas GII and GIII represents mass-movement deposits related to grounded glaciers (Andreassen et al., 2007a).

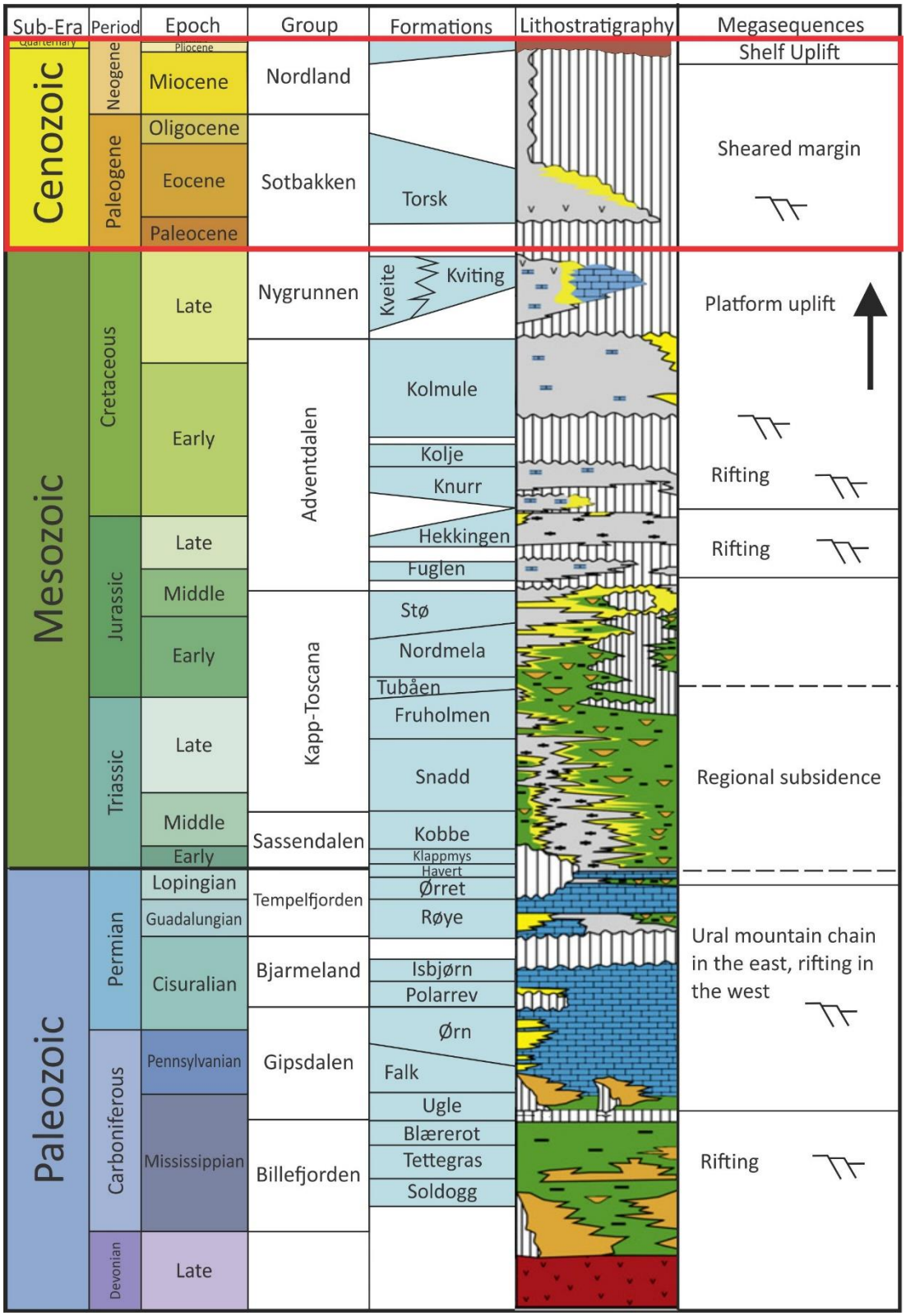

Figure 2.3 Stratigraphy of the western Barents Sea. The red box marks the age of studied sediments in the NH9803 dataset. Modified from Glorstad-Clark et al. (2010).

3 Data and methodology

3.1 Seismic data

The seismic data used in this thesis consists of a 3D seismic cube referred to as NH9803, which is located in the Sørvestsnaget Basin (fig 3.1). The data was acquired in 1998 by Norsk Hydro to look at potential Cenozoic prospects (Ryseth et al., 2003). The survey was acquired in a NW-SE direction and it consists of 971 inlines and 2167 crosslines covering an area of approximately 2000 km^2. Using the Society of Exploration Geophysicists (SEG) polarity standard, the polarity of the dataset can be described as a zero phase signal with a normal polarity (Fig.3.2a) (Sheriff, 2002). The seafloor reflection is used to identify the polarity since this reflection coefficient is always positive (fig 3.2b). An increase in AI is represented with a peak (red).

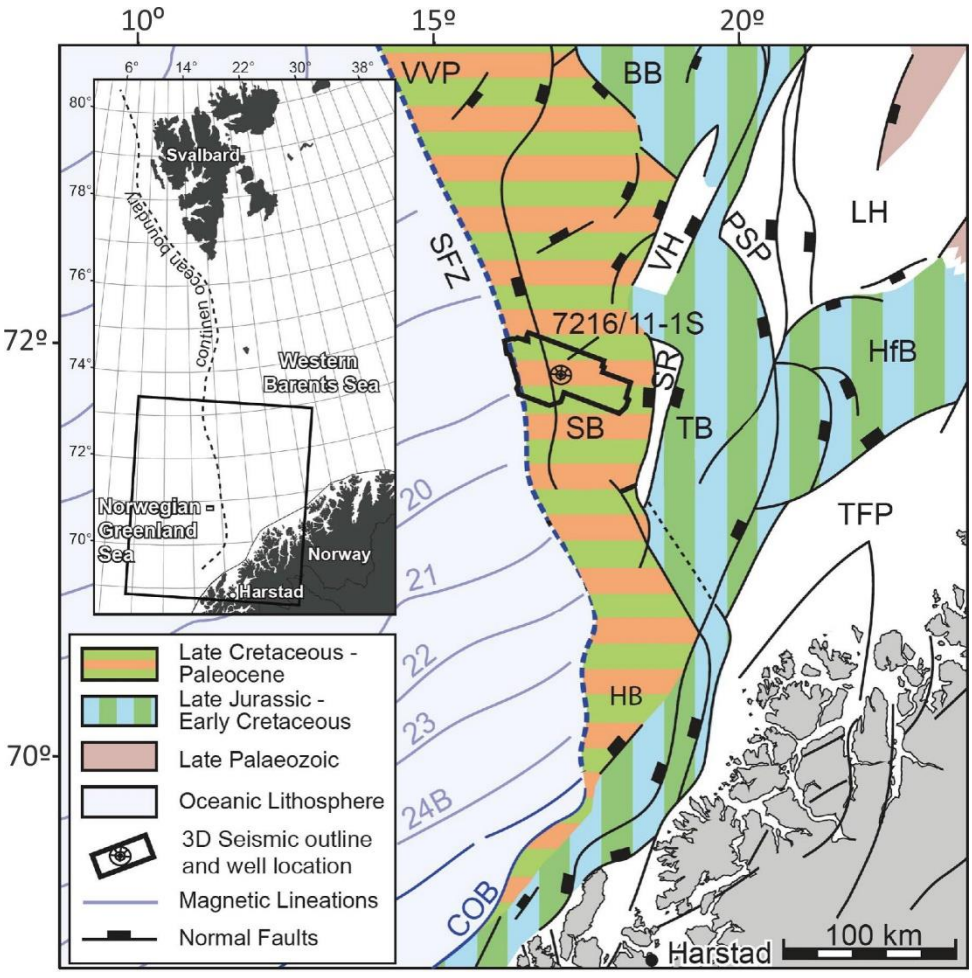

Figure 3.1 Location of the NH9803 dataset and 7216-11-1S well. Modified from Kristensen et al. (2017).

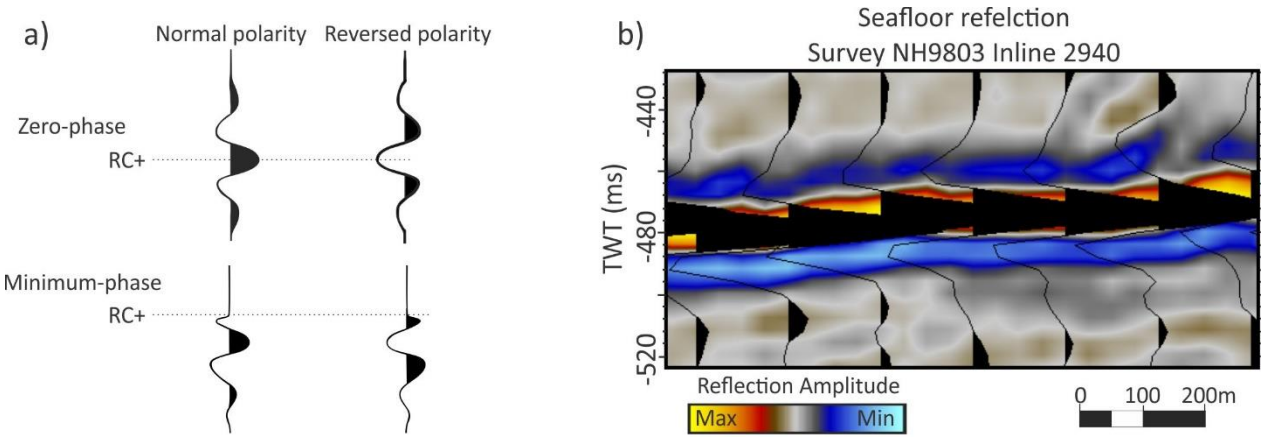

Figure 3.2 a) SEG polarity standard for seismic signals. Based on Sheriff (2002). b) Zero-phase polarity for the seafloor reflection in this seismic dataset.

3.1.1 Resolution of NH9803 dataset

The frequency at chosen depths can be approximated using the inspector tool and its frequency spectrum in Petrel. Combining this information with the sonic log from well 7216-11-1S and equation (1.10), (1.11) and (1.13)(1.12), it is possible to calculate the approximate resolution of the NH9803 dataset. From the 7216-11-1S well, four well tops situated at different depths were chosen as reference points; Pliocene, Miocene and R2. Their associated velocities from the sonic log were picked and converted from µs/ft to m/s. Table 3.1 shows a summary of the reference points and their associated depths, frequencies and velocities. Since equation (1.12) assumes perfectly migrated data, the resolution column in table 3.1 concerns both the vertical and horizontal aspects.

Table 3.1 Summary of the data used in calculating the resolution of the NH 9803 dataset.

Horizon	Depth (m)	Velocity (m/s)	Frequency (Hz)	Resolution (m)
Pliocene	≈ 767	≈ 2000	≈ 40	≈ 13
Miocene	≈ 2270	≈ 2644	≈ 27	≈ 24
R2	≈ 2912	≈ 3155	≈ 24	≈ 33

3.1.2 Artefacts

The seismic survey contains artefacts in the form of acquisition footprints. Acquisition footprints are according to Sheriff (2002) "*patterns in the data caused by the acquisition method*". In the NH 9803 dataset the survey footprints can be seen as repetitive features parallel to the inline direction.

3.2 Well data

One well is used in this study. Well 7216-11-1S is located in the Sørvestsnaget Basin (fig 3.1). It is an exploration well drilled by Norsk Hydro in 2000. Its primary objective was to test a Cenozoic structural closure (NPD, 2003). The well was spudded in a water depth of 361 mMSL and terminated in Paleocene rocks at a total depth of 4239 mMD (TVD was 3733 mMD due to a deviated borehole). The Kelly Bushing measured 24m and the bottom hole temperature was 114°C (NPD, 2003). There were no significant shows of hydrocarbons and the well was abandoned as a dry well. However, it did encounter a 214 m thick sandstone unit with excellent reservoir qualities (NPD, 2003; Henriksen et al., 2011). In the NH 9083 dataset, the well is located on inline 2940 and xline 4882.

The well has a total of five logs. The logs and associated values and abbreviations are summarised in table 3.2. Some of the logs do not have values for the whole well and there are some discontinuities within them, resulting in small intervals where there are no measurements.

Table 3.2 Logs from well 7216-11-1S, their abbreviations, values and range limit.

Log type	Abbreviations	Value range and unit
Gamma ray	GR	0-250 API
Sonic	AC	35-180 µs/ft
Bulk density	DEN	1.95-2.95 g/cm^3
Neutron porosity	NEU	-0.15-0.50 m^3/m^3
Deep resistivity	RDEP	0.2 – 200 ohm.m
Medium resistivity	RMED	0.2 – 200 ohm.m

The well has been studied before and a stratigraphy for the well has been established. Ryseth et al. (2003) divided the well into nine subunits based on lithology and age. Some of the already established results, such as well tops, will be further used in this thesis. All of the well tops are inserted based on the work by Ryseth et al. (2003). These are summarised in table 3.3.

Table 3.3 Summary of the well tops and their respective depths.

Horizon	Depth (MD)
Seabed	≈ 385
Miocene	≈ 2270
R2	≈ 2912
R1	≈ 3126
Early Eocene	≈ 3170

3.3 Interpretation methods

3.3.1 Seismic and well data

Both the seismic and well data used in this study is visualised and interpreted in the Petrel 2016 software from Schlumberger. The software contains a number of tools and features that are used to analyse both well data and seismic. For the geological model, only areas in close proximity to the well are used. This is achieved by cropping the seismic to a desired area surrounding the well. The well data and logs are displayed in measured depth (MD), which means that the distance is measured along the path of the borehole and that it takes into the account the Kelly Bushing. This is the distance between sealevel and the rotary table of the platform deck

3.3.2 Model

All modelling has been performed using Matlab®. The basis of one of the scripts has been supplied by the main supervisor. The other ones are made by the author of this thesis. Some of the scripts have been included in Appendix D at the end of this thesis.

4 Main observations

The first part of this chapter consists of a description of observations made in the NH 9803 dataset. This provides a regional description of the geology in the dataset. Further, the NH 9803 cube is cropped to a smaller volume surrounding well 7216/11-1S to make a geological model based on the observations. At the end, each unit in the model will be given certain parameters which is derived from logs in well 7216/11-1S.

4.1 Seismic observations

The Cenozoic succession in the seismic has been divided into three main units based on five well tops (Ryseth et al., 2003) from well 7216/11-1S as guidelines (Fig. 4.1). These are bounded by the Early Eocene, Reflector 1, Reflector 2, Miocene and Seafloor well tops. The thickness and internal seismic characteristics of the units varies.

The Seafloor is the only reflector mapped throughout the NH 9803 dataset. At some point, the rest of the reflectors either disappear, become too discontinuous, and/or too weak to interpret. In the following chapter, the boundary reflectors and the internal characteristics of the units will be described.

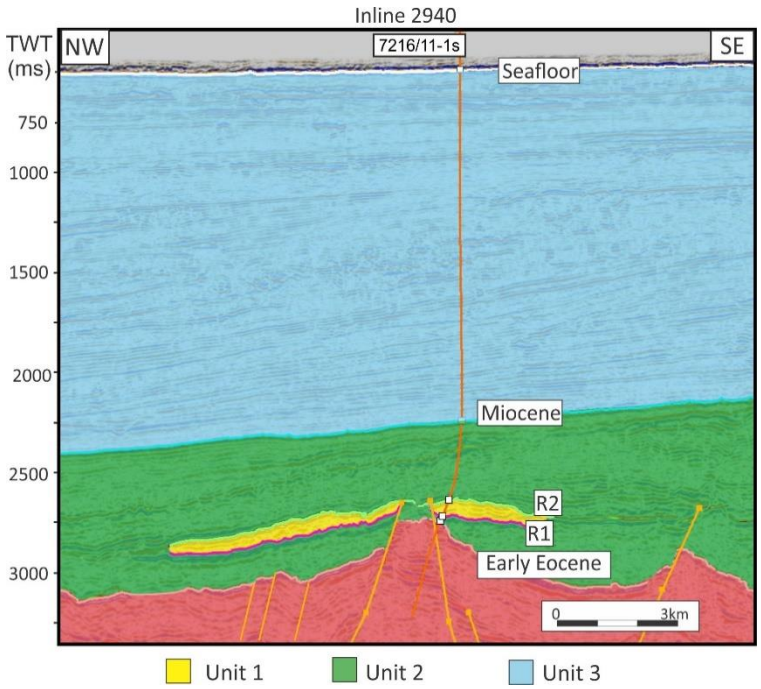

Figure 4.1 Main reflectors and units from the seismic.

4.2 Main reflectors

4.2.1 Reflector 1 (R1)

Representing the base of Unit 1, Reflector 1 is located between 2680-2780 ms (twt) (Fig. 4.2a). Overall, it has a slightly concave shape in both the NW-SE and SW-NE direction (fig 4.2c-e). The reflector is also gently dipping towards southeast. Towards northwest it is bounded by a fault and towards southeast it terminates against Reflector 2 (fig 4.2c). The reflector has an intermediate to strong RC and is generally continuous. It lies between 24-235 ms above the Early Eocene reflector. In some areas, the reflector is faulted (Fig. 4.2d).

4.2.2 Reflector 2 (R2)

Reflector 2 represents the top of Unit 1 and is located between 2620-2730ms ms (twt). It has an overall gently convex shape and it is bounded by a fault to the northwest and R1 to the southeast (fig 4.2c/d). It has a gentle deepening trend towards southeast. The reflector has a strong to intermediate RC and is mainly continuous. At the most, it lies approximately 100ms (twt) above R1. As with R1, R2 is also faulted (fig 4.2b/d).

The fault that both R1 and R2 terminates against towards northwest is the boundary towards an uplifted area on the seismic. Both R1 and R2 are present on the other side of the elevated area. These continuations will not be discussed.

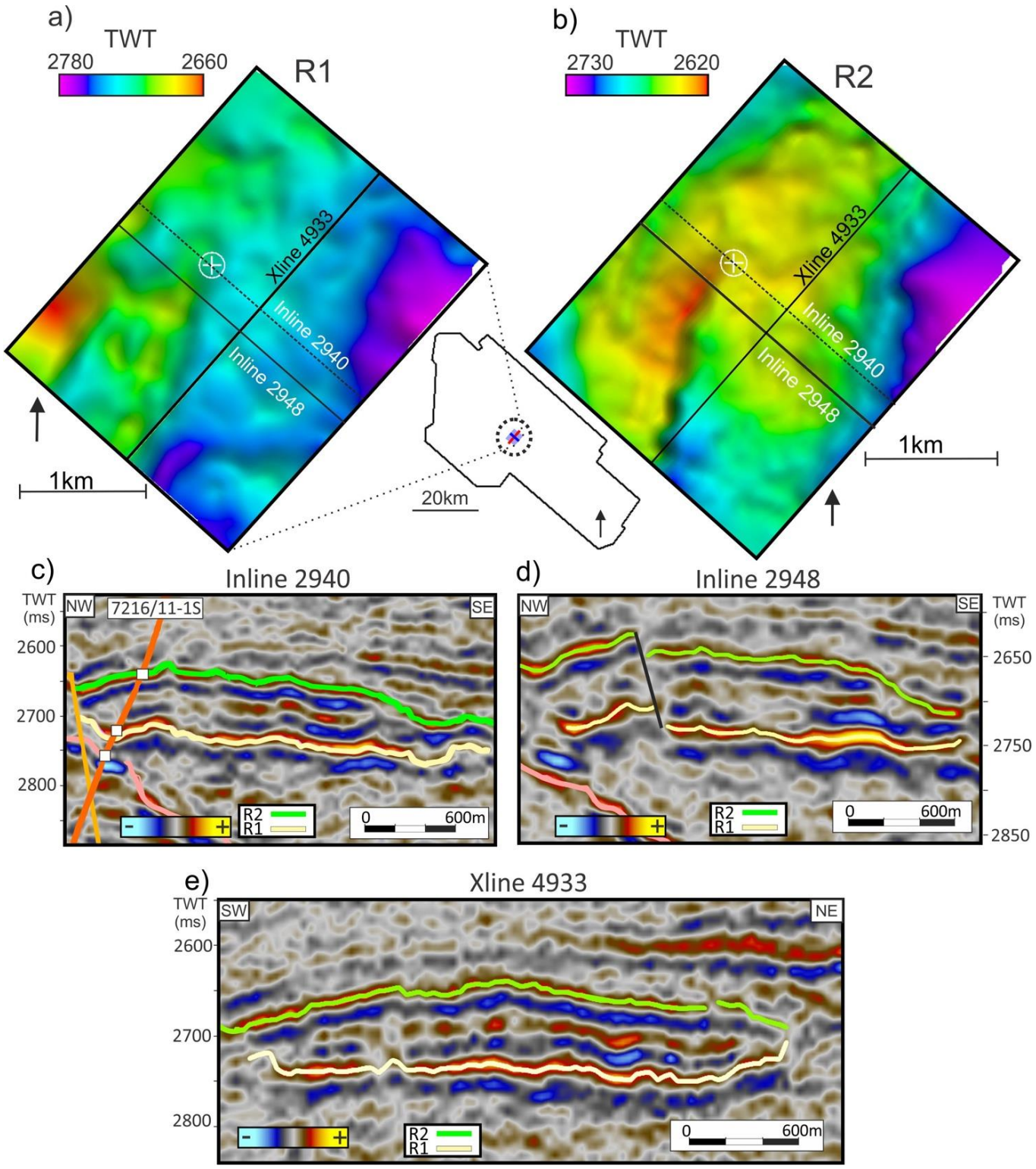

Figure 4.2 a) Time structure map of R1. b) Time structure map of R2. c) Seismic inline 2940 showing the slightly dipping concave and convex shape of the R1 and R2 reflectors, respectively. d) Seismic inline 2948 showing the faulted R1 and R2 reflectors. e) Xline 4933 showing the slightly concave and convex shape of the R1 and R2 reflectors, respectively.

4.2.3 Early Eocene

The Early Eocene reflector which represents the lower boundary of Unit 2, is located at two-way-travel times between 2700-3400 ms (Fig. 4.3a). The reflector varies between displaying a strong and intermediate positive RC, and between being continuous and discontinuous. Major faults have divided the reflector into several segments. Some of these are uplifted while others are dipping mainly in a southeastern direction (fig 4.3b). Due to the discontinuous characteristics of the reflector and generally poor data quality, it is hard to follow the reflector throughout the dataset. This study does not consider the reflectors beneath Early Eocene.

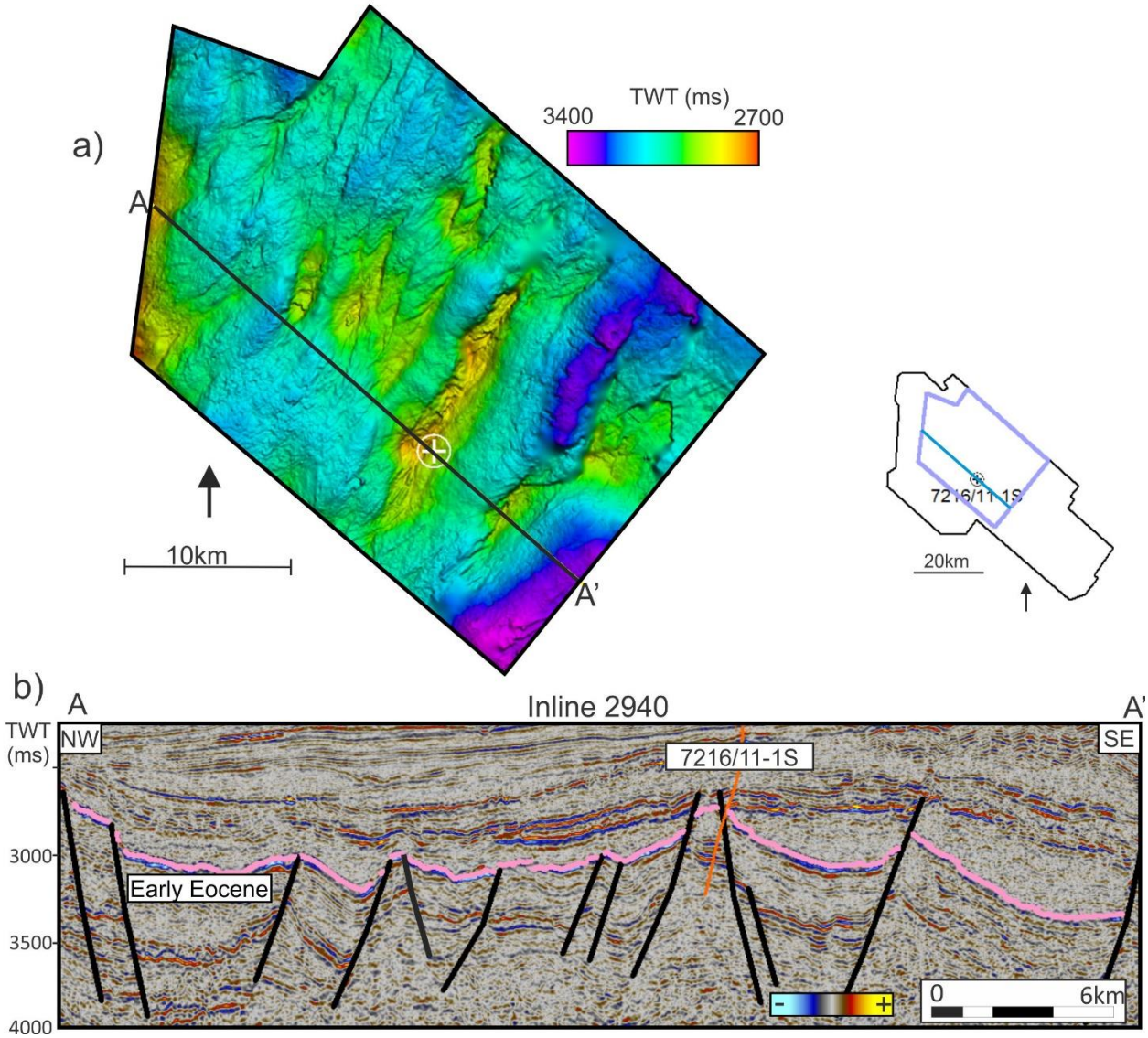

Figure 4.3 a) Time structure map of the Early Eocene reflector. b) Seismic section showing the faulted early Eocene reflector.

4.2.4 Miocene reflector

The Miocene reflector represents the upper boundary of Unit 2 and lower boundary of Unit 3. Towards east, it is defined at a time of 1700ms (twt). Towards the west it has a deepening trend where it reaches a maximum time of approximately 2500ms (twt) (fig 4.4a). The Miocene reflector has a low RC and varies between being continuous and discontinuous. Towards the southeast, the reflector disappears when it encounters a huge dome structure. The reflector is approximately subparallel with the overlying reflectors. Some of the underlying reflectors toplap the Miocene reflector (see Fig. 4.8b).

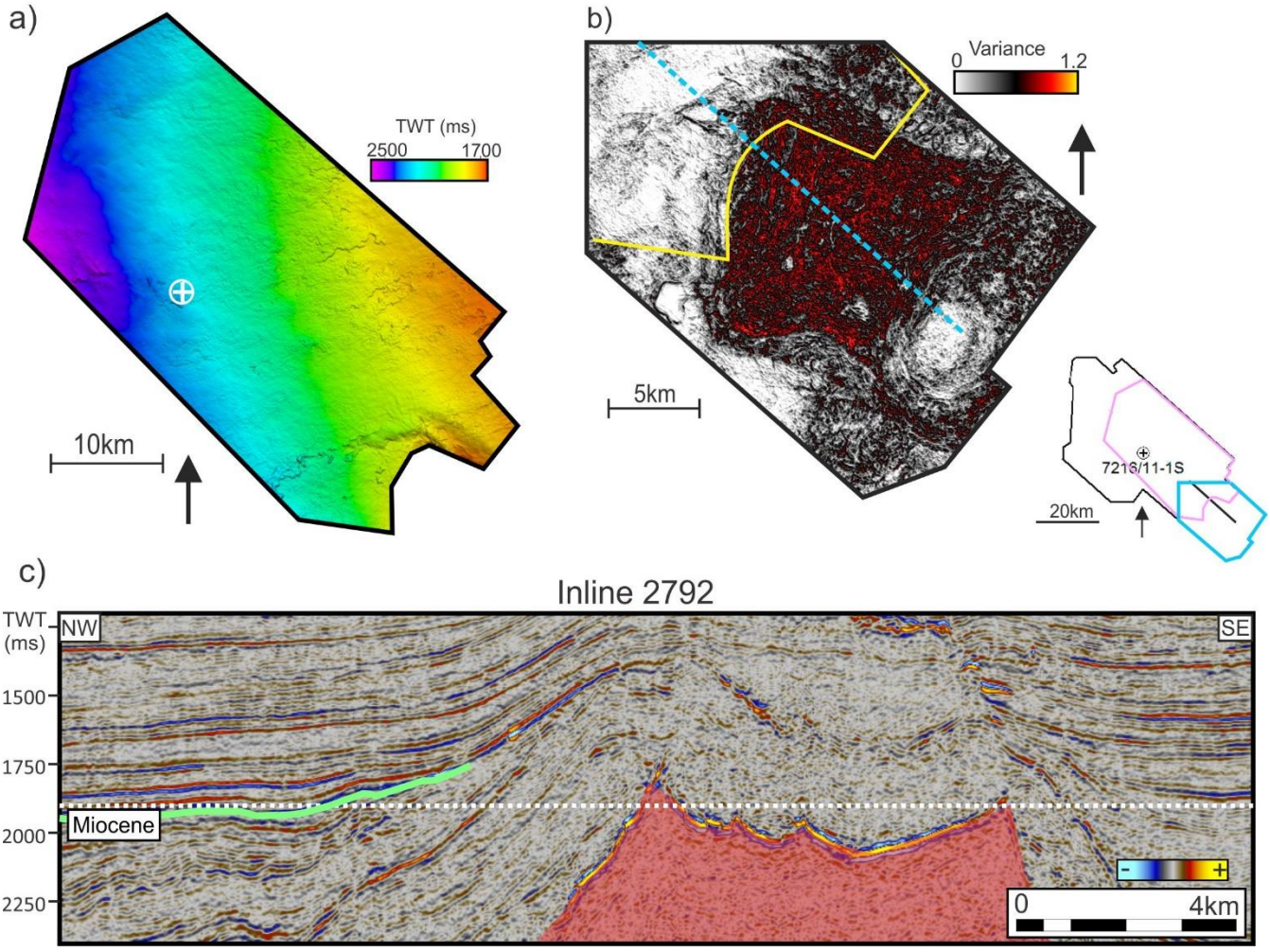

Figure 4.4 a) Time structure map of the Miocene reflector showing how the reflector gently dips towards west b) Variance time slice at 1916ms showing the abrupt change in continuity towards the southeast. The yellow line marks the southeastern extent of the mapped Miocene reflector. The blue dashed lines marks the seismic section in 1.5d. c) Seismic section is showing how the Miocene Reflector disappears as it encounters a big dome structure towards the southeast.

4.2.5 Seafloor reflector

The upper boundary of Unit 3 is represented by the seafloor reflector. Overall the time of the reflector ranges between 400-850ms (twt), but it is mainly situated between 400-550ms (twt). The reflector is continuous, gently dipping towards the northwest and has a strong RC. Towards the northwest there is an abrupt deepening trend from ca. 550 to 850ms (twt) (fig 4.5a). On the surface, there are many repetitive parallel lines with a NW-SE orientation (fig 4.5b). In addition, there are randomly orientated lines and some circular to semi-circular depressions (fig 4.5b). Some of these features are visible in the seismic as smaller depressions (fig 4.5c).

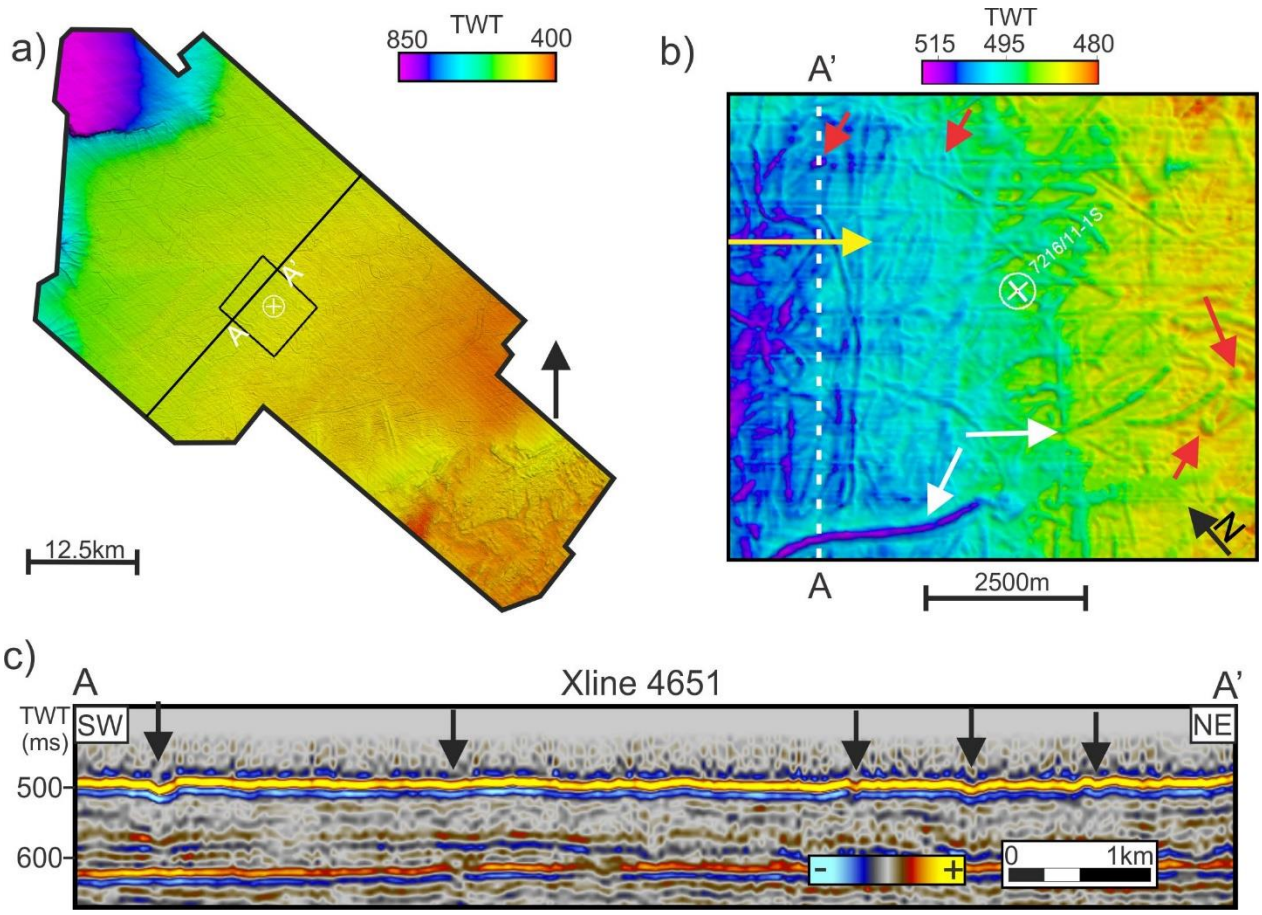

Figure 4.5 a) Time structure map of the seafloor. The black square marks the zoomed in area in 4.5b. b. b) Zoomed in area of the seafloor. The red arrows points at circular to sub circular depressions. The white arrows points at some randomly orientated depressions. The yellow arrow indicates the parallel and repetitive NW-SE lines. c) Part of xline 4651 showing small depressions in the seabed.

4.3 Main units

4.3.1 Unit 1

Unit 1 is the lowermost unit (Fig. 4.1). It is situated within unit 2 and is bounded by reflector 1 and reflector 2. Based on the thickness map in figure 4.6 Unit 1 has a somewhat lens/fan shaped body. The time thickness ranges between 0-100ms (twt) where the average is approximately 80-90ms (twt). Towards the edges, the thickness gradually decreases (fig 4.6). There are no major features within this unit, except for a fault and three sub-parallel reflectors (Fig. 4.2c-e).

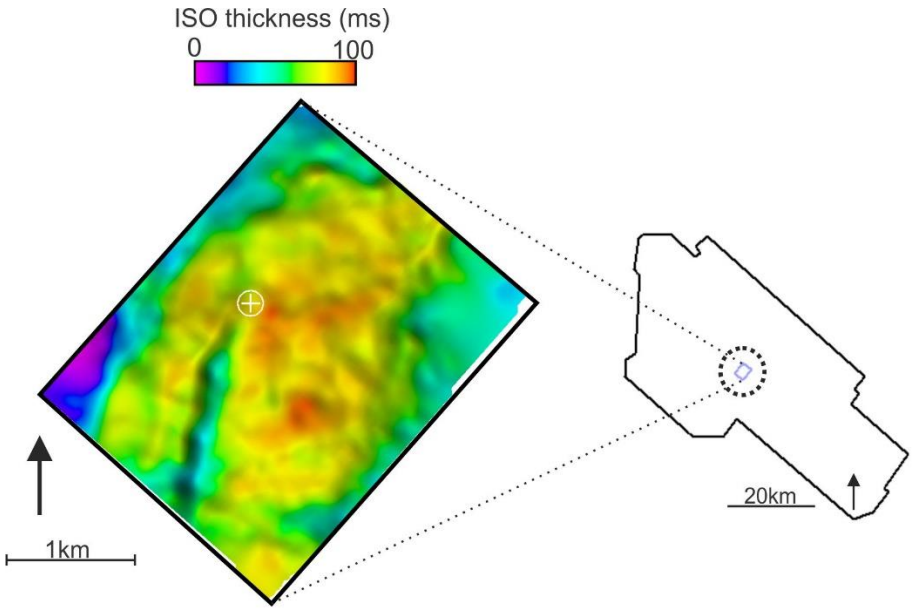

Figure 4.6 Isochron thickness map made between the R2 and R1 reflector.

4.3.2 Unit 2

The time thickness of Unit 2 varies from 500-1500ms (twt) (fig 4.7a). The thinnest parts are located between the uplifted areas and the Miocene reflector, and the thickest parts are located between the dipping areas and the Miocene reflector. Some of the reflectors within the unit are chaotic and discontinuous with a low to intermediate amplitude. Others are stronger and parallel and/or gently dipping. Towards southeast, Unit 2 onlaps a dome structure. Some of the internal seismic within Unit 2 is heavily faulted (fig 4.7a, 4.8a/b). These faults have a smaller offset compared to the ones dividing the early Eocene reflector. None of them affects the Miocene reflector.

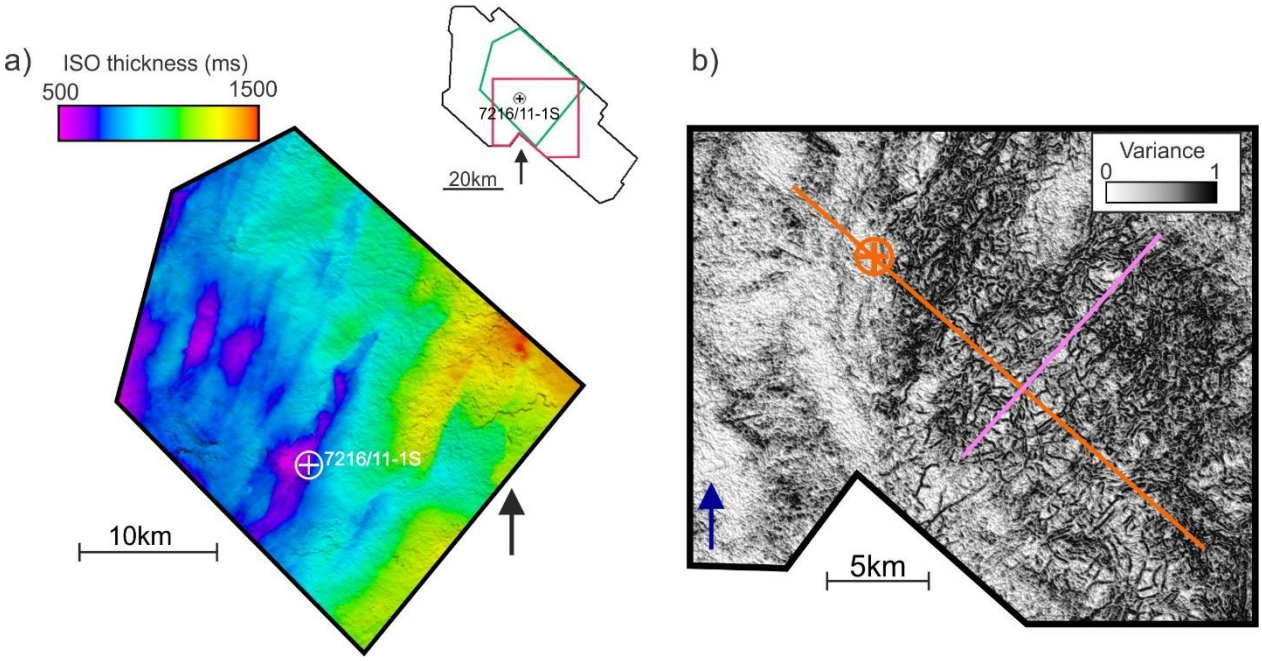

Figure 4.7 a) Thickness map of unit 2. b) Variance time slice at 2364ms showing how the variance of the signal increase towards the southeast. The orange line indicates the position of inline 2940 in figure 4.8a and the pink line indicates the position of xline 5650 in figure 4.8b.

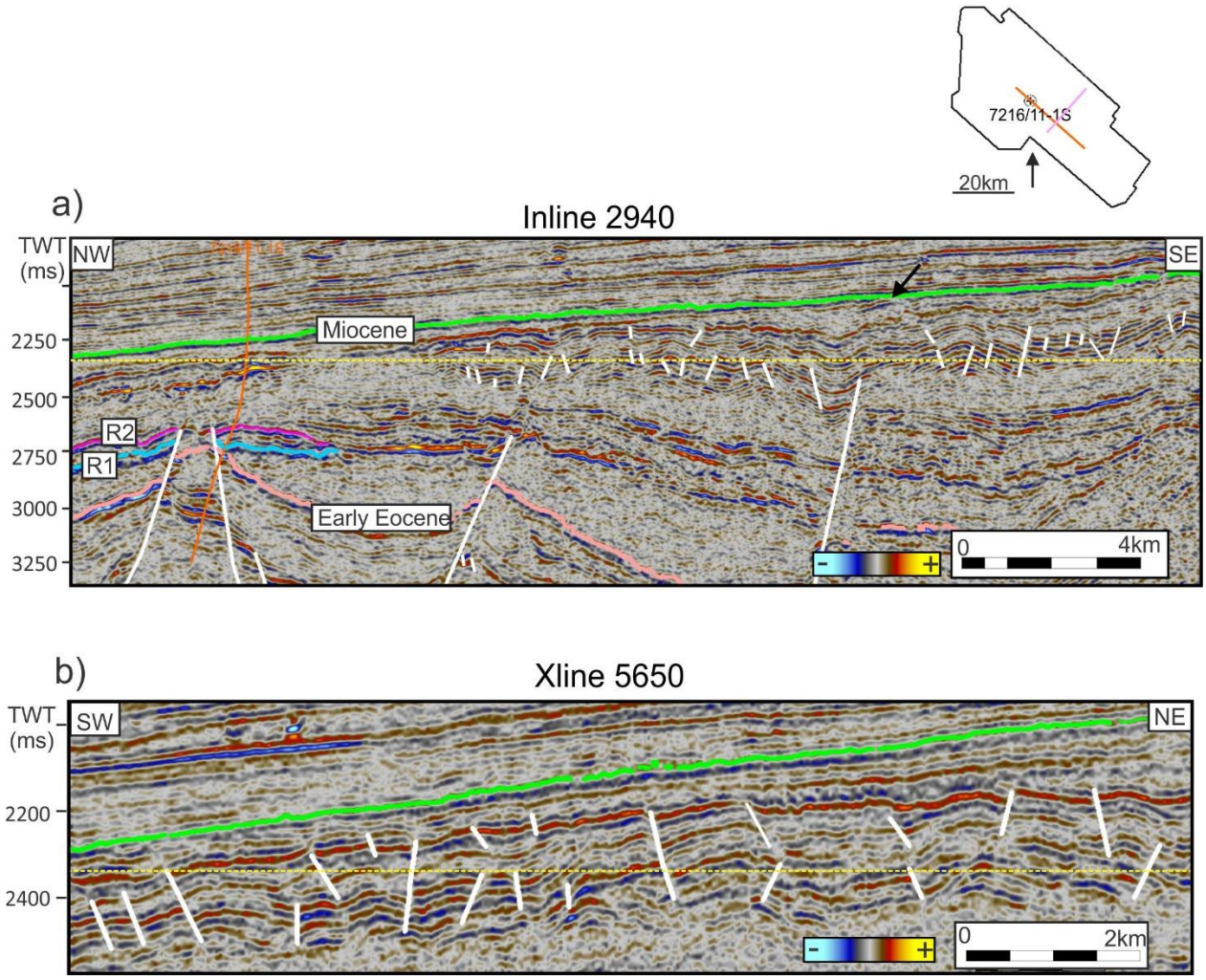

Figure 4.8 a) Parts of Inline 2940 showing how the characteristics in the cap rock varies. The white lines marks faults and the black arrow points at a toplap. The yellow stippled line indicates the position of the variance timeslice in figure 4.7a. b) Part of xline 5650 showing a faulted area of unit 2. The yellow stippled line indicates the position of the variance timeslice in figure 4.7a.

4.3.3 Unit 3

Unit 3 is the uppermost unit. It is bounded by the seafloor and Miocene reflectors. The two-way-time thickness in Unit 3 increases from approximately 1200ms in the east to 2000ms in the west (Fig. 4.9). The unit can be described as a thick section with a highly variable seismic. It contains features such as chaotic, parallel, continuous, discontinuous and dipping reflectors, several high amplitude reflectors and areas where the seismic seems to be disturbed (Fig. 4.10, 4.11). The polarity of some of the reflectors within the unit varies from positive and negative. In general Unit 3 appears to be unaffected by faults except in the areas close to the dome structure in southeast (Fig. 4.11).

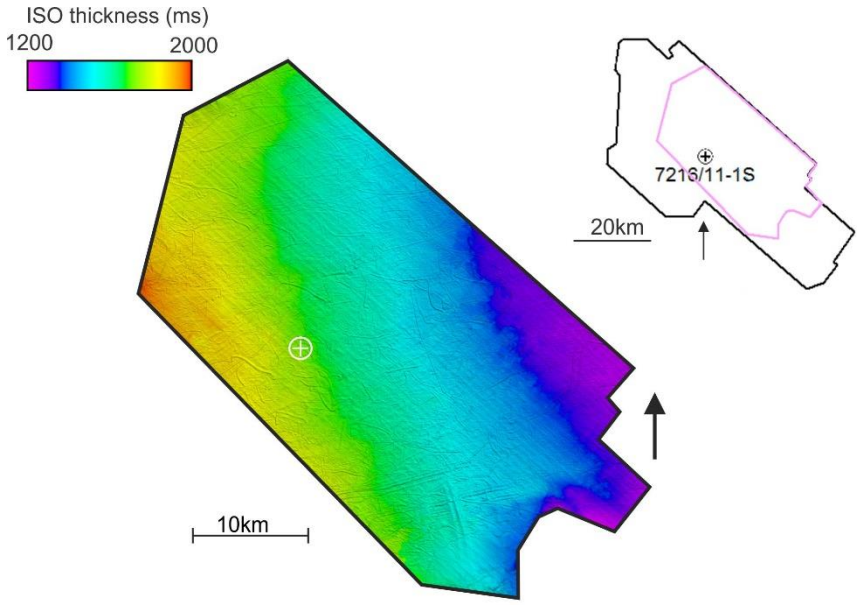

Figure 4.9 Isochron thickness map of the overburden between the Miocene and Seafloor reflector.

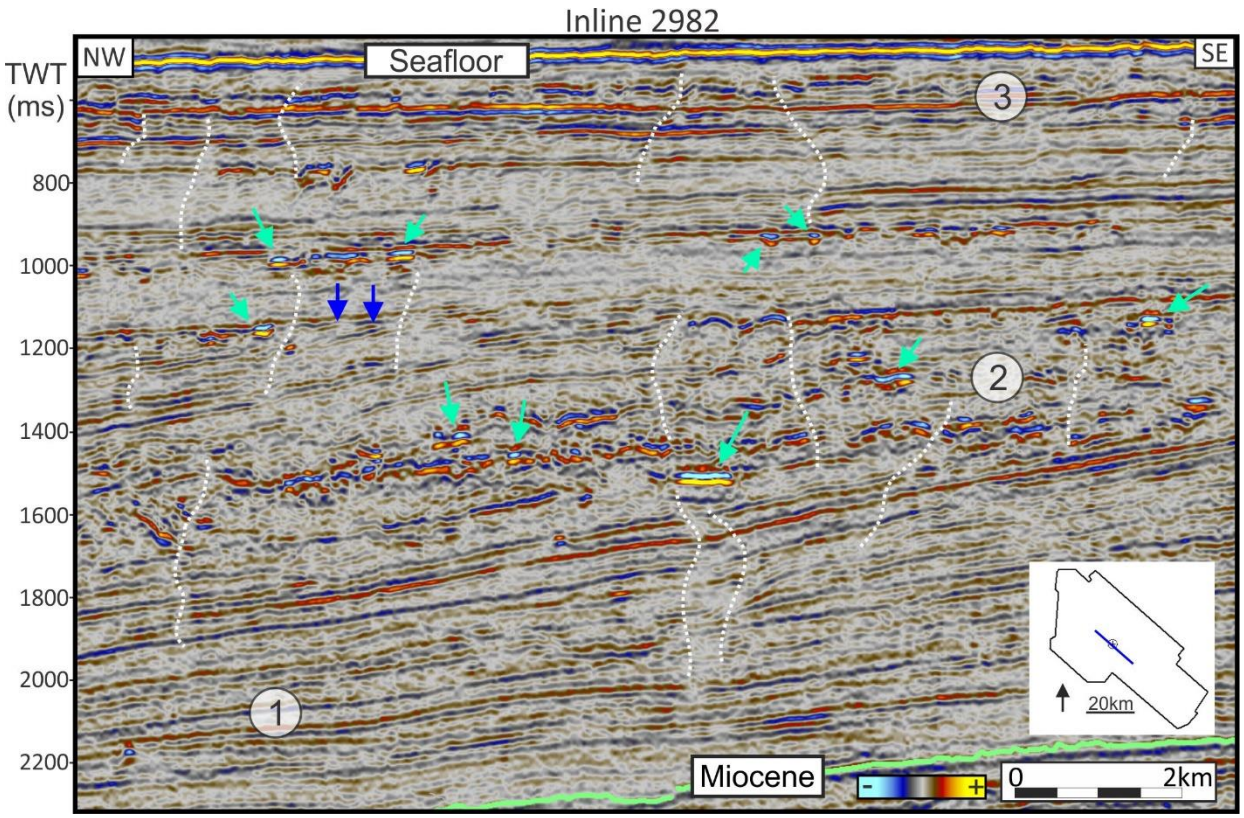

Figure 4.10 Part of Inline 2982. Bright spots are indicate with green arrows. Acoustic pipes are indicated with white stippled lines. Toplaps are indicated with blue arrows. The numbers 1, 2 and 3 indicate areas with dipping reflectors, chaotic reflectors and subparallel reflectors, respectively.

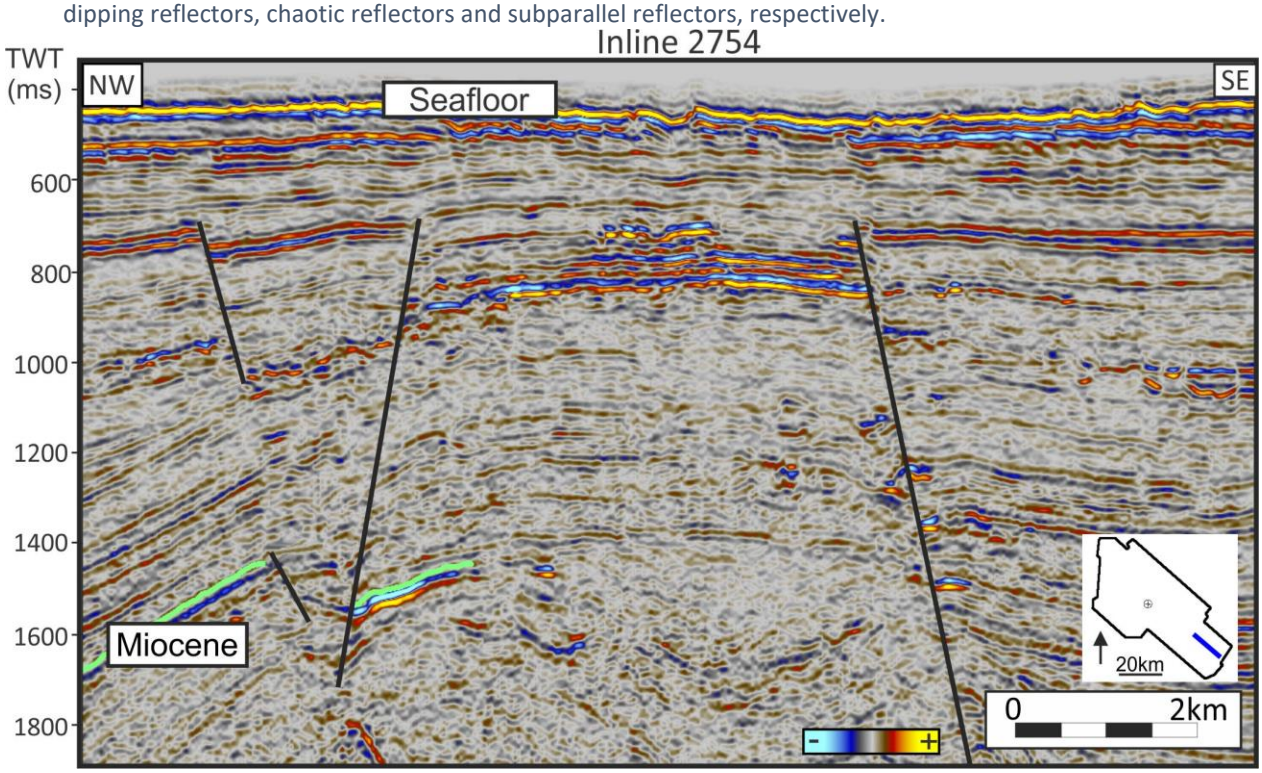

Figure 4.11 Faulted area of the overburden close to the dome structure in the southeast.

4.4 Geological model

To simplify and confine the extent of the geological model the seismic volume is cropped to a smaller area. The cropped volume surrounds well 7216/11-1S and is situated approximately in the middle of the NH 9803 dataset (fig 4.12). Vertically, it extends from 274-3388 ms (twt).

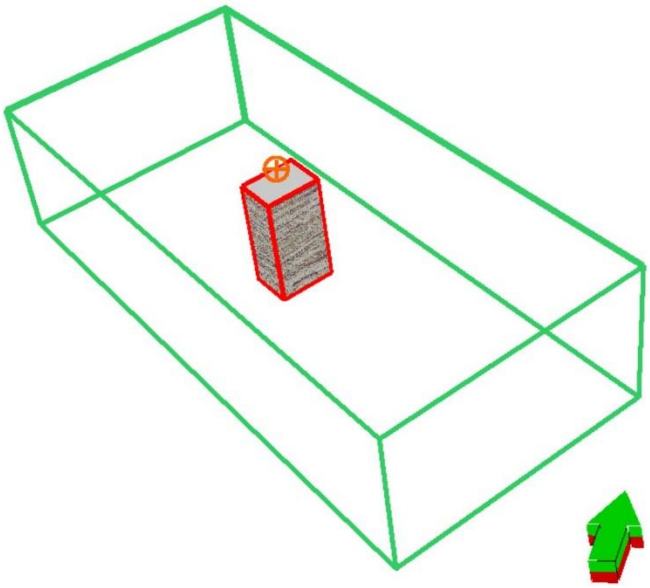

Figure 4.12 Cropped volume (red box) within the dataset (green box).

The geological model in this thesis will try to include some of the main elements with respect to a petroleum system (chapter 1.5).

In the previous chapter, three main units were identified in the NH 9803 dataset. In this model, Unit 1, 2 and 3 are assumed to represent the reservoir, cap rock and overburden, respectively. Even though the reservoir is situated within the cap rock (Fig. 4.1), it is considered as the lowermost unit in the model. The cap rock is also assumed to lie between the R2 reflector and the Miocene.

4.4.1 Petrophysical properties

The previous chapters defined and described the main units and their boundary reflectors. In this chapter, the properties of each unit will be described using information from a number of different logs in well 7216/11-1S (Fig. 4.12). All depths are given in MD, but annotated as m for simplicity.

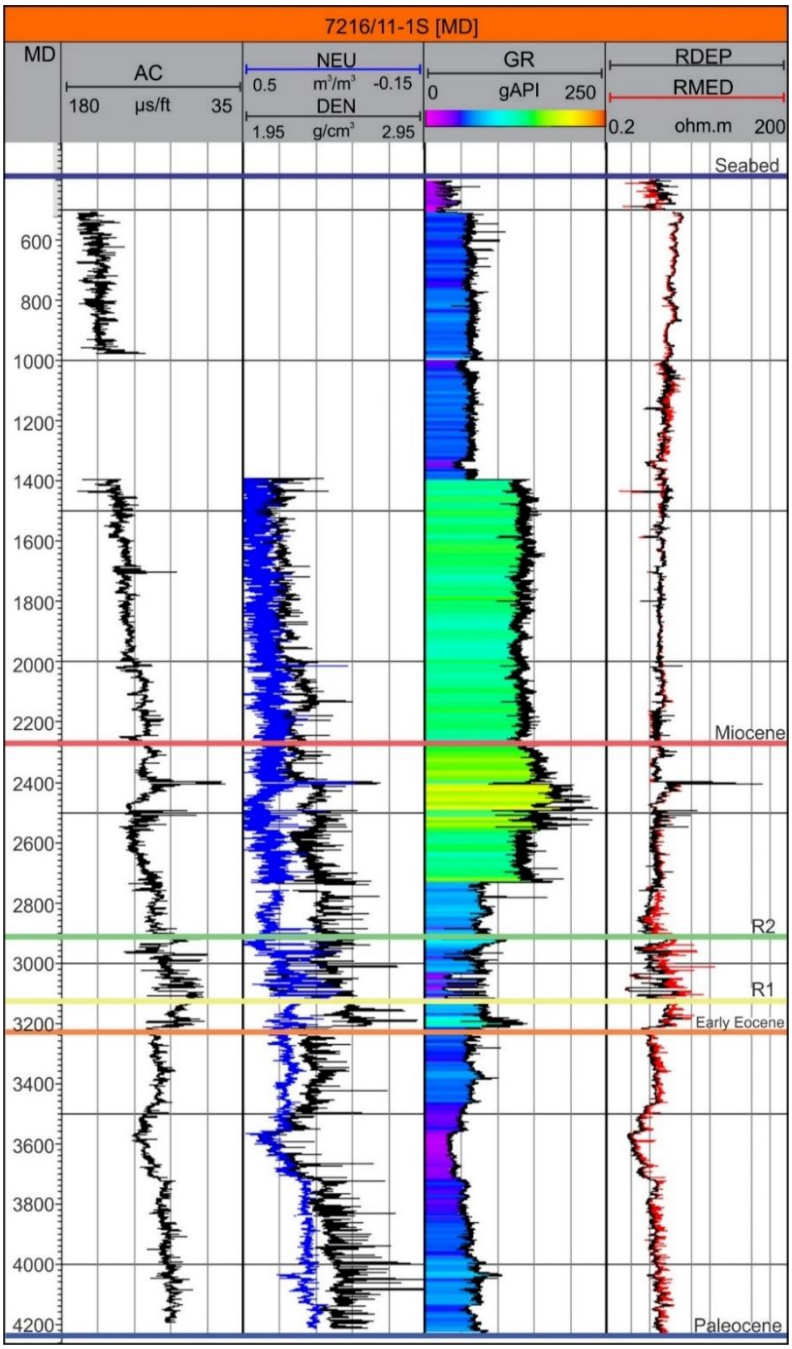

Figure 4.13 Main logs from well 7216/11-1S.

4.4.2 Reservoir

Based on the R1 and R2 well tops in well 7216/11-1s, the gross thickness of the reservoir is 214m. The gamma ray log for the reservoir can be divided into two main intervals; one with very low values and one with low values. Overall, the reservoir unit contains 14 intervals with variable thickness in which the GR value is significantly lower than the rest (fig 4.13). Together, these add up to a total of ca. 52m.

In the thickest very low GR unit, both the deep and medium resistivity values seem to decrease. The resistivity also decreases in some of the thinner units, whereas others have an increase (fig 4.13). In the low value units, no particular trend can be inferred from the resistivity log. In general, the medium resistivity seems to follow the deep resistivity trend, but it has higher values and more fluctuations in the measurements. There are some thin distinct high resistivity layers within the reservoir unit.

There seems to be a trend showing that for all very low GR units, the neutron porosity and bulk density decrease, causing a crossover (neutron and density log cross over and create an overlap between them) (Fig. 4.13). The overall neutron porosity and bulk density is higher in the low GR intervals. There are some layers where the bulk density increases and neutron density decreases. Some of these are located approximately at the same depth as thin high resistivity layers.

There is no clear trend in the sonic log with respect to the different regions. In some intervals, it increases and in other intervals it decreases.

The average values for the reservoir is summarised in table 4.1.

Table 4.1 Average values of the reservoir unit

Thickness (m)	**AC (µs/ft)**	**DEN (g/cm^3)**	**NEU**	**RDEP (ohm.m)**
52 (very low GR)	90.42	2.24	0.27	0.99
162 (low GR)	93.06	2.41	0.37	1.45

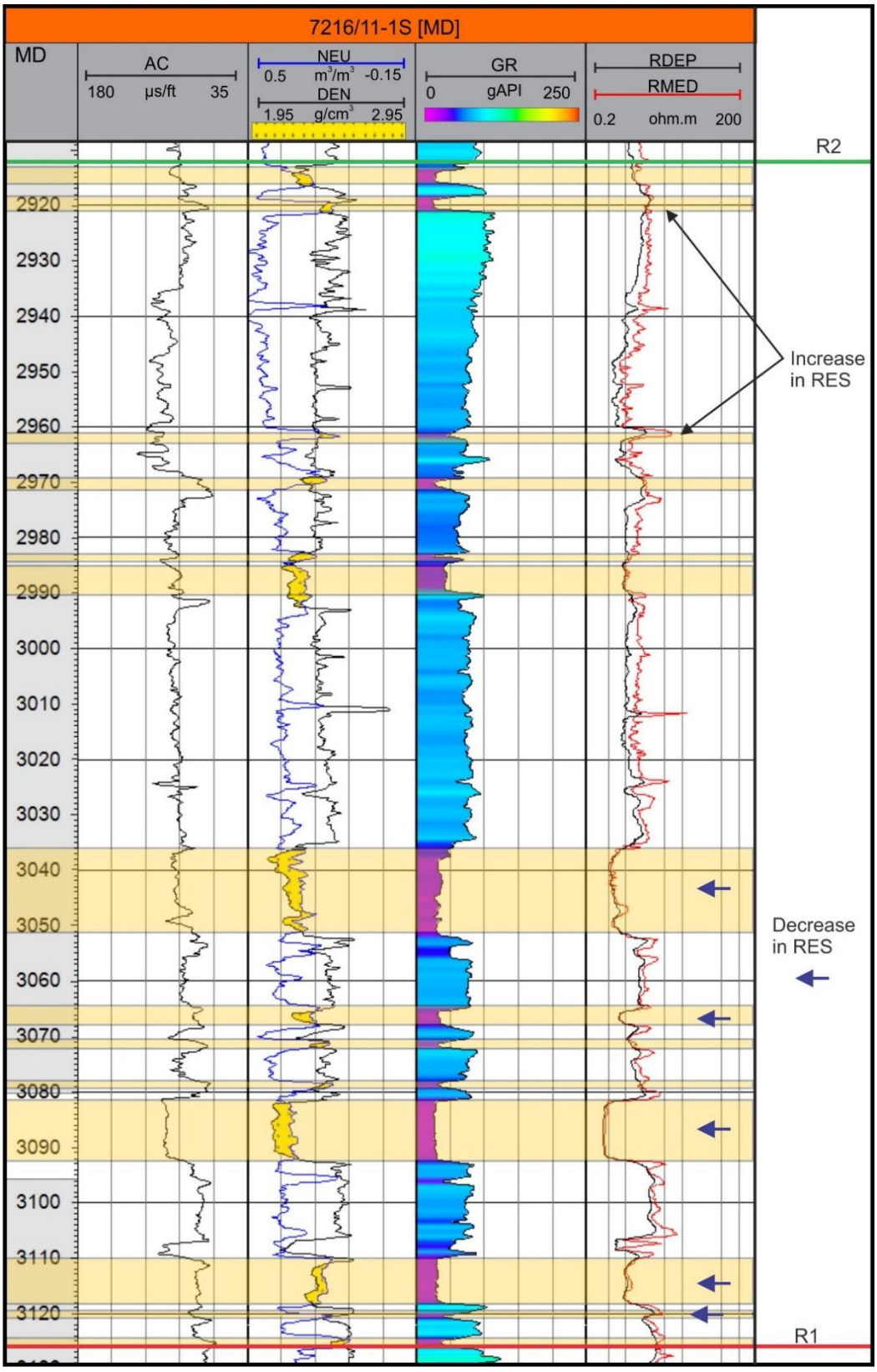

Figure 4.14 Main log responses for the reservoir. The GR can be divided into areas with very low and low values.

Discussion

The 52m with very low GR units represent the net-pay sand, whereas the rest of the GR units represent mainly shale. Compared to the shale, the decrease in resistivity in most of the sandy intervals could indicate an increase in porosity and/or the presence of salt water. If hydrocarbons were present, the resistivity would be expected to increase, as it is harder to transmit an electric current through oil or gas. Some peak resistivities occur in some of the low GR intervals. Overall, the bulk density and velocity is higher in these intervals compared to the rest of the sand, which could imply a less porous rock or another lithology such as a carbonate.

The average NEU value in the sand is quite high and could indicate a porous formation. Since the neutron log measures the amount of hydrogen in a formation, the high neutron porosity values in the shale regions are most likely due to bound water within its crystal lattice as well as free water. This is probably why the average NEU in the shale is higher than the average in the sand.

The crossover between DEN and NEU is often an indication of gas or oil (more crossover with gas). However, there are no significant changes in the velocity. In the same intervals as the crossover, the resistivity decreases, which is the opposite of what the resistivity log would do if it were to be gas in the reservoir. Therefore, these crossovers most likely do not represent gas, but water saturated high porosity sands.

4.4.3 The cap rock

The total thickness of the cap rock is 642 m and it is measured between the R2 and Miocene. Based on the GR log, the cap rock is divided into four units; one unit with low values, two units with intermediate values, and one unit with intermediate values interbedded with higher values (Fig. 4.14). The low GR interval (unit 1) is situated at the bottom and extends from 2912-2734 m . The intermediate GR units are located in the middle (unit 2) and at the top (unit 4), between 2734-2562 m and 2405-2270 m, respectively. The last unit (unit 3) occurs between 2562-2405 m. Within unit 3 there are two thick intervals with a low GR. There is a small interval between 2734-2760 m where there are no measurements for the neutron and density logs.

Except for an increasing trend in parts of unit 3, the resistivity log has no clear trend within the cap rock. However, there are some resistivity peaks. These seems to correlate with the low GR layers in unit 3.

Some trends are observed in the density log. In unit 2 there seems to be a gradual decrease in density. Between the two low GR layers in unit 3, the density increases. The neutron log does not show the same trend, however it decreases when the density increases in unit 3. Four very thin (<1m) crossovers are present throughout the cap rock. In some areas, the density suddenly increases while the neutron porosity decreases. These intervals seem to occur at the same depth as some of the resistivity peaks.

The sonic log has a gradual increase in unit 2. It decreases during the same interval as the density increases in unit 3. There are also some sonic peaks situated at the same depths as the resistivity peaks.

The average values for the cap rock is summarised in table 4.2.

Table 4.2 Average values of the cap rock.

Thickness (m)	AC (µs/ft)	DEN (g/cm^3)	NEU	RDEP (ohm.m)
642	111.63	2.33	0.4	1.42

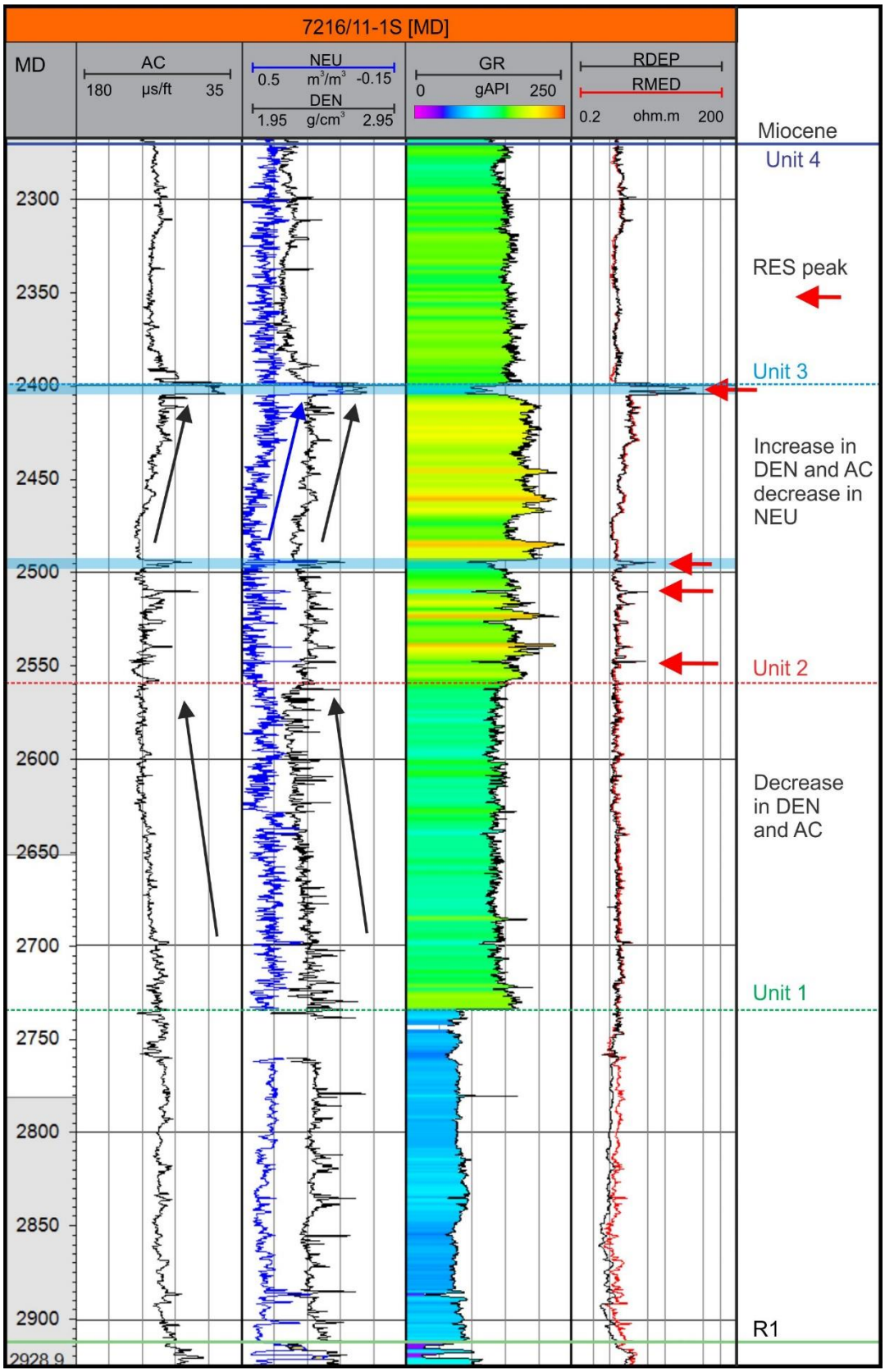

Figure 4.15 Main log responses for the cap rock. The GR can be divided into four units.

Discussion

The cap rock consists mainly of shale interbedded with thin layers of carbonate and sand. It has some peak values in the logs. However, compared to the reservoir unit, the cap rock displays less fluctuations. Overall, it is denser and has a higher neutron porosity and resistivity compared to the net pay sand. Less varying logs most likely indicate a more homogenous lithology. The small intervals with a sudden increase in density, velocity and resistivity probably indicates thinner layers consisting of a different lithology, such as carbonate.

The neutron porosity is higher in the cap rock compared to both the net pay sand and shale in the underlying unit. This could be because it contains more bound and free water.

It should be noticed that the cap rock interval is very thick and the average is taken over a long interval.

4.4.4 The overburden

The overburden has a total thickness of 1884m and is measured between the Miocene well top and seabed. The gamma ray log for this unit can be divided into three regions (fig 4.15). A lower region with intermediate GR (unit 1), a middle region with low GR (unit 2) and a thin upper region with very low GR (unit 3). The lower region extends from 2270-1396 m, the middle from 1396-508 m, and the upper from 508-385 m. All the units contain some lower GR layers within them. The resistivity log is present throughout the whole unit. Between 385-508 and 977-1932 m there is a gap in the sonic log with no measurements. The neutron and density log starts at 1392 m.

In unit 2, there seems to be a slight increase in resistivity. Overall, the resistivity is lower in the topmost unit. There are some thin areas where the resistivity peaks. These peaks seems to be located at the same depths as some of the lower GR layers within the units.

Except for some fluctuations, the density log indicates an overall gradual decrease in density throughout unit 1. The neutron log shows an overall increase in the same area. The DEN and NEU logs cross at several points, but the crossovers are very narrow. Most of them do not correspond to any peak in resistivity except the crossover located at approximately 2012 m. This interval correlate with an increase in resistivity. The average values for the overburden is summarised in table 4.3.

Even though there are some areas with no measurements, the trend in the sonic log is similar to that in the density log, which is an overall gradual increase through the overburden.

Table 4.3 Average values of the overburden.

Thickness (m)	AC (µs/ft)	DEN (g/cm^3)	NEU	RDEP (ohm.m)
1884	129.32	2.18	0.48	1.86

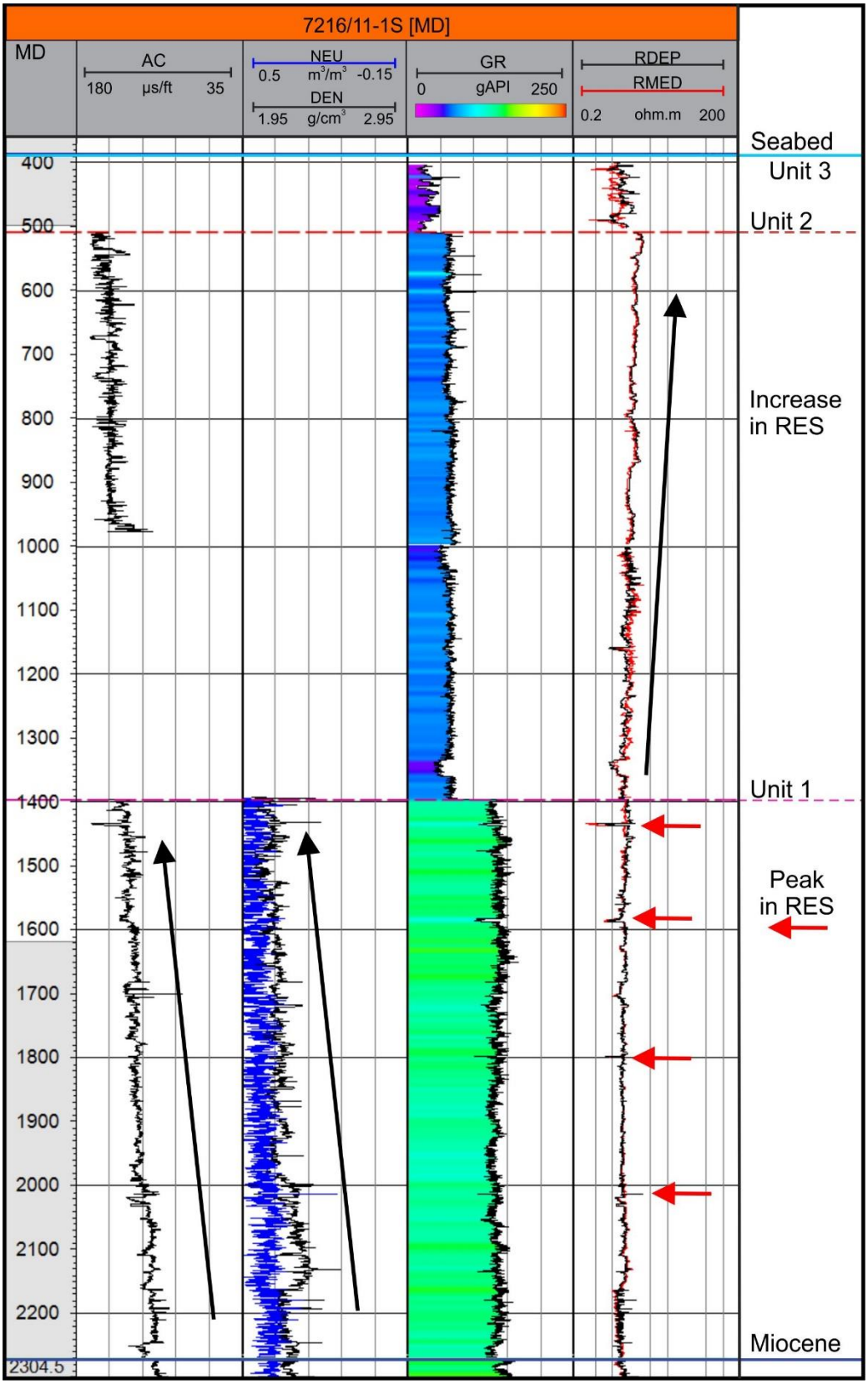

Figure 4.16 The main log responses for the overburden.

Discussion

As with the cap rock, the overburden consist mainly of shale, with some instances of carbonate and/or sand. The logs from the overburden are similar to the cap rock with respect to fluctuations. They do not vary much, except for Unit 3 where there is some variation in the resistivity logs.

The average velocity and density is lower in the overburden compared to the cap rock. This is consistent with the fact that the velocity and density usually increases with depth as rocks gets more compacted and less porous. The neutron porosity decrease with depth in the overburden. This is most likely due to the fact that the sediments get more compacted and less porous, and that water that was initially placed in the pores is pushed out.

There is a decrease in resistivity with depth in the overburden. This is most likely due to the fact that the brine salinity increases with depth (Dickey, 1969).

The bulk density for the measureable part of the overburden is 2.18 g/cm^3. However, the average bulk density for the whole overburden is probably lower, as the density is expected to decrease into unit 2 and 3.

4.5 Summary

To summarise, the geological model consist of three units, the reservoir, cap rock and overburden. Each unit is considered to be homogenous with equal properties throughout the unit. Hence, the properties gained from the logs are extrapolated to apply to the whole unit. By using equation (1.4) and (1.15), and the average values for each unit from tables 4.1, 4.2 and 4.3 the porosity and permeability can be estimated. For this model, only the net pay thickness is considered as the reservoir.

To use equation 1.15, the density of the matrix and fluid has to be assumed. These assumptions are summarised in table 4.4. When assuming that the sandstones in the reservoir consist of only quarts grains, the matrix density is 2.65 g/cm^3, according to Rider & Kennedy (2011). The density of shales vary between 1.8-2.75 g/cm^3 (Rider & Kennedy, 2011). Since the cap rock lies deeper than the overburden it is reasonable to assume that it us more compacted and has a higher density.

The salinity of brines usually increases with depth due to evaporate dissolution and increased rock-water interaction with depth/temperature (Dickey, 1969). Hence, the density increases, and it is likely to assume a small density increase with depth.

To estimate the permeability the irreducible water saturation (S_{wr}) has to be assumed. It usually varies depending on rock type. Conventional reservoirs can have an S_{wr} between 15-20% whereas in shales and siltstones it can be more than 60% (Moore et al., 2016). The assumed S_{wr} for the different units in the model is summarised in table 4.4 along with the calculated porosity and permeability.

Table 4.4 Summary of the different values used to calculate porosity and permeability

Unit	ρ_m	ρ_f	Porosity	Assumed S_{wr}	Permeability
Reservoir	2.65	1.1	26%	20%	571 mD
Cap Rock	2.45	1.075	8%	50%	0.5 mD
Overburden	2.3	1.05	15%	30%	23 mD

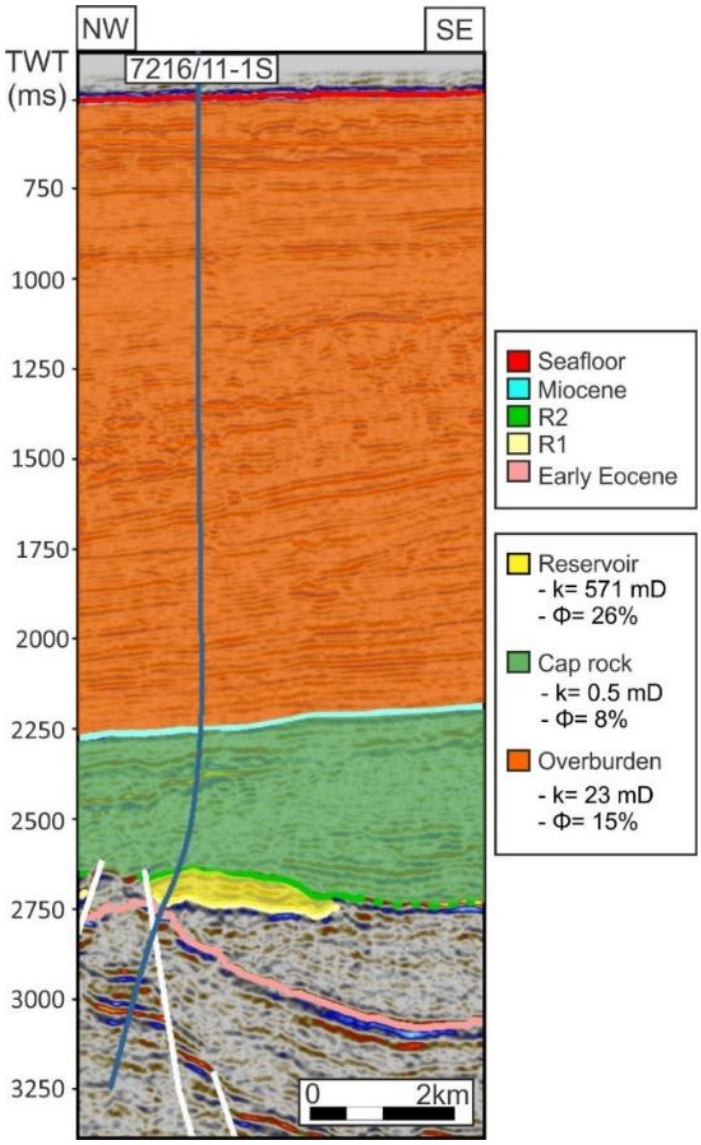

Figure 4.17 Summary of the geological model and its estimated parameters.

5 Mathematical model of two-phase flow

The vertical migration of fluids through a porous medium can be described using a modified Buckley-Leverett model of two-phase flow (Buckley & Leverett, 1942). The original model was introduced by Buckley and Leverett in 1942 and discusses the displacement of oil in a reservoir by injection of either water or gas. Their model is based on certain assumptions such as:

- The flow being horizontal
- Negligible gravitational forces
- Immiscible and incompressible fluids phases.
- Negligible capillary forces

The model in this study is based on some of the original assumptions, such as negligible capillary forces and immiscible and incompressible phases. However, the modified model also includes the gravitational forces and assumes that the flow is vertical. The new assumptions are mainly from Silin et al. (2009b).

This chapter consist of two sections. First the original Buckley-Leverett model and its solution will be introduced. Furthermore, the modified model and a simple walkthrough of its solution is described

A more detailed derivation of some of the equations is given in Appendix A and B.

5.1 Buckley-Leverett model for inclined and horizontal flow

Consider the displacement of oil by an injection of water in a one-dimensional system with cross-sectional area A, length x and angle α (fig 5.1). The fluid flow through the system can be expressed in terms of total flow rate q_t as

$$q_t = q_w + q_o \tag{5.1}$$

Here *q* denotes the volumetric flow rate and the subscripts *t*, *w* and *o* denotes total, water and oil, respectively.

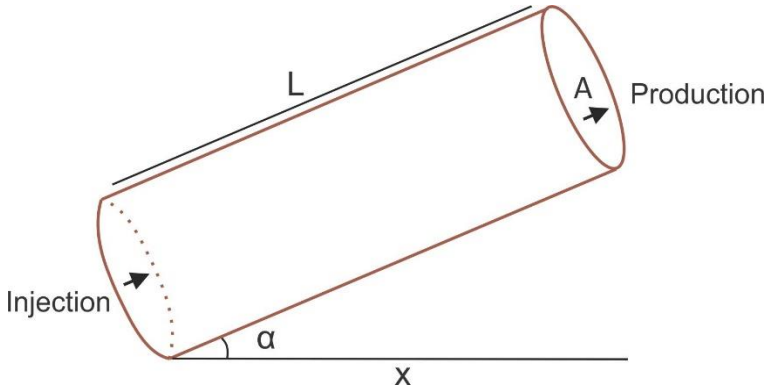

Figure 5.1 Simple sketch of an inclined system.

The volumetric flow rate of each fluid can be expressed with the Darcy equation as (Kleppe, 2017):

$$q_o = -\frac{k_{ro}(S)kA}{\mu_o}\left(\frac{\partial P_o}{\partial x} + \rho_o g \sin(\alpha)\right), \tag{5.2}$$

and

$$q_w = -\frac{k_{rw}(S)kA}{\mu_w}\left(\frac{\partial P_w}{\partial x} + \rho_w g \sin(\alpha)\right). \tag{5.3}$$

Here, the subscripts *o* and *w* correspond to the oil (non-wetting) and water (wetting) fluids, respectively. Furthermore, μ_i denotes their viscosities, ρ_i their densities and P_i their pressures, *i*=*o*,*w*. Furthermore, *k* is the absolute permeability of the medium and k_{ri} is the relative permeability of the fluids. *S*, *g* and *A* denotes the water saturation, gravity acceleration and cross-sectional area, respectively.

The term, $k_{ri}(S)k/\mu_i$, is often referred to as the mobility term because it describes the mobility of the entire system and depend on both fluid and rock properties. A fluid will move easily in a system with high mobility and likewise poorly if the mobility of the system is low. The second term in the equation, ($\nabla P_i + \rho_i g sin\alpha$), describes the driving forces in the system and consists of the difference in phase pressures (∇P_i) and the forces exerted by gravity ($\rho_i g sin\alpha$).

If we insert equation (1.6) for the capillary pressure in equation (5.3) we get

$$q_w = -\frac{k_{rw}(S)kA}{\mu_w}\left(\frac{\partial P_o - P_c)}{\partial x} + \rho_w g \sin(\alpha)\right). \tag{5.4}$$

Rearranging equation (5.2) and (5.4) we get

$$-q_o \frac{\mu_o}{k_{ro}(S)kA} = \frac{\partial P_o}{\partial x} + \rho_o g \sin(\alpha), \tag{5.5}$$

and

$$-q_w \frac{\mu_w}{k_{rw}(S)kA} = \frac{\partial P_o - P_c}{\partial x} + \rho_w g \sin(\alpha). \tag{5.6}$$

Subtracting equation (5.5) from (5.6) we get

$$\frac{1}{kA}\left(q_w \frac{\mu_w}{k_{rw}(S)} - q_o \frac{\mu_o}{k_{ro}(S)}\right) = \frac{\partial P_c}{\partial x} - g(\rho_o - \rho_w)\sin(\alpha). \tag{5.7}$$

The volumetric flow rate of each fluid can be expressed as the product of the total volumetric flow rate and the fluids fractional flow:

$$q_i = q_t f_i \tag{5.8}$$

Here *f* is the fractional flow and *i=o, w*.

The sum of the fractional flow of each phase in a system is always equal to one. In this case

$$f_w + f_o = 1. \tag{5.9}$$

By substituting q_o in equation (5.7) with q_t-q_w, combining it with equation (5.8) and solving with respect to f_w, we get the following expression for the fractional flow of water:

$$f_w = \frac{1 + kA\frac{k_{ro}(S)}{q_t\mu_o}\left(\frac{\partial P_c}{\partial x} - g\left(\rho_o - \rho_w\right)\sin(\alpha)\right)}{\left(1 + \frac{\mu_w k_{ro}(S)}{\mu_o k_{rw}(S)}\right)}. \tag{5.10}$$

The derivation of equation (5.10) is given in Appendix A.

If we assume that the flow is horizontal (α=0) and neglect the capillary pressure, equation (5.10) reduces to

$$f_w = \frac{1}{1 + \frac{k_{ro}(S)\mu_w}{k_{rw}(S)\mu_o}}. \tag{5.11}$$

Figure 5.2 is made with the matlab code provided in appendix D and shows a plot of the fractional flow function in equation (5.11) and its derivative df/dS. The fractional flow of a fluid will increase with its saturation in the medium (Buckley & Leverett, 1942). This gives rise to the S-shaped f_w curve in figure 5.2.

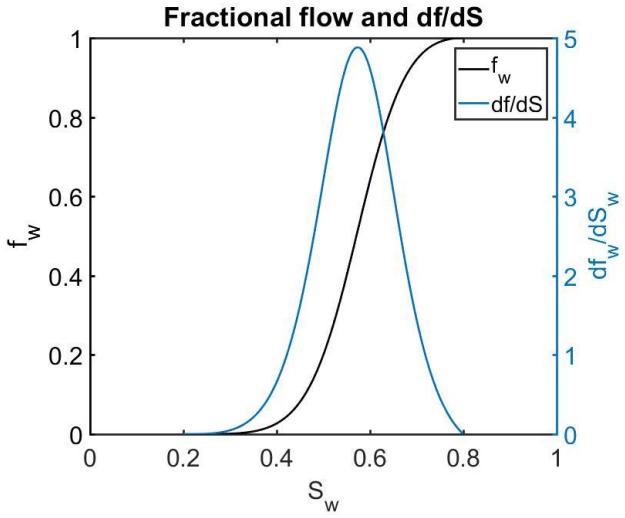

Figure 5.2 Fractional flow curve and its derivative.

The change in water flow rate across a system with length Δx during a time Δt can be found by performing a mass balance. According to Kleppe (2017) the mass balance is given by

$$[(q_w\rho_w)_x - (q_w\rho_w)_{x+\Delta x}]\Delta t = A\Delta x\phi[(S\rho_w)_{t+\Delta t} - (S\rho_w)_t]. \quad (5.12)$$

When Δx→ 0 and Δt →0 equation (5.12) reduces to (Kleppe, 2017)

$$-\frac{\partial}{\partial x}(q_w\rho_w) = A\phi\frac{\partial}{\partial t}(S\rho_w). \quad (5.13)$$

If we assume that the fluids are incompressible the density changes over time and distance can be neglected (ρ_w=constant). Combining this assumption with equation (5.8) and (5.13) we get the Buckley-Leverett (1942) equation expressed as

$$-\frac{\partial f_w(S)}{\partial x} = \frac{A\phi}{q_t}\frac{\partial S}{\partial t}. \quad (5.14)$$

5.1.1 Solution

Equation (5.14) can be solved analytically under certain assumptions, or numerically for a wider range of conditions. In this thesis, the focus will be on analytical solutions. There will also be a description of a graphical solution introduced by Welge (1952). Examples of numerical solutions and comparison between analytical and numerical solutions are given by e.g., Rosland (2013) and Jaoua (2017).

The standard Buckley-Leverett solution involves the study of the fractional flow theory. It is more convenient to use dimensionless variables when solving the Buckley-Leverett equation (Hirasaki, 2009). The dimensionless position x_D is defined with respect to the system length (L) as

$$x_D = \frac{x}{L}. \quad (5.15)$$

The dimensionless time t_D is defined as

$$t_D = \frac{q_t}{AL\phi}t. \quad (5.16)$$

Using equation (5.15) and (5.16) the dimensionless Buckley-Leverett equation can be expressed as

$$-\frac{\partial f_w}{\partial x_D} = \frac{\partial S}{\partial t_D}, \tag{5.17}$$

The fractional flow function is a function of the water saturation only. The water saturation is a function of distance and time, and the saturation changes can be expressed as

$$dS = \frac{\partial S}{\partial x_D} dx_D + \frac{\partial S}{\partial t_D} dt_D, \tag{5.18}$$

where $t_D \geq 0$.

During the displacement process, the fluid front is assumed to have a constant saturation (Buckley & Leverett, 1942), thus

$$0 = \frac{\partial S}{\partial x_D} dx_D + \frac{\partial S}{\partial t_D} dt_D. \tag{5.19}$$

Substituting into equation (5.17), we get

$$\frac{dx_D}{dt_D} = \frac{df_w}{dS}. \tag{5.20}$$

Equation (5.20) describes the velocity that the fluid front with a certain value of S propagates with. It states that the velocity of a plane with a specific saturation at the fluid front is proportional to the derivative of the fractional flow curve. It also represents the slope of a line of constant saturation, where dS=0, in the (x,t) plane (Bedrikovetsky, 2013). In figure 5.3 each line corresponds to a constant saturation. The initial and boundary condition are assumed to be constant. Changes start at (x_D, t_D)=(0,0) and propagate in lines of constant saturation. Changes in saturation with time and distance are known as saturation waves (Lake, 1989).

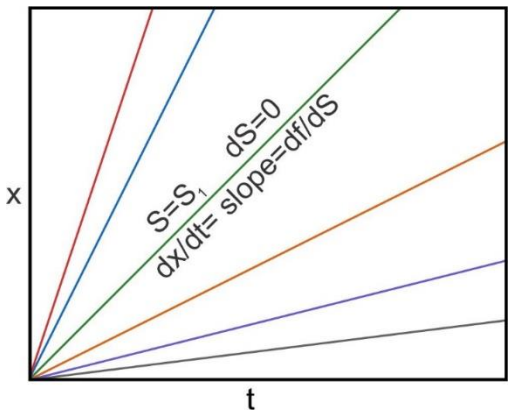

Figure 5.3 Schematic illustration of trajectories with a constant saturation in the (x,t) plane. The slope of the lines gives the velocity at that saturation.

We distinguish between three main types of waves:

1. Rarefaction wave

A rarefaction wave (fig 5.4) is a wave that becomes more diffusive upon propagation and where the slope, $\frac{dS}{dx}$, decreases over time (Lake, 1989).

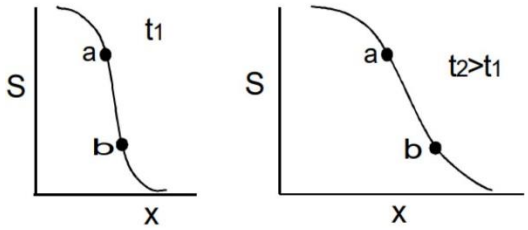

Figure 5.4 Spreading/diffusive wave. From Hirasaki (2009).

2. Indifferent wave

An indifferent wave (fig 5.5) maintains the same relative position wile propagating and $\frac{dS}{dx}$ is constant (Lake, 1989).

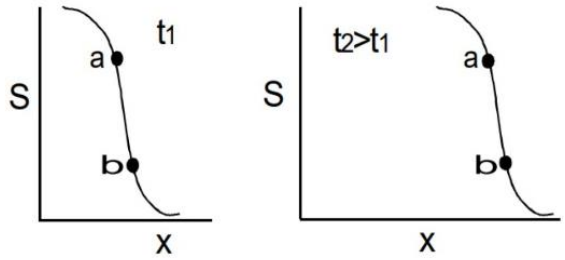

Figure 5.5 Indifferent wave. From Hirasaki (2009).

3. Sharpening wave

A sharpening wave (fig 5.6) is a wave that becomes less diffusive upon propagation and were $\frac{dS}{dx}$ increases with time (Lake, 1989). A shock wave is a discontinuity that arises from a sharpening wave (fig 5.6).

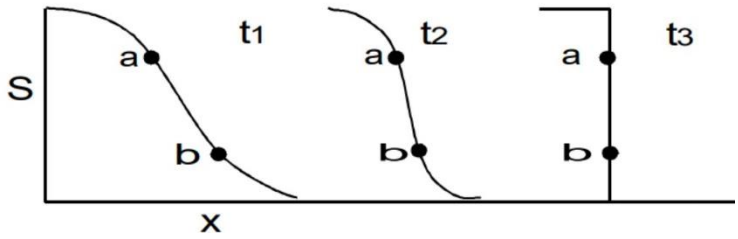

Figure 5.6 Sharpening wave turning into a shock wave. From Hirasaki (2009).

Integrating eqs. (5.20) in time

$$\int \frac{dx_D}{dt_D} dt = \int \frac{\partial f_w}{\partial S} dt_D, \tag{5.21}$$

gives an expression known as the frontal advance equation which gives the position of the fluid front

$$(x_D)_f = t_D (\frac{\partial f_w}{\partial S})_f. \tag{5.22}$$

Figure 5.7 shows the water saturation as a function of x_D from t=0.05 to t=0.4 with a time step of 0.05. The plot of saturations vs distance at a specific time is known as a saturation profile (Lake, 1989).

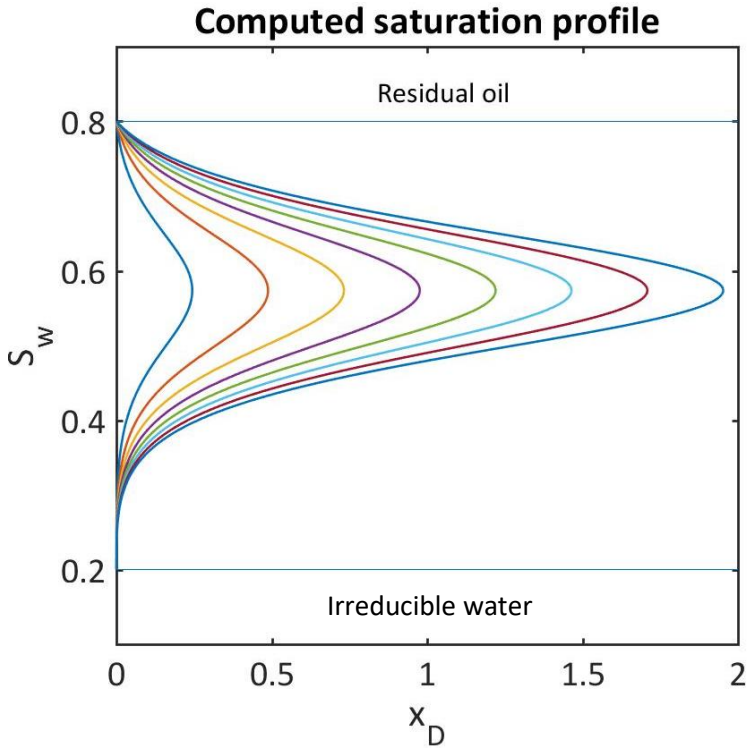

Figure 5.7 Typical saturation profile.

The saturation profile has a maximum point. This indicates that at a certain distance there are two saturations present. This is physically not possible. The problem is solved by assuming that the saturation has a discontinuity (shock front) at the fluid front and by balancing of the areas ahead (A_1) and below (A_2) the curve (Fig.5.8a) (Buckley & Leverett, 1942).

It is possible to find the shock front saturation graphically. Welge (1952) developed a graphical solution for determining the shock front saturation by using the average water saturation behind the front. Figure 5.8b show an illustration of the concept behind Welge's method. The graphic solution is to draw the tangent line to the fractional flow curve, drawn from the irreducible water saturation (S_{wr}). This line must have a point of tangency which represents the saturation and fractional flow at the fluid front. The extrapolated tangent to the point where f_w=1 gives the average water saturation behind the front.

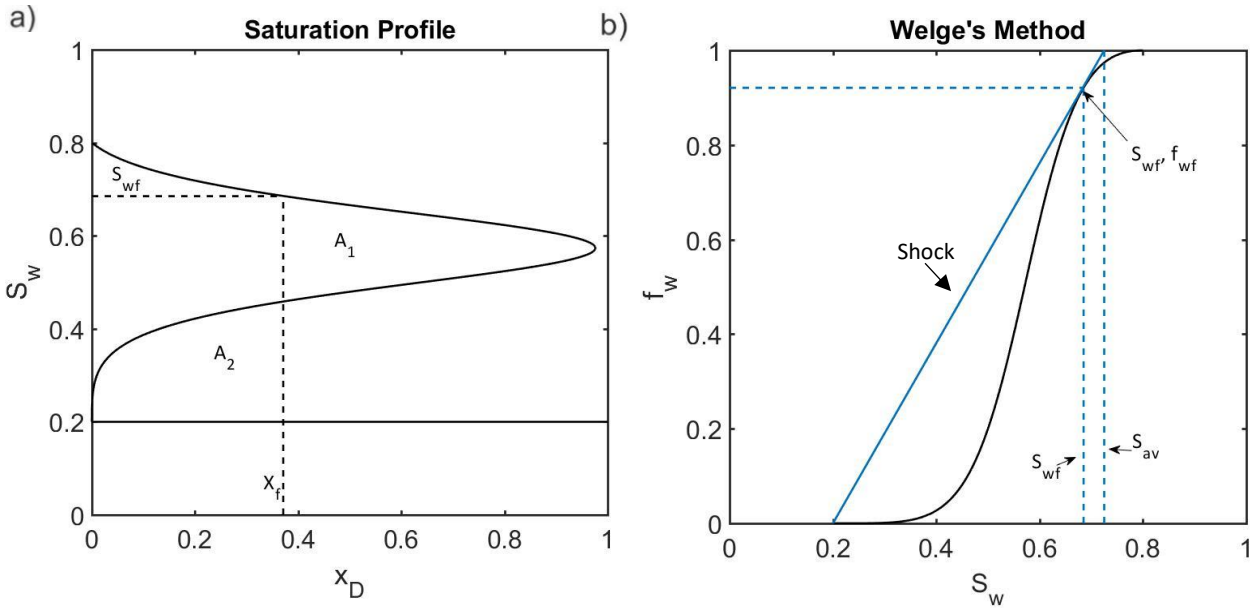

Figure 5.8 a) Illustration of how to balance of the areas in the saturation profile b) Graphical determination of the shock front saturation using the tangent to the fractional flow curve from the irreducible water saturation (S_{wr}) to S_{av}.

The velocity at the fluid front saturation can according to Welge (1952) be expressed as

$$\left(\frac{\partial f}{\partial S}\right)_{S_{wf}} = \frac{1}{S_{av} - S_{wr}}. \tag{5.23}$$

which is equal to the slope of the tangent line in figure 5.8b. Here S_{av} denotes the average water.

Figure 5.9 shows the final saturation profile.

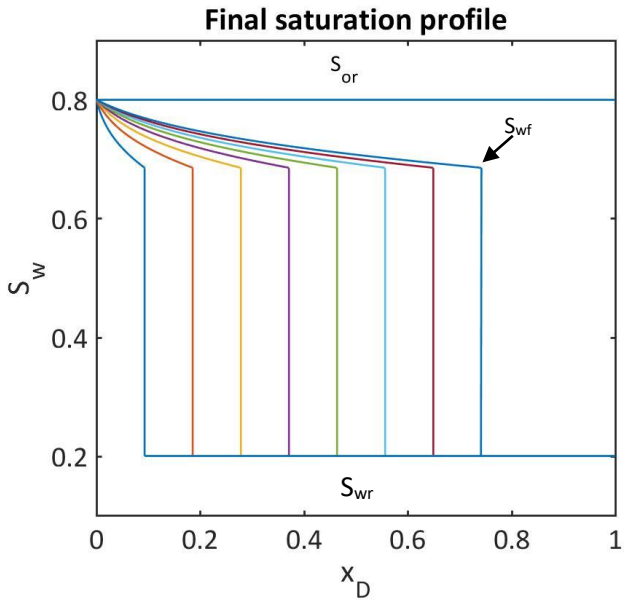

Figure 5.9 Final saturation profile.

5.2 Mathematical model for vertical flow

The Darcy velocities of gas and water can through Darcy's law for two phase flow be expressed as,

$$\boldsymbol{u}_g = \frac{k_{rg}(S)k}{\mu_g}\left(-\nabla P_g + \rho_g g sin(\alpha)\right), \tag{5.24}$$

and

$$\boldsymbol{u}_w = \frac{k_{rw}(S)k}{\mu_w}\left(-\nabla P_w + \rho_w g sin(\alpha)\right). \tag{5.25}$$

Here, the subscripts *g* and *w* correspond, to the gas (non-wetting) and water (wetting) phase, respectively. Furthermore, $\boldsymbol{u}_i$ are the Darcy velocities of the fluids. In the Buckley-Leverett model we assumed that the gravity forces were negligible. In this model equation (5.24) and (5.25) will take into account the gravity. In a vertical system, α=90. Since sin (90)= 1, the gravity term reduces to $\rho_i g$.

Figure 5.10 shows the configuration of the system. The vertical coordinate, z, is directed upwards. A positive Darcy velocity therefore implies upwards migration and $\boldsymbol{g} = -\hat{z}g$.

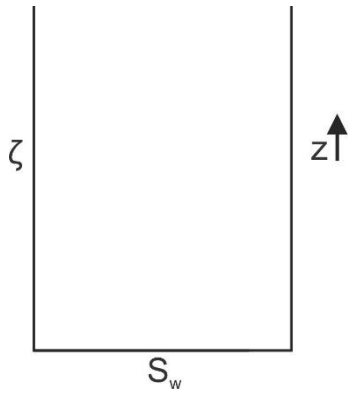

Figure 5.10 Schematic configuration of the system.

If we insert equation (1.6) for capillary pressure in equation (5.24), ∇P_g can be eliminated from the equation. Equation (5.24) then becomes

$$u_{g=}\frac{k_{rg}(S)k}{\mu_g}(-\nabla P_c(S)-\nabla P_w+\rho_g g) \tag{5.26}$$

The mass balance of each fluid can according to Silin et al. (2009a) be written as

$$\frac{\partial(\rho_g(1-S)\phi)}{\partial t}+\nabla\cdot\left(\rho_g\boldsymbol{u}_g\right)=0, \tag{5.27}$$

and

$$\frac{\partial(\rho_w S\phi)}{\partial t}+\nabla\cdot(\rho_w\boldsymbol{u}_w)=0, \tag{5.28}$$

where ϕ is the porosity of the medium.

If we assume that the porosity is constant and we neglect the compressibility of the fluids and the rock, we can neglect the density changes with depth and time and equation (5.27) and (5.28) becomes

$$\frac{\partial((1-S)\phi)}{\partial t}+\nabla\cdot\left(\boldsymbol{u}_g\right)=0 \tag{5.29}$$

and

$$\frac{\partial(S\phi)}{\partial t}+\nabla\cdot(\boldsymbol{u}_w)=0 \tag{5.30}$$

Summation of equation (5.29) and (5.30) yields

$$\nabla\cdot\left(\boldsymbol{u}_g+\boldsymbol{u}_w\right)=0. \tag{5.31}$$

By assuming a vertical flow, the lateral flow components ($\frac{\partial}{\partial \mathrm{x}}$ and $\frac{\partial}{\partial \mathrm{y}}$) can be neglected. With this assumption equation (5.31) simplifies to

$$\boldsymbol{u}_g+\boldsymbol{u}_w=0, \tag{5.32}$$

and the flow is countercurrent. This means that the volume of the gas migrating upwards is replaced by an equal amount of water flowing downwards (Silin et al., 2006).

Combining equations (5.25), (5.26), and (5.32) and solving with respect to $\frac{\partial \mathrm{P_w}}{\partial \mathrm{z}}$, we get

$$\frac{\partial P_w}{\partial z} = -\frac{1}{\frac{k_{rg}(S)}{\mu_g} + \frac{k_{rw}(S)}{\mu_w}} \left(\frac{k_{rg}(S)}{\mu_g} \frac{\partial}{\partial z} P_c(S) + \frac{k_{rg}(S)}{\mu_g} \rho_g g + \frac{k_{rw}(S)}{\mu_w} \rho_w g \right). \quad (5.33)$$

Equation (5.33) can be rearranged and simplified to

$$\frac{\partial P_w}{\partial z} = -\frac{\frac{k_{rg}(S)}{\mu_g}}{\frac{k_{rg}(S)}{\mu_g} + \frac{k_{rw}(S)}{\mu_w}} \left(\frac{\partial}{\partial z} P_c(S) - \left(\rho_w - \rho_g\right) g \right) - \rho_w g. \quad (5.34)$$

Combining equations (5.25) and (5.34), the Darcy velocity of water can be expressed as

$$\boldsymbol{u}_w = \frac{k}{\mu_w} f_w(S) \left(\frac{\partial}{\partial z} P_c(S) - \left(\rho_w - \rho_g\right) g \right), \quad (5.35)$$

where $f_w(S)$ is the fractional flow function given by

$$f_w(S) = \frac{k_{rw}(S)}{\frac{k_{rw}(S)}{k_{rg}(S)} \frac{\mu_g}{\mu_w} + 1}. \quad (5.36)$$

From equation (5.30) and (5.35) we get that

$$\frac{\partial (S\phi)}{\partial t} = -\frac{\partial}{\partial z} \boldsymbol{u}_w = -\frac{\partial}{\partial z} \left(\frac{k}{\mu_w} f_w(S) \left(\frac{\partial}{\partial z} P_c(S) - \left(\rho_w - \rho_g\right) g \right) \right). \quad (5.37)$$

To express all equations in a dimensionless form, we introduce a dimensionless time, τ, and a dimensionless spatial coordinate, ζ, where

$$\zeta = \frac{z}{H} \quad (5.38)$$

and

$$\tau = \frac{k\left(\rho_w - \rho_g\right) g}{\mu_w H} t. \quad (5.39)$$

Here, H denotes the thickness of the reservoir in meters, and t is time in seconds. If we use the reservoir thickness in the geological model as an example of H, one ζ unit equals to 52 m.

A dimensionless Darcy Velocity W_w can through equations (5.38) and (5.39) be expressed as

$$W_w = \frac{\mu_w}{k(\rho_w - \rho_g)g} u_w. \tag{5.40}$$

Combining equations (5.35) and (5.40), we get that

$$W_w = f_w(S)\left(\frac{1}{(\rho_w - \rho_g)g}\frac{\partial}{\partial z}P_c(S) - 1\right) \tag{5.41}$$

The capillary pressure can according to Leverett et al. (1942) be expressed as

$$P_c(S) = \sigma\sqrt{\frac{\phi}{k}}J(S), \tag{5.42}$$

where σ is the interfacial tension and *J(S)* is the dimensionless Leverett J-function.

Inserting equation (5.42) in (5.41) we get that

$$W_w = f_w(S)\left(\gamma J'(S)\frac{\partial S}{\partial \zeta} - 1\right), \tag{5.43}$$

where

$$\gamma = \frac{\sigma}{(\rho_{w-}\rho_g)gH}\sqrt{\frac{\phi}{k}}, \tag{5.44}$$

is a dimensionless factor that describes the ratio between the capillary and buoyancy forces. A low value is associated with permeable layers whereas a high value is associated with low permeable layers (Silin et al., 2009a).

Table 5.1 Formation parameters

	ϕ (%)	**k (mD)**
Reservoir	26	571
Cap rock	8	0.5

Table 5.2 Fluid parameters

σ (N/m)	**ρ_w (kg/m^3)**	**ρ_g (kg/m^3)**	**μ_w (Pa·s)**
0.03	1000	561	$5\cdot10^{-4}$

Using the formation and fluid parameters in tables 5.1 and 5.2, γ can be calculated. For the calculations, the permeability is converted to m^2. For a gas flowing through a 1m thick permeable reservoir the order of $\gamma \simeq 1$, whereas for a 1m thick cap rock the order of $\gamma \simeq 3$. Using the same parameters in eqs. (5.39) a unit interval for the dimensionless time τ corresponds to

approximately 2 days in the reservoir, whereas in the cap rock the respective time scale corresponds to 27231 days. The fluid parameters are taken from (Silin et al., 2009a).

The dimensionless form of equation (5.37) is

$$\frac{\partial(S\phi)}{\partial\tau} = -\frac{\partial}{\partial\zeta}W_w = \frac{\partial}{\partial\zeta}\left(f_w(S)\left(-\gamma J'(S)\frac{\partial S}{\partial\zeta}+1\right)\right). \tag{5.45}$$

In front of a migrating fluid, the variation in saturation is very low and there is a small saturation gradient. This can be expressed as

$$\left|\gamma J'(S)\frac{\partial S}{\partial z}\right| \ll 1. \tag{5.46}$$

According to assumption (5.46) the capillary pressure can be neglected (Silin et al., 2006), which leads to the Buckley-Leverett approximation.

Using assumption (5.46) in eqs. (5.43) and (5.45) they reduce to

$$W_w = -f_w(S) \tag{5.47}$$

and

$$\phi\frac{\partial S}{\partial\tau} = \frac{\partial}{\partial\zeta}f_w(S). \tag{5.48}$$

Equation (5.48) is a modified version of the Buckley-Leverett equation introduced in the previous chapter.

5.2.1 Exact solutions

A simple walkthrough of the solution will be provided in this chapter. For a more detailed explanation of the Buckley-Leverett problem with an account for gravity, see e.g. Wangen (1993), Kaasschieter (1999) and Hayek et al. (2009)

Figure 5.11 shows the plot of the fractional flow function in equation (5.36) . The shape of this curve is different compared to the S-shaped fractional flow function in figure 5.2. This difference is due to the fact that fractional flow in the original Buckley-Leverett model is injection driven and the one in figure 5.11 is buoyancy driven (Wangen, 1993; Hayek et al., 2009).

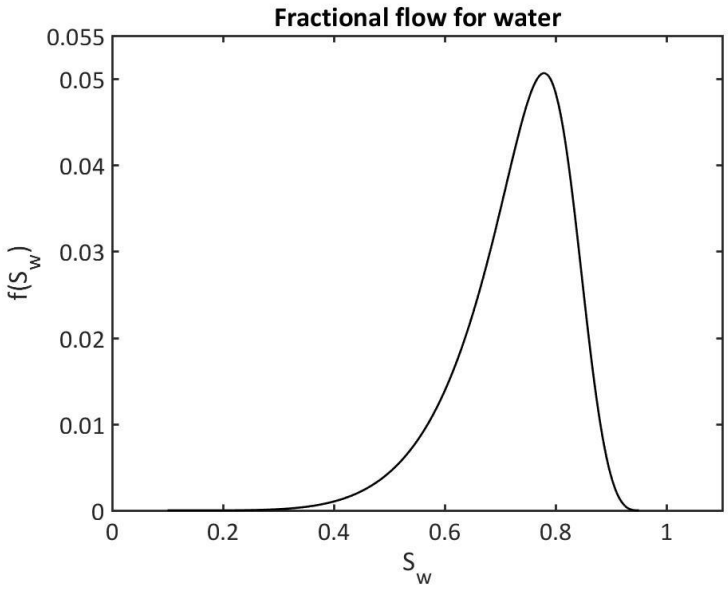

Figure 5.11 Fractional flow of water for buoyancy driven flow.

The flow curve in figure 5.11 can be described by the concept of waves. In figure 5.12 the initial gas saturation in the plume is assumed to be 50 % and the irreducible water and gas saturation is 0.1 and 0.05, respectively. We also assume that the area in front of the plume is entirely brine saturated. Based on these values we can describe the fractional flow function with three shock waves and two rarefaction waves as shown in figure 5.12.

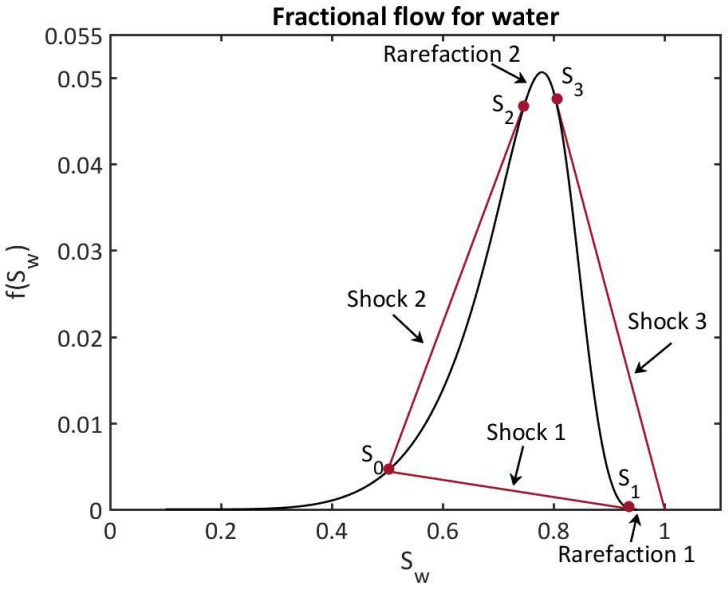

Figure 5.12 Fractional flow curve explained with the concept of waves.

Figure 5.13 shows the final saturation profile based on the flow function in figure 5.12. The first shockwave occurs between the initial gas saturation in the plume, S_0, and the gas saturation at S_1. This shock is located at the bottom boundary of the plume and is travelling upwards. From the irreducible gas saturation to S_1 there is a rarefaction wave. The difference between the saturation at S_1 and the residual gas saturation is very small and the rarefaction wave is barely noticeable on the plot. The second shockwave is located between S_0 and S_2 and is traveling downwards. The last shockwave occurs between S_3 and S=1, and propagates upwards at the top of the plume. A second rarefaction wave is located between S_2 and S_3.

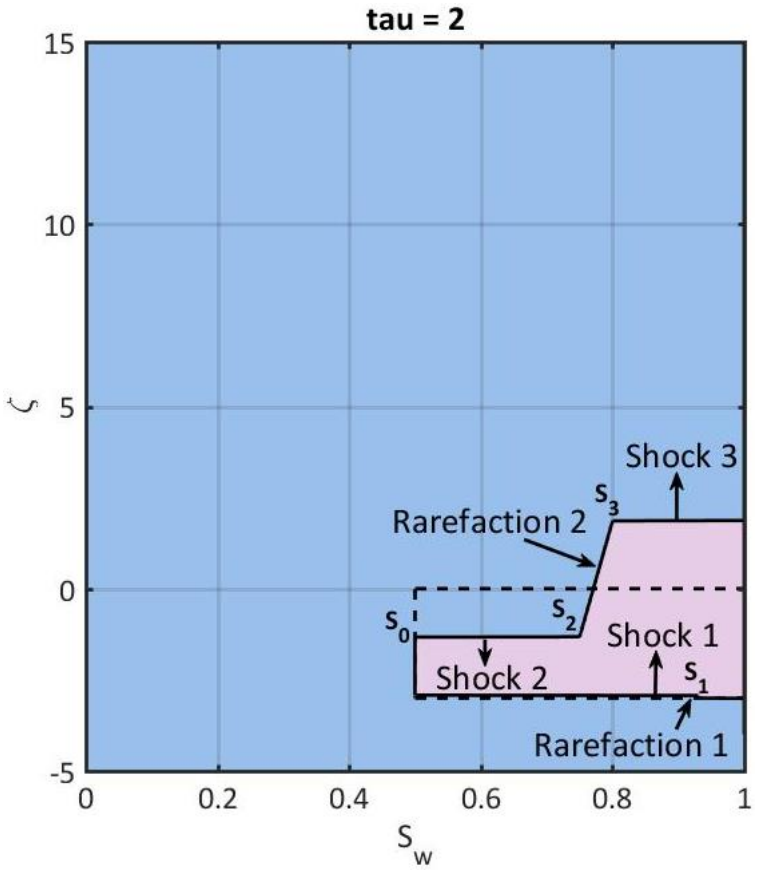

Figure 5.13 Final saturation profile for the gravity driven fractional flow function. The stippled line indicates the initial conditions.

The velocity of the shock fronts and rarefaction waves can according to Silin et al. (2009b) be expressed as

$$V_S(S_1, S_2) = -\frac{1}{\phi}\frac{f(S_2) - f(S_1)}{S_2 - S_1}, \tag{5.49}$$

and

$$V_r(S) = -\frac{1}{\phi} f'(S), \tag{5.50}$$

respectively. Here V_s denotes the velocity of the shock front and V_r denotes the velocity of the rarefaction wave. S_1 and S_2 denotes the brine saturation ahead and behind a front, respectively.

In physical units the shockwave velocity can be expressed as

$$v = -\frac{k_i(\rho_w - \rho_g)g}{\phi_i \mu_w}\frac{f(S_2) - f(S_1)}{S_2 - S_1}. \tag{5.51}$$

The provided solution works for the case where the evolution of the plume in a homogenous layer is considered.

For case two where the evolution across a horizontal interface is evaluated the approach follows the solution given in section 3.3 in Silin et al. (2009b). On both sides of an interface, the Darcy velocity of gas must be the same. The solution to Silin et al., (2009) is based on finding the saturation in the lower layer that makes Darcy velocity in the lower layer match the maximum Darcy velocity in upper layer. The solution depends on the five different variables. These are S', S*, S_{max}, v_1 and v_2. The Matlab script for this solution is given in Appendix D.

6 Results

In this chapter the geological model will be integrated with the mathematical model to display how the gas plume will evolve and propagate in layers with different properties. The model will be used to display two different cases. In case one we consider the evolution of a plume in a homogenous layer. In case two we consider the evolution of a plume at a horizontal boundary between different lithologies.

In all cases the initial conditions state that the layers are water wet and that the gas is the propagating non-wetting phase. The relative permeability functions used for the calculations are summarised in Appendix C. The values of the different parameters used to make the plots are given in Table 6.1. These values have been used for all plots unless stated otherwise.

Table 6.1 Values of the parameters used in the calculations

S_{wr}	0.1	**g**	9.81 m/s^2
S_{gr}	0.05	**Permeability reservoir**	571 mD
λ (model parameter)	0.457	**Permeability cap rock**	0.5 mD
μ_g	$5 \cdot 10^{-5}$ Pa·s	**Permeability overburden**	23 mD
μ_w	$5 \cdot 10^{-4}$ Pa·s	**ϕ reservoir**	26%
ρ_g	1000 kg/m^3	**ϕ cap rock**	8%
ρ_w	561 kg/m^3	**ϕ overburden**	15%

6.1 Case 1: Evolution of a gas plume in a homogenous layer

In case one we consider the evolution of a plume in the reservoir of the geological model. Figure 6.1 shows how the plume of gas evolves in the reservoir. The initial saturation of the gas is 50% and the top of the plume at initial conditions is located at 0 m. Based on figure 6.1 the evolution of the plume consists of a different number of shock and rarefaction waves at different times. The saturation and direction of propagation of the different shocks differ. It takes the plume approximately 103 days to propagate ca. 40 m. After this the velocity of the plume is significantly reduced.

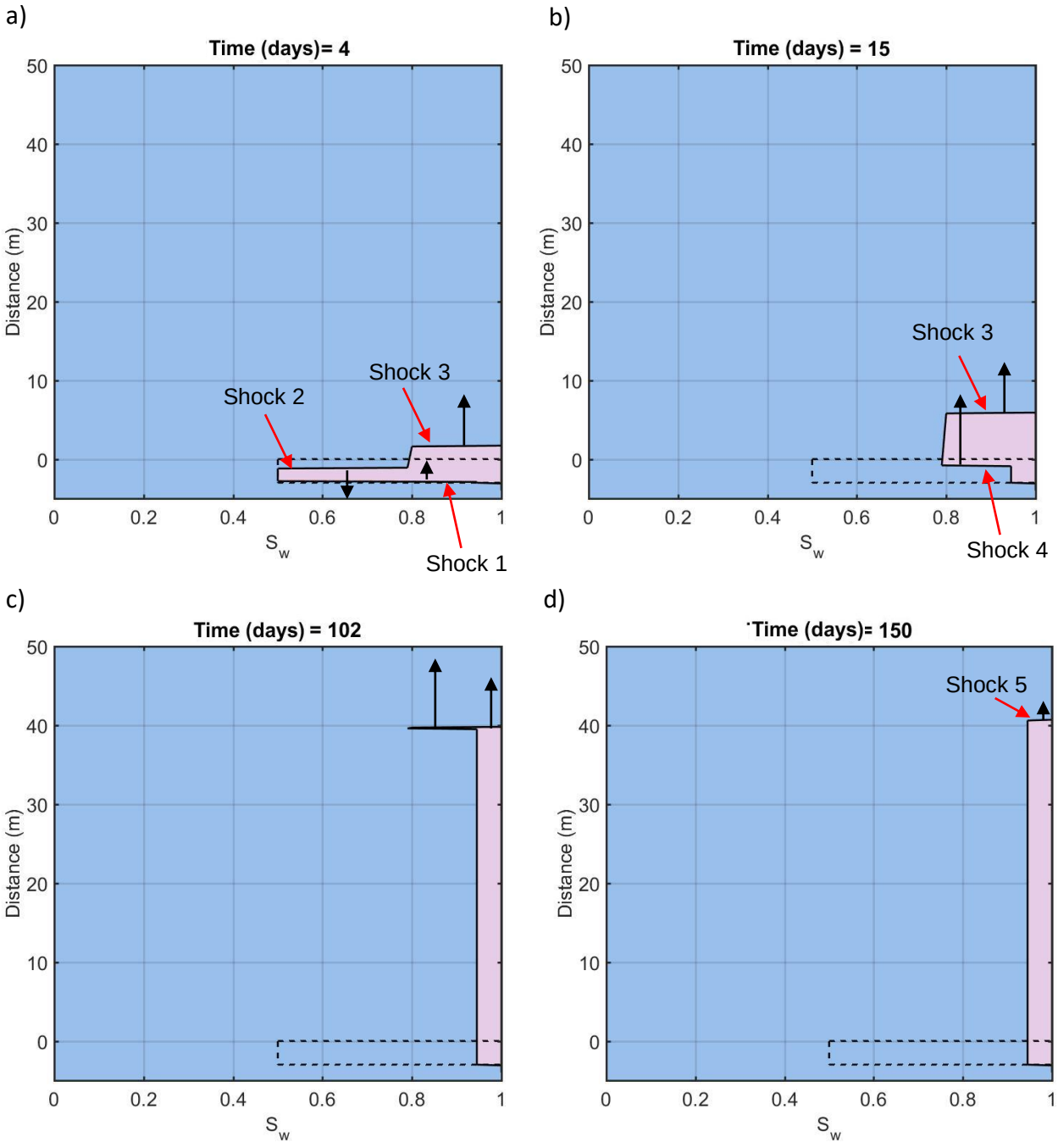

Figure 6.1 Saturation profile showing the evolution of a gas plume at a) 4 days. b) 15 days. c) 102 days. d) 150 days. The black arrows indicate the direction and relative velocity of the waves.

Based on figure 6.1, the model predicts that the evolution of the plume in the reservoir unit (Fig. 6.1) can be separated into three different stages. Stage one (fig 6.1a) describes the initial plume evolution. It is characterised by three shock waves and two rarefaction waves. Shock 1 is travelling upwards with a velocity of V_1, shock 2 is traveling downwards with a velocity of V_2 and shock 3 is travelling upwards with a velocity of V_3. When shock 1 and 2 meet, the bottom part of the plume collapses and stage one is over. This initiates stage 2 (fig 6.1 b-c), which consist of two shock waves and two rarefaction waves. Shock 3 is propagating upwards with the same velocity and a new shockwave (shock 4) is initiated at the bottom propagating upwards with a velocity of V_4. At this stage shock 4 is travelling faster than shock 3 at the top of the plume. When shock 4 and 3 catch up, the top part of the plume collapses and stage two is over. This initiates the final stage (Fig. 6.1 d) consisting of shock wave 5 propagating with a velocity of V_5 and a rarefaction wave. The saturation of the plume at this point is close to the residual gas saturation and the rarefaction wave characterises most of the profile. The velocity of shock 5 is very small and the propagation of the plume at this stage is significantly reduced. The evolution of the plume at this stage is barely noticeable on the saturation profile compared to the other stages (see how little the plume has evolved between fig 6.1 c and d). The different shock velocities are summarised in table 6.1.

Table 6.2 Summary of the different shockwave velocities in the reservoir

Unit	**V_1**	**V_2**	**V_3**	**V_4**	**V_5**	
Reservoir	0.014	-0.28	0.39	0.46	$2.84\ 10^{-4}$	**m/day**

The time it takes for each stage of the plume evolution to occur can also be visualised by plotting the different shock front velocities. Figure 6.2 shows a plot of the velocities of the different shockswaves in the reservoir. This figure can as with figure 6.1, be divided into three areas. In the beginning, there are three velocities present, V_1, V_2 and V_3. After approximaltey 10 days, V_1 and V_2 intersect. This initiates stage 2 and a new shock front with velocity V_4. At this point V_1 and V_2 cease to exist. Stage 2 consits of two shocks. This stages lasts until V_3 intersects with V_4 at around 103 days. Based on figure 6.2 we can see that when two velocities intersect, a new stage is initiated. Note that the saturations of the shocks are needed to calcualte their velocities.

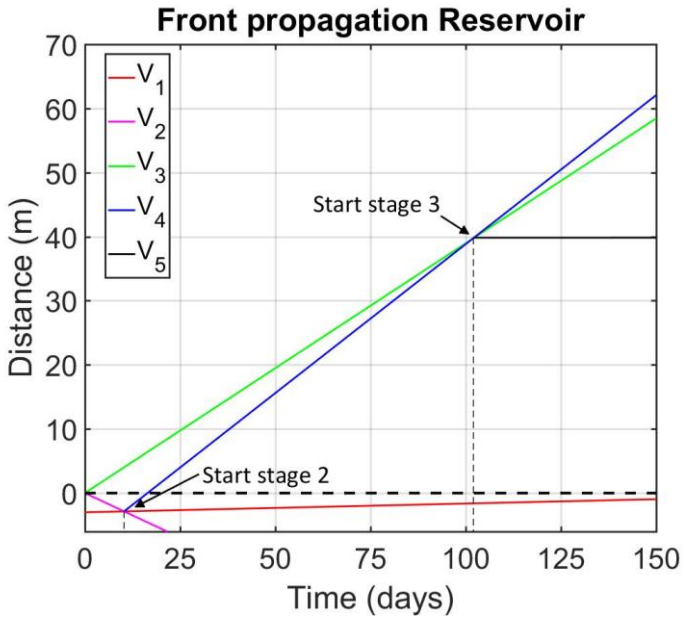

Figure 6.2 Velocity plot of the different shocks in the reservoir.

6.2 Case 2: evolution of a plume at a horizontal interface

In case two we consider the evolution of a plume propagation through a a horizontal boundary with different porosities and permabilities below and above the boundary. Here we consider only the evolution of the top part of the propagating plume. As an example we consider the boundary between the reservoir and overburden. The reservoir lays beneath the boundary. Figure 6.3a shows the velocity of the reflected (v_1) and transmitted (v_2) wave across the boundary. Figure 6.3b-d shows the final saturation profile for the same waves at different times. The saturation profiles are characterised by three different saturations and two different velocities. The boundary between the two rocks is situated at 0 m. The velocity of the transmitted and reflected wave is ≈0.029 m/day and ≈-0.23 m/day, respectively.

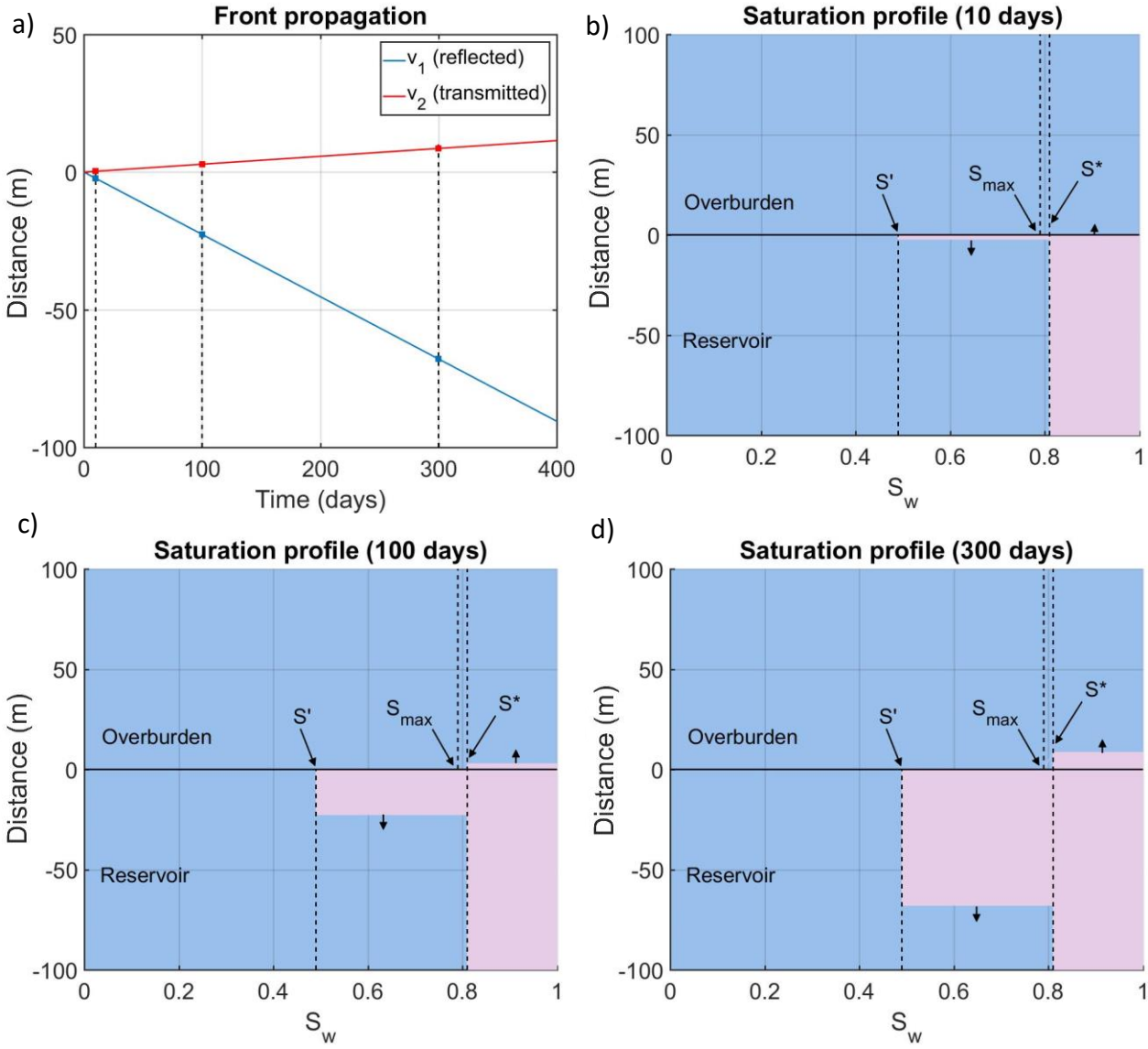

Figure 6.3 a) Velocity of the reflected and transmitted wave between the reservoir and overburden. b) Saturation profile after 10 days. c) Saturation profile after 100 days. d) Saturation profile after 300 days.

The model predicts that when the top part of a plume in the reservoir encounters the overburden where the permeability and porosity are significantly lower, the gas will start to accumulate beneath the boundary. This happens because the overburden is not capable of supporting the gas flow from the reservoir. The gas saturation below the boundary will increase to a certain saturation denoted with S'. This decrease in water saturation (increase in gas saturation) slows down the velocity of the plume. Gas accumulation at the boundary initiates two shockwaves, one in the overburden and one in the reservoir. The shockwave above the interface propagates upwards with velocity V_2 and saturation S*. The shockwave below the boundary propagates downward with velocity v_1 and saturation S'. S_{max} denotes the saturation corresponding to the maximum of the fractional flow function.

7 Discussion

7.1 Case 1

The model showed that the evolution of a plume could be divided into three different stages. What happens if we change the properties of the homogenous media it evolves in? Figure 7.1 shows the different velocities of the shock waves in the reservoir, overburden and cap rock unit of the geological model. The initial conditions are the same. The velocities of the different shocks in the different layers are summarised in table 7.1

Table 7.1 Summary of the shock wave velocities in the different layers

Unit	V_1	V_2	V_3	V_4	V_5	
Reservoir	0.014	-0.28	0.39	0.46	$2.84\ 10^{-4}$	**m/day**
Cap rock	0.0014	-0.0288	0.040	0.0482	$1.23\ 10^{-5}$	**m/year**
Overburden	$5.37\ 10^{-4}$	-0.011	0.015	0.018	$4.70\ 10^{-6}$	**m/day**

Based on figure 7.1, we see that the evolution of the plume in all layers can be divided into three stages. If we compare the three different cases it takes the plume approximately 10 days, 261 days and 100 years to reach stage 2 in the reservoir, overburden and cap rock, respectively. Stage three is initiated at approximately day 105 and day 2600 in the reservoir and overburden, respectively, whereas in the cap rock the same stage starts at ca. 1000 years. Based on figure 7.1 we can see that the evolution of the plume is the same. However, the time taken for it to reach the different stages depends very much on the properties of the layer. Changing these alters the velocities of the different shock waves significantly as seen in table 7.1 and figure 7.1.

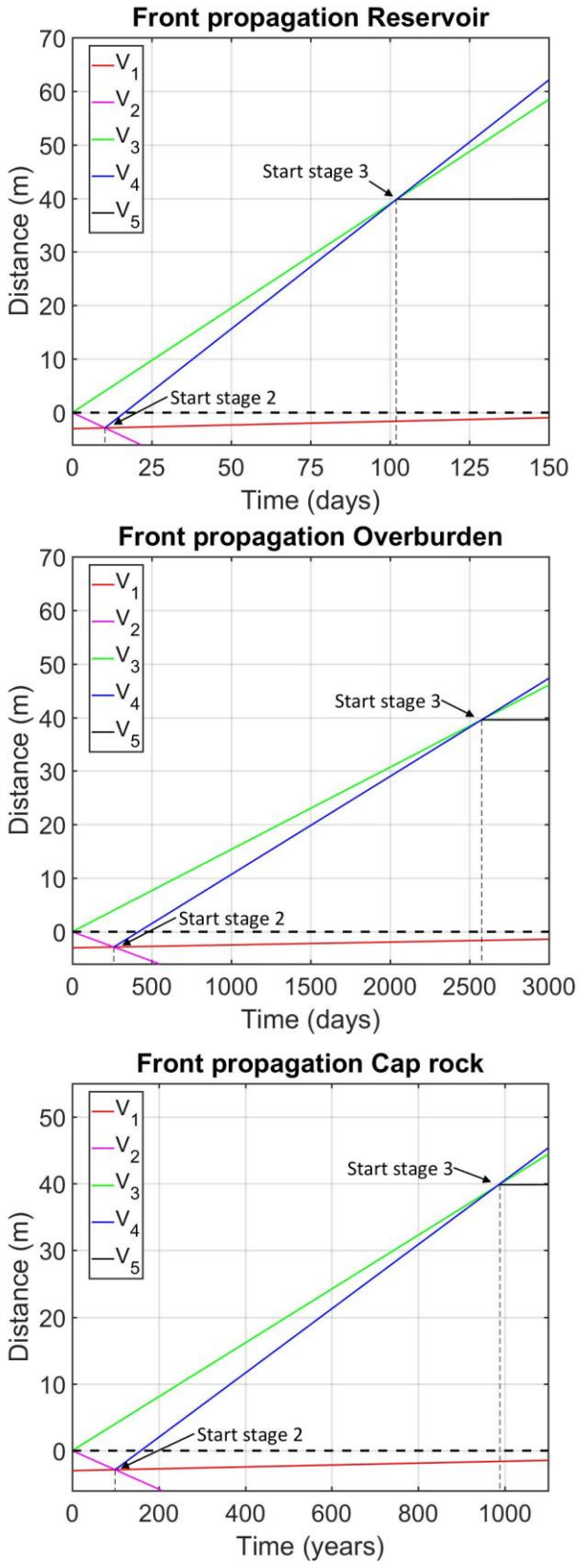

Figure 7.1 Velocity plots for the reservoir, overburden and cap rock.

From equation (5.36) and (5.51), we see that the velocity of the shock fronts rely on both rock (permeability and porosity) and fluid (density and viscosity) properties. In the previous examples, the rock properties were modified whereas the fluid properties remained the same. What happens if the rock properties remains unaltered and some of the fluid properties change? Figure 7.2 shows the plot of the fractional flow function in equation (5.36) for three different water viscosities. The gas viscosity ($5 \cdot 10^{-5}$ Pa·s) remains the same in all cases.

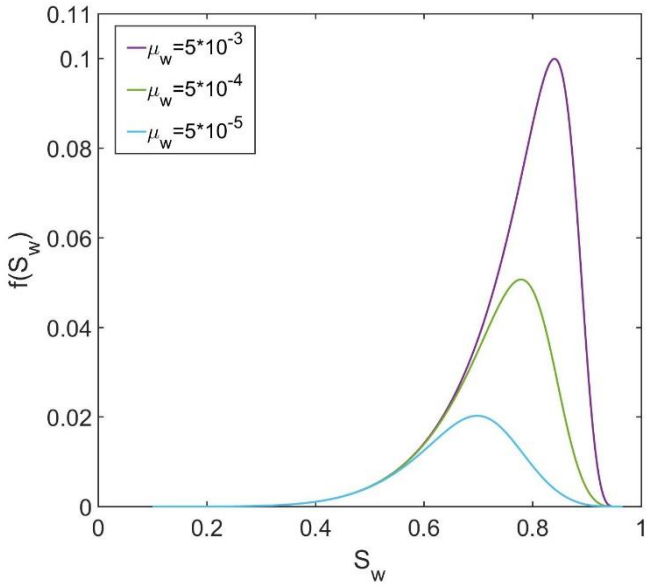

Figure 7.2 Fractional flow function for different values of water viscosity.

The fractional flow will increase as the water viscosity increase (Fig. 7.2). Using the solution introduced in subchapter 5.2.1 on figure 7.2 we see that the three initial shocks will have different saturations depending on the viscosity ratio between the gas and water. A new velocity plot is generated in figure 7.3 for the case where the water viscosity has a value of $5 \cdot 10^{-3}$ Pa·s.

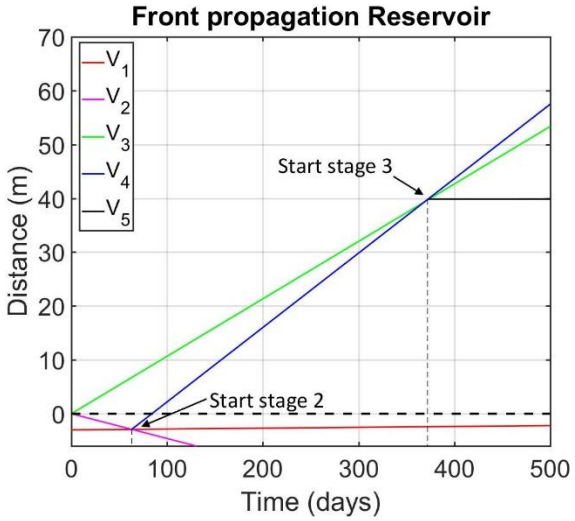

Figure 7.3 Velocity plot for the reservoir unit with a water viscosity of $5 \cdot 10^{-3}$ Pa·s.

Comparing figure 6.2 and figure 7.3 we see that the time taken for the plume to reach the different stages has increased. With a water viscosity of $5 \cdot 10^{-3}$ Pa·s stage 2 is initiated at day 63 and stage 3 at day 372, compared to 10 and 103 days, respectively. An increase in viscosity appear to affect the velocity in the same way as a decrease in porosity and permeability does.

7.2 Case 2

The model showed that the evolution of the top part of a plume between the reservoir and overburden caused gas to accumulate beneath the boundary. What happens if we further reduce the porosity and permeability of the layer above? E.g. let us look at the boundary between the reservoir and the cap rock.

Figure 7.4a shows the velocity of the reflected and transmitted wave across the boundary between the reservoir (v_1) and cap rock (v_2). Figure 7.4b shows the final saturation profile for the same wave at 300 days. The boundary between the two rocks is situated at 0 m. The velocity of the transmitted and reflected wave is ≈0.0012 m/day and ≈-0.1553 m/day, respectively.

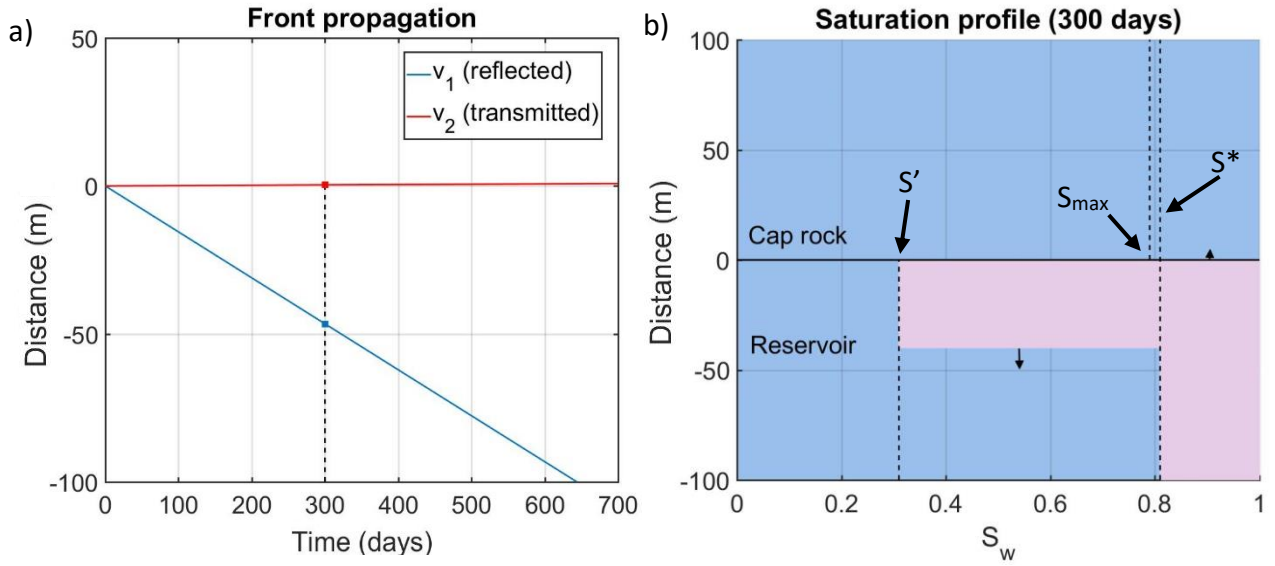

Figure 7.4 a) Velocity of the reflected and transmitted wave between the reservoir and cap rock. b) Saturation profile after 300 days.

Comparing the reservoir/cap rock case with the reservoir/overburden example we see that S_{max} and S* remains the same. However, the gas accumulating below the boundary reaches a higher gas saturation in the former example causing a reduction in S'. The velocity of the transmitted wave in the cap rock is also significantly lower than the transmitted wave in the overburden. The velocity of the shockwave in the reservoir is also reduced. However, the alteration is not as significant as the change of velocity in the cap rock. Due to the low transmitted wave velocity the advance of the plume is not noticeable on the saturation profile.

What happens if the contrast in permeability and porosity between the reservoir unit and overlying unit is not that significant? E.g. let us look at the boundary between the reservoir and an overlying unit (Unit A) with porosity and permeability of 20% and 400 mD, respectively.

Figure 7.5a shows the velocity of the reflected (v_1) and transmitted (v_2) wave across the boundary between the reservoir and Unit A (v_2). Figure 7.5b shows the final saturation profile for the same waves at 100 days. The boundary between the two rocks is situated at 0 m. The velocity of the transmitted and reflected wave is ≈0.38 m/day and ≈-0.13 m/day, respectively.

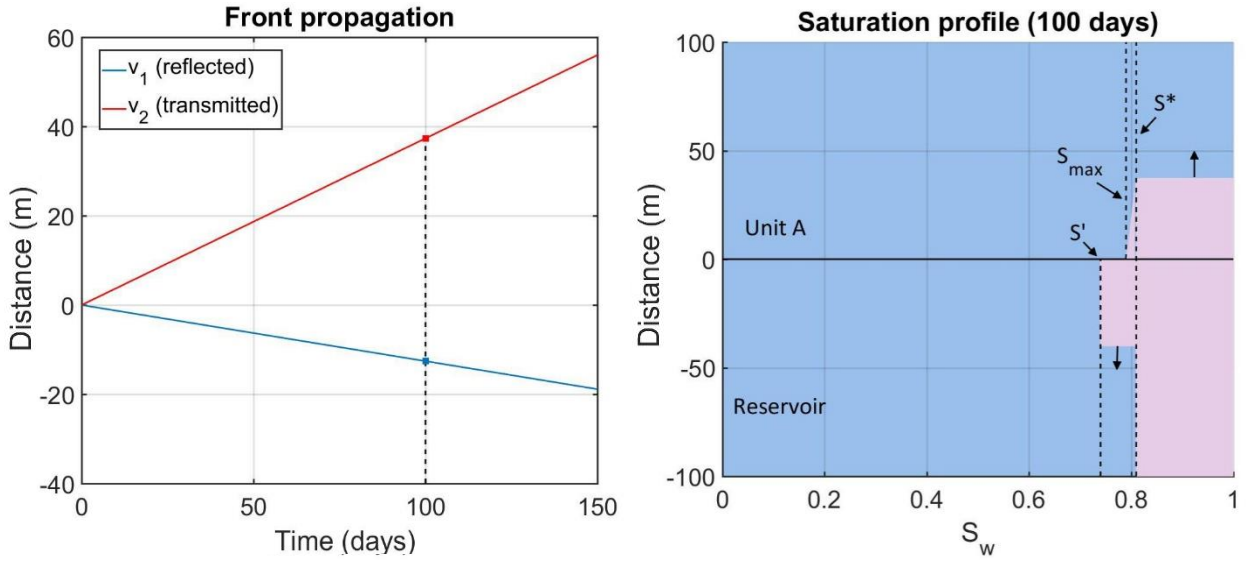

Figure 7.5 a) Velocity of the reflected and transmitted wave between the reservoir and Unit A. b) Saturation profile after 100 days.

Comparing this example with the reservoir/overburden case we see that S_{max} and S* remains the same. There is still an accumluation of gas below the boundary, however the gas saturation is much lower, causing an increase in S'. The increase in S' cause a significant increase in v_2 and a decrease in v_1.

Looking at this from a geological perspective, we see that the cap rock significantly slows down the propagation of the plume compared to the overburden and Unit A. The model shows that the sealing effect of the cap rock is better than the sealing effect of the other units.

The model only displayed boundaries where the permeability and porosity were higher in the underlying unit. What happens if the permeability and porosity above the interface is higher? According to Silin et al., (2006), the type of flow could be affected by such differences. Figure 7.6 shows two different ways a plume of gas may evolve at a boundary. If the leak from a gas source is intense a continuous plume may form (fig 7.6a). However, if the plume enters a high permeability area, the gas leak may not be intense enough to support the plume. This means that the top part of the plume may be separated from the bottom, dividing the plume into several parts (fig 7.6b) (Silin et al., 2006).

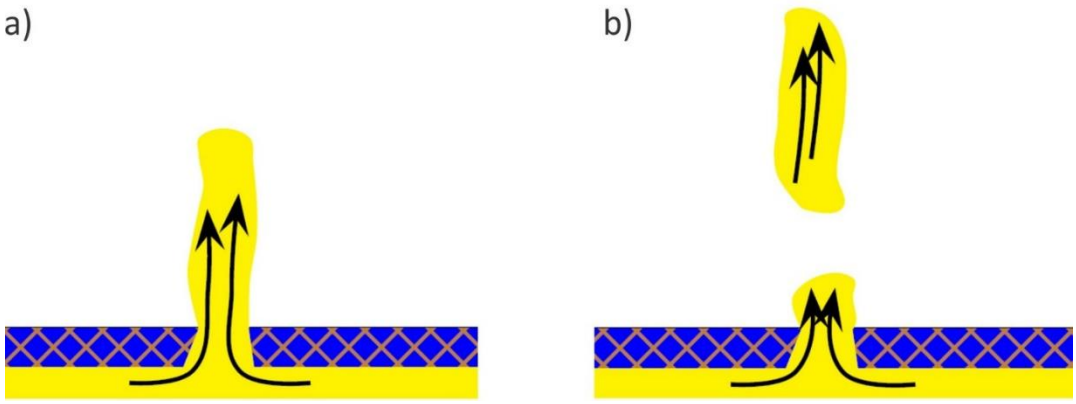

Figure 7.6 a) Continuous plume. b) Separation of plume into several parts. Modified from Silin et al., (2006).

7.3 General remarks

Both the geological and mathematical model has been simplified and many assumptions were made. A crucial assumption in the derivation of the mathematical model is that we neglect the capillary pressure (eqs. (5.46)). This is necessary to obtain a mathematical model that has analytical solutions, i.e., that we can solve without resorting to numerical approaches. Another important assumption is the assumption that the fluid phases are incompressible, meaning that the density is constant with a change in depth (change in pressure and temperature). This is a reasonable assumption for the liquid phase, however gas tends to either expand or contract with changes in pressure and temperature (Selley & Sonnenberg, 2015).

One of the most important factors in the geological model is the permeability estimation. Timur's (1968) equation is very sensitive to changes in porosity and irreducible water saturation. E.g. if the porosity of the reservoir was interpreted to be 25% instead of 26% the permeability is reduced by almost 100 mD. Averaging of the values from the log data and extrapolating them to apply for the whole unit are examples of other simplifications. The well only penetrates a small part of a bigger formation and in reality, there is definitely both lateral and vertical alterations within the formation. However, for this thesis the main objective was to look at how a plume would propagate in and through geological layers with different physical properties. The values obtained

from the geophysical data we had available were used to provide realistic parameter values as input for the mathematical model.

An important factor that was left out from the mathematical model was the degree of faulting. Even though this topic is outside the scope of this thesis, faults are important factors when discussing fluid flow. The identified faults in the cap rock are according to Andreassen et al. (2007a) Eocene bound polygonal faults formed by rapid loading of dense glacigenic sediments. These faults could work as potential fluid conduits and compromise the seal integrity. However, sealing units with polygonal faults of Eocene age in the North Sea overlie many Paleocene reservoirs, suggesting that the faults do not necessarily compromise the sealing effect (Cartwright et al., 2007). However, Cartwright et al. (2007) also suggest that there may be specific circumstances in which polygonal faults might be reactivated under later stress conditions, threatening the trap integrity. With the Barents Sea being subject to heavy uplift and erosion during the Cenozoic, faults could have been reactivated and worked as potential fluid conduits. Andreassen et al. (2007) also suggests that the area has experienced cycles of fluid expulsion and migration due to glacial-interglacial cycles.

Silin et al. (2009b) showed that the plume propagation in a highly permeable region in a formation, such as a fracture, is much faster than the propagation through the rest of the formation. Based on this, if we were to account for the faults in the model the velocity of the plume would most likely increase when encountering them.

We could question the range validity and the practical applicability of the mathematical plume propagation model due to the many assumptions and simplifications. In particular, it is well known that the capillary pressure is the main resisting force for fluid flow (e.g., Schowalter, 1979) and taking this physical effect into account would probably affect the modelled results significantly. However, it is this particular assumption that renders the model analytically tractable, so the model might become complicated to solve if capillary pressure effects are included.

8 Summary

8.1 Conclusion

- A geological model was made based on geophysical data from the Sørvestsnaget Basin.
- A model for vertical gas plume migration was derived based on the original Buckley-Leverett model for two-phase flow.
- The two models were integrated to display the propagation of a plume in a homogenous layer and at a horizontal boundary between different lithologies.
- This thesis shows that the propagation of a gas plume depends on both fluid and rock properties.

8.2 Recommendations for future work

We suggest that one attempts to develop a model with fewer simplifications and assumptions. In particular, this applies to the neglect of the effects of the capillary pressure, as this is certainly a major factor controlling fluid flow.

Another idea would be to derive and solve a multi-layer model as that would allow us to model geological settings that are more realistic.

We suggest that this work is generalized to include an additional component, so that the simultaneous propagation of oil, water and gas can be handled.

Finally, in this thesis we only evaluated changes in rock properties and fluid properties individually. It would be useful to see how the results were affected if we changed the rock and fluid properties simultaneously.

9 References

ABDALLAH, W., BUCKLEY, J. S., CARNEGIE, A., BERND HEROLD, J. E., FORDHAM, E., GRAUE, A., CLAUDE SIGNER, T. H. N. S., HUSSAIN, H., MONTARON, B. & ZIAUDDIN, M. (2007). Fundamentals of Wettibility. *Oilfield Review*, p. 44-61

ALLABY, M. (2013). *A dictionary of geology and earth sciences*: Oxford University Press, p. 436.

ANDREASSEN, K., NILSSEN, E. G. & ODEGAARD, C. M. (2007a). Analysis of shallow gas and fluid migration within the Plio-Pleistocene sedimentary succession of the SW Barents Sea continental margin using 3D seismic data. *Geo-Marine Letters*, 27 (2-4), p. 155-171

ANDREASSEN, K., ØDEGAARD, C. & RAFAELSEN, B. (2007b). Imprints of former ice streams, imaged and interpreted using industry three-dimensional seismic data from the south-western Barents Sea. *Geological Society, London, Special Publications*, 277 (1), p. 151-169

ANDREASSEN, K. (2009). MARINE GEOPHYSICS, Lecture Notes for Geo-3123. *University of Tromsø*

AYAN, C., COLLEY, N., COWAN, G., EZEKWE, E., WANNELL, M., GOODE, P., HALFORD, F., JOSEPH, J., MONGINI, A., OBONDOKO, G. & POP, J. (1994). Measuring Permeability Anisotropy - the Latest Approach. *Oilfield Review*, 6 (4), p. 24-35

BADLEY, M. E. (1985). *Practical seismic interpretation*. Boston: International Human Resources Development Corporation, p. 266.

BARKER, C. (1980). Primary migration-the importance of water-organic-mineral matter interactions in the source rock. *AAPG Studies in Geology*, 10, p. 19-31

BEARD, D. C. & WEYL, P. K. (1973). Influence of Texture on Porosity and Permeability of Unconsolidated Sand. *American Association of Petroleum Geologists Bulletin*, 57 (2), p. 349-369

BEDRIKOVETSKY, P. (2013). *Mathematical theory of oil and gas recovery: with applications to ex-USSR oil and gas fields*, b. 4: Springer Science & Business Media, p. 575.

BELKNAP, W. B., DEWAN, J. T., KIRKPATRICK, C., MOTT, W. E., PEARSON, A. & RABSON, W. (1959). API calibration facility for nuclear logs. *Drilling and production practice*, p. 289-317

BJØRLYKKE, K. (2015). Petroleum Migration. In: Bjørlykke, K. (eds.) *Petroleum Geoscience - From Sedimentary Environments to Rock Physics*. 2 ed.: Springer-Verlag Berlin Heidelberg, p. 373-384.

BROOKS, R. & COREY, T. (1964). HYDRAU uc Properties Of Porous Media. *Hydrology Papers, Colorado State University*, 24, p. 37

BROWN, A. R. (2011). *Interpretation of three-dimensional seismic data*: Society of Exploration Geophysicists and American Association of Petroleum Geologists, p. 615.

BUCKLEY, S. E. & LEVERETT, M. C. (1942). Mechanism of fluid displacement in sands. *Transactions of the American Institute of Mining and Metallurgical Engineers*, 146, p. 107-116

CARTWRIGHT, J., HUUSE, M. & APLIN, A. (2007). Seal bypass systems. *AAPG bulletin*, 91 (8), p. 1141-1166

CATHLES, L. M., SU, Z. & CHEN, D. F. (2010). The physics of gas chimney and pockmark formation, with implications for assessment of seafloor hazards and gas sequestration. *Marine and Petroleum Geology*, 27 (1), p. 82-91

CERVENY, K., DAVIES, R., DUDLEY, G., FOX, R., KAUFMAN, P., KNIPE, R. & KRANTZ, B. (2004). Reducing uncertainty with fault-seal analysis. *Oilfield Review*, 16 (4), p. 2005

CHOPRA, S., CASTAGNA, J. & PORTNIAGUINE, O. (2006). Seismic resolution and thin-bed reflectivity inversion. *CSEG recorder*, 31 (1), p. 19-25

COREY, A. T. (1954). The interrelation between gas and oil relative permeabilities. *Producers monthly*, 19 (1), p. 38-41

DANDEKAR, A. Y. (2013). *Petroleum reservoir rock and fluid properties*: CRC press.

DARCY, H. (1856). *Les fontaines publiques de la ville de Dijon: exposition et application*: Victor Dalmont, p. 647.

DICKEY, P. A. (1969). Increasing concentration of subsurface brines with depth. *Chemical Geology*, 4, p. 361-370

DORE, A. G. (1995). Barents Sea Geology, Petroleum Resources and Commercial Potential. *Arctic*, 48 (3), p. 207-221

DOWNEY, M. W. (1994). Hydrocarbon seal rocks. In: Magoon, L. B. & Dow, W. G. (eds.). 60 *The Petroleum System, From Source to trap*. Tulsa: AAPG Memoir, p. 159-164.

ENGLAND, W. A. (1994). Secondary migration and accumulation of hydrocarbons. In: Magoon, L. B. & Dow, W. G. (eds.). 60 *The Petroleum System, From Source to trap*: AAPG Memoir, p. 211-217.

FALEIDE, J. I., GUDLAUGSSON, S. T. & JACQUART, G. (1984). Evolution of the western Barents Sea. *Marine and Petroleum Geology*, 1 (2), p. 123-150

FALEIDE, J. I., GUDLAUGSSON, S. T., ELDHOLM, O., MYHRE, A. M. & JACKSON, H. R. (1991). Deep Seismic Transects across the Sheared Western Barents Sea-Svalbard Continental-Margin. *Tectonophysics*, 189 (1-4), p. 73-89

FALEIDE, J. I., VÅGNES, E. & GUDLAUGSSON, S. T. (1993). Late Mesozoic-Cenozoic Evolution of the South-Western Barents Sea in a Regional Rift Shear Tectonic Setting. *Marine and Petroleum Geology*, 10 (3), p. 186-214

FALEIDE, J. I., SOLHEIM, A., FIEDLER, A., HJELSTUEN, B. O., ANDERSEN, E. S. & VANNESTE, K. (1996). Late Cenozoic evolution of the western Barents Sea-Svalbard continental margin. *Global and Planetary Change*, 12 (1-4), p. 53-74

FALEIDE, J. I., BJØRLYKKE, K. & GABRIELSEN, R. H. (2015). Geology of the Norwegian Continental Shelf. In: Bjørlykke, K. (eds.) *Petroleum Geoscience - From Sedimentary Environments to Rock Physics*. 2 ed.: Springer-Verlag Berlin Heidelberg, p. 603-637.

FALODE, O. & MANUEL, E. (2014). Wettability effects on capillary pressure, relative permeability, and irredcucible saturation using porous plate. *Journal of Petroleum Engineering*, p. 1-12

FLOODGATE, G. D. & JUDD, A. G. (1992). The Origins of Shallow Gas. *Continental Shelf Research*, 12 (10), p. 1145-1156

FOSSEN, H., DAKKMAN, W. & ANDERSEN, T. B. (2006). Fjellkjeden går til grunne - Kaledonidene brytes ned; 405-359 millioner år. In: Ramberg, I. B., Bryhni, I. & Nøttvedt, A. (eds.) *Landet Blir til - Norges geologi*: Norsk Geologisk Forening, p. 230-257.

GLORSTAD-CLARK, E., FALEIDE, J. I., LUNDSCHIEN, B. A. & NYSTUEN, J. P. (2010). Triassic seismic sequence stratigraphy and paleogeography of the western Barents Sea area. *Marine and Petroleum Geology*, 27 (7), p. 1448-1475

GUDLAUGSSON, S. T., FALEIDE, J. I., JOHANSEN, S. E. & BREIVIK, A. J. (1998). Late Palaeozoic structural development of the South-western Barents Sea. *Marine and Petroleum Geology*, 15 (1), p. 73-102

HALLAND, E., BJØRNESTAD, A., MAGNUS, C., RIIS, F., MELING, I. M., GJELDVIK, I. T., MUJEZINOVIC, J., BJORHEIM, M., RØD, R. S. & PHAM, V. T. H. (2014). *Compiled CO2 atlas for the Norwegian Continental Shelf*.

HAYEK, M., MOUCHE, E. & MÜGLER, C. (2009). Modeling vertical stratification of CO2 injected into a deep layered aquifer. *Advances in Water Resources*, 32 (3), p. 450-462

HENRIKSEN, E., RYSETH, A. E., LARSSEN, G. B., HEIDE, T., RONNING, K., SOLLID, K. & STOUPAKOVA, A. V. (2011). Tectonostratigraphy of the greater Barents Sea: implications for petroleum systems. *Arctic Petroleum Geology*, 35, p. 163-195

HINDLE, A. D. (1997). Petroleum migration pathways and charge concentration: A three-dimensional model. *AAPG bulletin*, 81 (9), p. 1451-1481

HIRASAKI, G. 2009. *Chapter 7 Two Phase, One Dimensional, Displacement* [Online]. Univeristy of Stavanger. Available: http://www1.uis.no/Fag/Learningspace_kurs/PetBachelor/webpage/tech%5CReservoir%5Cceng571%5CCHAP7.pdf [Accessed 13.03.2017].

HJELSTUEN, B. O., ELVERHØI, A. & FALEIDE, J. I. (1996). Cenozoic erosion and sediment yield in the drainage area of the Storfjorden Fan. *Global and Planetary Change*, 12 (1), p. 95-117

HUBBERT, M. K. (1940). The theory of ground-water motion. *The Journal of Geology*, 48 (8, Part 1), p. 785-944

JAOUA, M. (2017). *Solution to Buckley-Leverett Problem*: Montan Universitat, Department og Petroleum Engineering.

JUDD, A. & HOVLAND, M. (2007). *Seabed Fluid Flow : The Impact on Geology, Biology and the Marine Environment*: Cambridge University Press, p. 441.

KAASSCHIETER, E. F. (1999). Solving the Buckley–Leverett equation with gravity in a heterogeneous porous medium. *Computational Geosciences*, 3 (1), p. 23-48

KEAREY, P., BROOKS, M. & HILL, I. (2002). *An introduction to geophysical exploration*: Wiley-Blackwell, p. 262.

KLEPPE, J. (2017). TPG4150 Reservoir Recovery Techniques 2017. Hand-out note 4: Buckley Leverett Analysis. *Norwegian University of Science and Technology*.

KNIES, J., MATTHIESSEN, J., VOGT, C., LABERG, J. S., HJELSTUEN, B. O., SMELROR, M., LARSEN, E., ANDREASSEN, K., EIDVIN, T. & VORREN, T. O. (2009). The Plio-Pleistocene glaciation of the Barents Sea-Svalbard region: a new model based on revised chronostratigraphy. *Quaternary Science Reviews*, 28 (9-10), p. 812-829

KRISTENSEN, T., ROTEVATN, A., MARVIK, M., HENSTRA, G. A., GAWTHORPE, R. L. & RAVNÅS, R. (2017). Structural evolution of sheared margin basins: the role of strain partitioning. Sørvestsnaget Basin, Norwegian Barents Sea. *Basin Research*, p. 1-23

LAKE, L. W. (1989). Enhanced oil recovery. p. 423

LARSSEN, G., ELVEBAKK, G., HENRIKSEN, L. B., KRISTENSEN, S., NILSSON, I., SAMUELSBERG, T., SVÅNÅ, T., STEMMERIK, L. & WORSLEY, D. (2002). Upper Palaeozoic lithostratigraphy of the Southern Norwegian Barents Sea. *Norwegian Petroleum Directorate Bulletin*, 9, p. 1-69

LEVERETT, M. C. (1941). Capillary behavior in porous solids. . *Trans. AIME*, 142, p. 152-169

LEVERETT, M. C., LEWIS, W. B. & TRUE, M. E. (1942). Dimensional-model studies of oil-field behavior. *Transactions of the American Institute of Mining and Metallurgical Engineers*, 146, p. 175-192

LI, K. & HORNE, R. N. (2006). Comparison of methods to calculate relative permeability from capillary pressure in consolidated water-wet porous media. *Water resources research*, 42 (6), p. 1-9

LIGTENBERG, J. (2005). Detection of fluid migration pathways in seismic data: implications for fault seal analysis. *Basin Research*, 17 (1), p. 141-153

LØSETH, H., GADING, M. & WENSAAS, L. (2009). Hydrocarbon leakage interpreted on seismic data. *Marine and Petroleum Geology*, 26 (7), p. 1304-1319

MAGOON, L. B. & DOW, W. G. (1994). The Petroleum System. In: Magoon, L. B. & Dow, W. G. (eds.). 60 *The Petroleum System, From Source to trap*. Tulsa: AAPG Memoir, p. 3-24.

MARELLO, L., EBBING, J. & GERNIGON, L. (2013). Basement inhomogeneities and crustal setting in the Barents Sea from a combined 3D gravity and magnetic model. *Geophysical Journal International*, 193 (2), p. 557-584

MOORE, W. R., MA, Y. Z., PIRIE, I. & ZHANG, Y. (2016). Chapter 15 - Tight Gas Sandstone Reservoirs, Part 2: Petrophysical Analysis and Reservoir Modeling. In: *Unconventional Oil and Gas Resources Handbook*. Boston: Gulf Professional Publishing, p. 429-448.

NANDA, N. C. (2016). *Seismic Data Interpretation and Evaluation for Hydrocarbon Exploration and Production: A Practitioner's Guide*. A Practitioner's Guide. Cham: Springer International Publishing: Cham.

NJOBUENWU, D. O., OBOHO, E. O. & GUMUS, R. H. (2007). Determination of contact angle from contact area of liquid droplet spreading on solid substrate. *Leonardo Electronic Journal of Practices and Technologies*, 10, p. 29-38

NORWEGIAN PETROLEUM DIRECTORATE. 2003. Available: http://factpages.npd.no/ReportServer?/FactPages/PageView/wellbore_exploration&rs:Command=Render&rc:Toolbar=false&rc:Parameters=f&NpdId=4129&IpAddress=46.9.185.93&CultureCode=nb-no [Accessed 18.10.2017].

NØTTVEDT, A. & JOHANNESSEN, E. P. (2006). Grunnlaget for Norges oljerikdom - Seinjura, Et øyhav vokser fram; 161-156 millioner år. In: Ramberg, I. B., Bryhni, I. & Nøttvedt, A. (eds.) *Landet blir til - Norges Geologi*: Norsk Geologisk Forening, p. 382-415.

OHM, S. E., KARLSEN, D. A. & AUSTIN, T. (2008). Geochemically driven exploration models in uplifted areas: Examples from the Norwegian Barents Sea. *AAPG bulletin*, 92 (9), p. 1191-1223

PEAK SEISMIC SOLUTIONS. 2017. *Ocean Bottom Seismic* [Online]. Available: http://peakseismic.com/content/ocean-bottom-seismic.asp [Accessed 13.11.2017].

PEGAZ-FIORNET, S., CARPENTIER, B., MICHEL, A. & WOLF, S. (2012). Comparison between the different approaches of secondary and tertiary hydrocarbon migration modeling in basin simulators. In: Peters, K. E., Curry, D. & Kacewicz, M. (eds.) *Basin Modeling: New Horizons in Research and Applications*: AAPG, p. 221-236.

PETERS, K. E., CURRY, D. & KACEWICZ, M. (2012). An Overview of Basin and Petroleum System Modeling: Definitions and Concepts. In: Peters, K. E., Curry, D. & Kacewicz, M. (eds.) *Basin Modeling: New Horizons in Research and Applications*. 1 ed.: AAPG, p. 1-16.

RESERVIOIRENGINEERINGONLINE. 2014. *Capillary Pressure* [Online]. Available: http://reservoironline.blogspot.no/2014/08/capillary-pressure.html [Accessed 08.04.2018].

RIDER, M. & KENNEDY, M. (2011). *The geological interpretation of well logs*. 3 ed. Scotland: Rider-French Consulting.

ROSLAND, F. A. (2013). *Modelling of water-oil flow in reservoir including the effects from gravity, capillary pressure and water rock chemistry*: University of Stavanger, Faculty of Science and Technology.

RYSETH, A., AUGUSTSON, J. H., CHARNOCK, M., HAUGERUD, O., KNUTSEN, S. M., MIDBOE, P. S., OPSAL, J. G. & SUNDSBO, G. (2003). Cenozoic stratigraphy and evolution of the Sorvestsnaget Basin, southwestern Barents Sea. *Norwegian Journal of Geology*, 83 (2), p. 107-130

SCHLUMBERGER. 1994. *Neutron Porosity Logging Revisited* [Online]. Available: https://www.slb.com/~/media/Files/resources/oilfield_review/ors94/1094/p04_08.pdf [Accessed 30.01.2018].

SCHLUMBERGER. 2017. *Permeability* [Online]. Available: http://www.glossary.oilfield.slb.com/Terms/p/permeability.aspx [Accessed 20.11.2017].

SCHOWALTER, T. T. (1979). Mechanics of secondary hydrocarbon migration and entrapment. *AAPG bulletin*, 63 (5), p. 723-760

SELLEY, R. C. & SONNENBERG, S. A. (2015). *Elements of petroleum geology*. 3rd ed. ed. San Diego, Calif: Academic Press, p. 516.

SHERIFF, R. E. (1985). Aspects of Seismic Resolution. In: Roger, O. B. & Woolverton, D. G. (eds.) *AAPG Memoir 39: Seismic Stratigraphy II: An Integrated Approach to Hydrocarbon Exploration*. Tulsa: AAPG, p. 1-10.

SHERIFF, R. E. (2002). *Encyclopedic dictionary of applied geophysics*: Society of exploration geophysicists, p. 429.

SILIN, D. B., PATZEK, T. W. & BENSON, S. M. (2006). Exact solutions in a model of vertical gas migration. SPE Paper 103156. In: Proceeding of the 2006 SPE Annual Techincal Conference and Exhibition; September 24-27: San Anotnio, TX.

SILIN, D. B., PATZEK, T. W. & BENSON, S. M. (2009a). A Model of Buoyancy-Driven Two-Phase Countercurrent Fluid Flow. *Transport in Porous Media*, 76 (3), p. 449-469

SILIN, D. B., PATZEK, T. W. & BENSON, S. M. (2009b). A one-dimensional model of vertical gas plume migration through a heterogeneous porous medium. *International Journal of Greenhouse Gas Control*, 3 (3), p. 300-310

SMELROR, M., PETROV, O., LARSSEN, G. B. & WERNER, S. (2009). *Atlas : geological history of the Barents Sea*. Trondheim: Geological Survey of Norway, p. 134.

SULAK, A. & DANIELSEN, J. (1988). *Reservoir aspects of Ekofisk subsidence*. Offshore Technology Conference.

TALWANI, M. & ELDHOLM, O. (1977). Evolution of Norwegian Greenland Sea. *Geological Society of America Bulletin*, 88 (7), p. 969-999

TIMUR, A. (1968). *An investigation of permeability, porosity, and residual water saturation relationships*. SPWLA 9th annual logging symposium: Society of Petrophysicists and Well-Log Analysts.

TISSOT, B. & WELTE, D. (1984). *Petroleum Formation and Occurrence*. 2 ed.: Springler-Verlag.

TORSKAYA, T. S., JIN, G. & TORRES-VERDIN, C. (2007). *Pore-level analysis of the relationship between porosity, irreducible water saturation, and permeability of clastic rocks*. SPE Annual Technical Conference and Exhibition: Society of Petroleum Engineers.

TORSVIK, T. H., CARLOS, D., MOSAR, J., COCKS, L. R. M. & MALME, T. N. (2002). Global reconstructions and North Atlantic paleogeography 440 Ma to recent. In: Eide, E. A. (eds.) *BATLAS—Mid Norway plate reconstruction atlas with global and Atlantic perspectives*: Geological Survey of Norway, p. 18-39.

VAN GENUCHTEN, M. T. (1980). A closed-form equation for predicting the hydraulic conductivity of unsaturated soils 1. *Soil science society of America journal*, 44 (5), p. 892-898

VAVRA, C. L., KALDI, J. G. & SNEIDER, R. M. (1992). Geological applications of capillary pressure: a review (1). *AAPG Bulletin*, 76 (6), p. 840-850

WANGEN, M. (1993). Vertical migration of hydrocarbons modelled with fractional flow theory. *Geophysical Journal International*, 115 (1), p. 109-131

WATTS, N. L. (1987). Theoretical aspects of cap-rock and fault seals for single- and two-phase hydrocarbon columns. *Marine and Petroleum Geology*, 4 (4), p. 274-307

WELGE, H. J. (1952). A simplified method for computing oil recovery by gas or water drive. *Journal of Petroleum Technology*, 4, p. 91-98

WORSLEY, D., JOHANSEN, R. & KRISTENSEN, S. E. (1988). The mesozoic and cenozoic succession of Tromsøflaket. In: Dalland, A., Worsley, D. & Ofstad, K. (eds.) *A lithostratigraphic scheme for the mesozoic and cenozoic and succession offshore mid-and northern norway*: Norwegian Petroleum Directorate Bulletin 4, p. 42-65.

WORSLEY, D. (2008). The post-Caledonian development of Svalbard and the western Barents Sea. *Polar Research*, 27 (3), p. 298-317

Appendix A: Buckley-Leverett theory

This appendix shows the derivation of equation (5.9) in chapter 5.1.

$$\frac{1}{kA}\left(q_w \frac{\mu_w}{k_{rw}(S)} - q_o \frac{\mu_o}{k_{ro}(S)}\right) = \frac{\partial P_c}{\partial x} - g(\rho_o - \rho_w)\sin(\alpha) \tag{A.1}$$

Inserting for $q_o = q_t - q_w$ equation (A.1) becomes

$$\frac{1}{kA}\left(q_w \frac{\mu_w}{k_{rw}(S)} - (q_t - q_w)\frac{\mu_o}{k_{ro}(S)}\right) = \frac{\partial P_c}{\partial x} - g(\rho_o - \rho_w)\sin(\alpha). \tag{A.2}$$

Multiplying by kA and rearranging equation (A.2) we get

$$q_w \frac{\mu_w}{k_{rw}(S)} + q_w \frac{\mu_o}{k_{ro}(S)} = q_t \frac{\mu_o}{k_{ro}(S)} + kA\left(\frac{\partial P_c}{\partial x} - g(\rho_o - \rho_w)\,\sin(\alpha)\right). \tag{A.3}$$

Dividing by $\frac{\mu_o}{k_{ro}(S)}$ equation (A.3) becomes

$$q_w \frac{\mu_w k_{ro}(S)}{\mu_o k_{rw}(S)} + q_w = q_t + kA\frac{k_{ro}(S)}{\mu_o}\left(\frac{\partial P_c}{\partial x} - g(\rho_o - \rho_w)\,\sin(\alpha)\right). \tag{A.4}$$

Rearranging equation (A.4) it simplifies to

$$q_w\left(1 + \frac{\mu_w k_{ro}(S)}{\mu_o k_{rw}(S)}\right) = q_t + kA\frac{k_{ro}(S)}{\mu_o}\left(\frac{\partial P_c}{\partial x} - g(\rho_o - \rho_w)\,\sin(\alpha)\right). \tag{A.5}$$

Using $f_w = \frac{q_w}{q_t}$, we get the final expression for the fractional flow:

$$f_w = \frac{q_w}{q_t} = \frac{1 + kA\frac{k_{ro}(S)}{q_t \mu_o}\left(\frac{\partial P_c}{\partial x} - g(\rho_o - \rho_w)\,\sin(\alpha)\right)}{\left(1 + \frac{\mu_w k_{ro}(S)}{\mu_o k_{rw}(S)}\right)}. \tag{A.6}$$

Appendix B: Vertical migration

This appendix show the derivations of some of the equations in chapter 5.2

Remember **g**=-$\hat{z}g$.

Equation (5.33)

Inserting equations (5.24) and (5.25) in (5.32) and solving with respect for$\frac{\partial P_w}{\partial z}$ we get that

$$\frac{k_{rg}(S)k}{\mu_g}\left(-\nabla P_c(S)-\nabla P_w+\rho_g g\right)+\frac{k_{rw}(S)k}{\mu_w}\left(-\nabla P_w+\rho_w g\right)=0 \tag{B.1}$$

Dividing by *k* and expanding the expression we get that

$$-\frac{k_{rg}(S)}{\mu_g}\nabla P_c(S)-\frac{k_{rg}(S)}{\mu_g}\nabla P_w+\frac{k_{rg}(S)}{\mu_g}\rho_g g-\frac{k_{rw}(S)}{\mu_w}\nabla P_w+\frac{k_{rw}(S)}{\mu_w}\rho_w g=0. \tag{B.2}$$

Rearranging and solving with respect to ∇P_w we get that

$$-\frac{\partial P_w}{\partial z}\left(\frac{k_{rg}(S)}{\mu_g}+\frac{k_{rw}(S)}{\mu_w}\right)=\frac{k_{rg}(S)}{\mu_g}\nabla P_c(S)+a\frac{k_{rg}(S)}{\mu_g}g+\frac{k_{rw}(S)}{\mu_w}\rho_w g, \tag{B.3}$$

Which equals to

$$\boldsymbol{\frac{\partial P_w}{\partial z}=-\frac{1}{\frac{k_{rg}(S)}{\mu_g}+\frac{k_{rw}(S)}{\mu_w}}\left(\frac{k_{rg}(S)}{\mu_g}\frac{\partial}{\partial z}P_c(S)+\frac{k_{rg}(S)}{\mu_g}\rho_g g+\frac{k_{rw}(S)}{\mu_w}\rho_w g\right).} \tag{B.4}$$

Proof that eqs. (5.34) and (5.36) are equal.

To simplify the expressions two constants, *a* and *b*, are introduced where

$$a = \frac{k_{rg}(S)}{\mu_g} \text{ and } b = \frac{k_{rw}(S)}{\mu_w}.$$

Combining equation (5.34) and (5.36) we get that

$$-\frac{1}{a+b}\left(a\frac{\partial}{\partial z}P_c(S) + a\rho_g g + b\rho_w g\right) = -\frac{a}{a+b}\left(\frac{\partial}{\partial z}p_c(S) - (\rho_w - \rho_g)g\right) - \rho_w g. \quad \text{(B.5)}$$

Expanding the expression we get that

$$-\frac{a}{a+b}\frac{\partial}{\partial z}P_c(S) - \frac{a}{a+b}\rho_g g - \frac{b}{a+b}\rho_w g = -\frac{a}{a+b}\frac{\partial}{\partial z}p_c(S) + \frac{a}{a+b}\rho_w g - \frac{a}{a+b}\rho_g g - \rho_w g. \quad \text{(B.6)}$$

Removing equal expressions simplifies the previous equation to

$$-\frac{b}{a+b}\rho_w g = -\frac{a}{a+b}\rho_w g - \rho_g g. \quad \text{(B.7)}$$

Multiplying the right side expression with the common denominator gives

$$-\frac{b}{a+b}\rho_w g = \frac{a\rho_w g - a\,\rho_w g\, - b\rho_w g}{a+b}. \quad \text{(B.8)}$$

Cancelling equal expressions and inserting the values for the constants a and b we see that

$$-\frac{\frac{\mathbf{k_{rw}(S)}}{\mathbf{\mu_w}}}{\frac{\boldsymbol{k_{rg}(S)}}{\boldsymbol{\mu_g}} + \frac{\boldsymbol{k_{rw}(S)}}{\boldsymbol{\mu_w}}}\boldsymbol{\rho_w g} = -\frac{\frac{\mathbf{k_{rw}(S)}}{\mathbf{\mu_w}}}{\frac{\boldsymbol{k_{rg}(S)}}{\boldsymbol{\mu_g}} + \frac{\boldsymbol{k_{rw}(S)}}{\boldsymbol{\mu_w}}}\boldsymbol{\rho_w g}. \quad \text{(B.9)}$$

Equation (5.45)

$$W_w = f(S)\left(\frac{1}{(\rho_w - \rho_g)g}\sigma\sqrt{\frac{\phi}{k}}\frac{\partial}{\partial z}J(S) - 1\right) \quad \text{(B.10)}$$

Using the chain rule,

$$\frac{\partial}{\partial z}J(S(z)) = \frac{\partial J(S)}{\partial S}\frac{\partial S}{\partial z}. \quad \text{(B.11)}$$

which can be simplified to

$$\frac{\partial}{\partial z}J(S(z)) = J'(S)\frac{\partial S}{\partial z}. \quad \text{(B.12)}$$

Expressing z as a dimensionless variable,

$z = \zeta H,$

we get that

$$J'(S)\frac{\partial S}{\partial z} = J'(S)\frac{\partial S}{\partial \zeta H} \quad \text{(B.13)}$$

Since H is constant we can write

$$\frac{1}{H}J'(S)\frac{\partial S}{\partial \zeta} \quad \text{(B.14)}$$

Inserting the expression in (B.14) in (B.10) we get that

$$W_w = f(S)\left(\frac{1}{(\rho_w - \rho_g)g}\sigma\sqrt{\frac{\phi}{k}}\frac{1}{H}J'(S)\frac{\partial S}{\partial \zeta} - 1\right). \quad \text{(B.151)}$$

All constants can be combined into one variable y expressed as

$$\gamma = \frac{\sigma}{(\rho_{w-}\rho_g)gH}\sqrt{\frac{\phi}{k}}. \quad \text{(B.16)}$$

Equation (B.15) then simplifies to

$$\boldsymbol{W_w = f(S)\left(\gamma J'(S)\frac{\partial S}{\partial \zeta} - 1\right)} \quad \text{(B.17)}$$

Appendix C: Relative permeability

Two different relationships between the relative permeability (k_{ri}) and water saturation has been used in this thesis. One for the oil/water system in chapter 5.1 and one for the gas/water system in chapter 5.2 and chapter 6. In chapter 5.1 the k_{ri} were calculated based on the Brooks-Corey water and oil relative permeabilites (Brooks & Corey, 1964) which are expressed as

$$k_{rw} = KRW(S_{wn})^{n_w}, \text{ and} \tag{C.1}$$

and

$$k_{ro} = KRO(1 - S_{wn})^{n_o}, \tag{C.2}$$

where

$$S_{wn} = \frac{S - S_{wr}}{1 - S_{wr} - S_{or}}. \tag{C.3}$$

Here, KRW denotes the relative permeability of water at the residual oil saturation and KRO denotes the relative permeability of oil at the residual water saturation. n_w and n_o are the Corey water and oil exponents, respectively. S_{wr} and S_{or} denotes the irreduciblae water saturation and residual oil saturation. The Corey exponent is normally 4 for the wetting phase and 2 for the non-wetting phase.

In chapter 5.2 and chapter 6, a Corey type formula (Corey, 1954) was used for the relative permeability of gas expressed as:

$$k_{rg}(S) = \left(1 - \widetilde{S}\right)^2 \left(1 - \widetilde{S}^2\right), \tag{C.4}$$

where

$$\widetilde{S} = \frac{S - S_{wr}}{1 - S_{gr} - S_{wr}}. \tag{C.5}$$

Here k_{rg} is the relative gas permeability, S is the water saturation, S_{wr} the irreducible water saturation and S_{gr} the irreducible gas saturation.

For the relative permeability of water, a Van Genuchten function (Van Genuchten, 1980) was used:

$$k_{rw}(S) = \sqrt{S^*}\left[1 - \left(\left(1 - S^{*1/\lambda}\right)^{\lambda}\right)\right]^2 \quad \text{(C.6)}$$

where

$$S^* = \frac{S - S_{wr}}{1 - S_{wr}} \quad \text{(C.7)}$$

Here k_{rw} is the relative water permeability and λ is an empirical parameter. The value of λ is taken from Silin et al. (2006).

Appendix D: Matlab codes

Solution for original Buckley-Leverett

```
% Input values
KRO=0.8;         KRW=0.4;     Swr=0.2;     Sor=0.2;
no=2;            nw=4;        muo= 1e-3;    muw=5e-4;
S=Swr:0.001:1-Sor;
t=[0.05; 0.1; 0.15; 0.2; 0.25; 0.3; 0.35; 0.4];


%Relative permeabilities
Swn = (S - Swr ) ./ (1 - Swr - Sor);
coreyrel_o =KRO.*((1-Swn).^no);
coreyrel_w = KRW .*(Swn.^nw) ;
kro=@(S)coreyrel_o;
krw=@(S)coreyrel_w;

%Fractional flow
BLffw=(1)./((coreyrel_o./coreyrel_w).*(muw/muo)+1);
fw=@(S) BLffw;

%Derivative of fractional flow
dfw=gradient(BLffw,S);
ddfw=@(S)dfw;

% Saturatuion Profile
x= @(S)t*(ddfw(S));

figure (1) % Figure 1.2
plot(S,kro(S),'linewidth',2);
hold on
plot(S,krw(S),'linewidth',2);
ylabel('RelPerm','Fontsize',20);
xlabel('S','Fontsize',20);
legend('k_r_o','k_r_w');

figure (2) % Figure 5.2
plot(S,fw(S),'linewidth',2);
axis([0 1 0 1]);
ylabel('f_w','Fontsize',20);
hold on
yyaxis right
plot(S,ddfw(S),'linewidth',2);
axis([0 1 0 5]);
xlabel('S', 'Fontsize',20);
ylabel('df_w/d_S','Fontsize',20);

figure (3) % Figure 5.7
plot(x(S),S,'linewidth',2);
xlabel('x_D', 'Fontsize',20);
ylabel('S','Fontsize',20);
legend('0.05','0.1','0.15','0.2','0.25','0.3','0.35','0.4');
```

Solution for horizontal interface

```
% Fat plume calculation
% formulas from Silin et al., (2006, 2009)
% calculates the three key saturations (s', s^M, and S^*)
% calculates the two key velocities (v1' and v2^*)

swr = 0.1;     % irreducible water saturation
sgr = 0.05;    % irreproducible gas saturation
mug = 5e-5;    % gas viscosity (Pa*s)
muw = 5e-4;    % water viscosity (Pa*s)
phi_1 = 0.26;   % porosity below interface
phi_2 = 0.08;   % porosity above interface

k_conv = 9.869233e-16;  % permeability conversion factor from mD to SI

k_1 = 571*k_conv;    % permeability below interface (m^2)
k_2 = 0.5*k_conv;     % permeability above interface (m^2)

rho_w = 1000;   % water density (kg/m^3)
rho_g = 561;    % gas density (kg/m^3)
g = 9.81;       % acceleration of gravity (m/s^2)

sec_to_day = 60*60*24;    %conversion from seconds to days

dim_factor=(rho_w-rho_g)*g/muw; % dimensional scaling factor

ds=.001;         % step size along S-axis
s=[0:ds:1];     % S-axis

% relative water permeability (van Genuchten)
lambda = 0.457;     % parameter
sstar=(s-swr)/(1-swr);
krw=sqrt(sstar).*(1.-(1.-sstar.^(1/lambda)).^lambda).^2;

% relative gas permeability (Corey-type)
stilde=(s-swr)/(1-sgr-swr);
krg=((1.-stilde).^2).*(1.-stilde.^2);

krw=max(0,real(krw));   % remove complex and negative values
krg=max(0,krg);         % remove negative values

fs=(krw.*krg)./((mug/muw)*krw+krg); % fractional flow function

% locate sstar by maximizing fs/(1-s)
[m_sstar,i_sstar] = max(fs./(1-s)); % i_sstar is the index of max value
sstar=ds*i_sstar;   % value of sstar

% locate smax by maximizing fs
[m_sm,i_smax] = max(fs);    %  i_smax is the index of max value
smax=ds*i_smax; % value of smax

% locate sprime by solving associated zero crossing problem
qq=(phi_1/phi_2)*(k_2/k_1);         % dim. less scaling parameter
[d,i_sprime] = min(abs(fs-qq*fs(i_sstar))); % i_sprime is index
sprime=ds*i_sprime; % value of sprime
```

```
% calculation of the two key velocities

% velocity of reflected plume front in lower layer
v1_prime = - (1/phi_1)*(fs(i_sprime)-fs(i_sstar))/(sprime-sstar); %dimless
v1_prime_dim = v1_prime*k_1*dim_factor;    % dimensional (m/s)
v1_prime_days = sec_to_day*v1_prime_dim;   % dimensional (m/days)

% velocity of plume front transmitted into upper layer
v2_star = (1/phi_2)*fs(i_sstar)/(1.-ds*i_sstar);    %dimensionless
v2_star_dim = v2_star*k_2*dim_factor;               % dimensional (m/s)
v2_star_days = sec_to_day*v2_star_dim;              % dimensional (m/days)

figure(1) % Figure 6.3a, 7.2a, 7.3b
clf
t_ax=[0:1:x];           % plot positions x days ahead
x1=v1_prime_days*t_ax;  % position (m) of reflected plume front
x2=v2_star_days*t_ax;   % position (m) of transmitted plume front
plot(t_ax, x1,'linewidth',2)
hold on
plot(t_ax, x2,'r','linewidth',2)
title('Front propagation','fontsize',20)
xlabel('Time (days)','Fontsize',20)
ylabel('Distance(m)','Fontsize',20)
xlim([0 x])
grid on
legend('v_1 (reflected)','v_2^* (transmitted)')
hold off

figure(2) % Figure 6.3b-d, 7.2b, 7.3b
clf
xlim([0 1])
ylim([-100 100])
line([sprime sprime], [-100 100],'linewidth',2,'linestyle','--')
hold on
line([smax smax], [-100 100],'linewidth',2,'linestyle','--')
line([sstar sstar], [-100 100],'linewidth',2,'linestyle','--')
line([0 1], [0 0],'linewidth',3)
grid on
title('Saturations','fontsize',20)
xlabel('S_w','Fontsize',20)
ylabel('Distance(m)','Fontsize',20)
hold off
```